Measuring of Radiation Exposure of the Landscape

Bc. Aleš Navrátil

Master's thesis
2024

Tomas Bata University in Zlín
Faculty of Applied Informatics

Univerzita Tomáše Bati ve Zlíně
Fakulta aplikované informatiky
Ústav elektroniky a měření

Akademický rok: 2023/2024

ZADÁNÍ DIPLOMOVÉ PRÁCE

(projektu, uměleckého díla, uměleckého výkonu)

Jméno a příjmení:	**Bc. Aleš Navrátil**
Osobní číslo:	**A22407**
Studijní program:	**N1032A020003 Bezpečnostní technologie, systémy a management**
Specializace:	**Bezpečnostní technologie**
Forma studia:	**Kombinovaná**
Téma práce:	**Měření radiačního zatížení krajiny**
Téma práce anglicky:	**Measurement of Radiation Exposure of the Landscape**

Zásady pro vypracování

1. Seznamte se s problematikou měření radioaktivity přírodního prostředí pomocí laboratorního vybavení na FAI UTB ve Zlíně.
2. Realizujte měření plošného rozložení radiačního pozadí ve vybrané lokalitě a pokuste se o interpretaci získaných dat s důrazem na zjištění případného vlivu lidské činnosti na radioaktivním znečistění zkoumané krajiny.
3. Ve vybraném prostoru proveďte sondu do hloubky alespoň 0,75 metru s postupným odebíráním půdních vrstev.
4. Odebrané vzorky proměřte v laboratoři a interpretujte získaná data.
5. Výsledky vyhodnoťte a navrhněte případný další postup zkoumání zadaného tématu.

Forma zpracování diplomové práce: **tištěná/elektronická**
Jazyk zpracování: **Angličtina**

Seznam doporučené literatury:

1. Procházka V. at al.: Stabilní a radioaktivní cesium v přírodním prostředí, Chemické listy vol. 117 (2023), 501-507.
2. Matsuda N. at al.: Depth profiles of radioactive cesium in soil using a scraper plate over a wide area surrounding the Fukushima Dai-ichi Nuclear Power Plant, Japan, Journal of Environmental Radioactivity vol. 139 (2015), 427-434.
3. Mishra S. at al.: Reprint of "Vertical migration of radio-caesium derived from the Fukushima Dai-ichi Nuclear Power Plant accident in undisturbed soils of grassland and forest", Journal of Geochemical Exploration, vol.184 (2018), 271--295.
4. Matsuoka K. at al.: Continuous nitrogen fertilization retards the vertical migration of Fukushima nuclear accident--derived cesium-137 in apple orchard soil, Science of the Total Environment vol.731 (2020), 138903.
5. Rulík P., Helebrant J.: Mapa kontaminace půdy České republiky ^{137}Cs po havárii JE Černobyl, Zpráva Státního ústavu radiační ochrany v.v.i. č.22/2011.

Vedoucí diplomové práce: **doc. RNDr. Vojtěch Křesálek, CSc.**
Ústav elektroniky a měření

Datum zadání diplomové práce: **20. listopadu 2023**
Termín odevzdání diplomové práce: **28. května 2024**

doc. Ing. Jiří Vojtěšek, Ph.D. v.r.
děkan

UNIVERZITA TOMÁŠE BATI VE ZLÍNĚ
Fakulta aplikované informatiky

Ing. Milan Navrátil, Ph.D. v.r.
ředitel ústavu

Ve Zlíně dne 1. prosince 2023

I hereby declare that:

- I understand that by submitting my Master‘s thesis, I agree to the publication of my work according to Law No. 111/1998, Coll., On Universities and on changes and amendments to other acts (e.g. the Universities Act), as amended by subsequent legislation, without regard to the results of the defence of the thesis.
- I understand that my Master ‘s thesis will be stored electronically in the university information system and be made available for on-site inspection, and that a copy of the Diploma/Thesis will be stored in the Reference Library of the Faculty of Applied Informatics, Tomas Bata University in Zlín, and that a copy shall be deposited with my Supervisor.
- I am aware of the fact that my Master‘s thesis is fully covered by Act No. 121/2000 Coll. On Copyright, and Rights Related to Copyright, as amended by some other laws (e.g. the Copyright Act), as amended by subsequent legislation; and especially, by §35, Para. 3.
- I understand that, according to §60, Para. 1 of the Copyright Act, TBU in Zlín has the right to conclude licensing agreements relating to the use of scholastic work within the full extent of §12, Para. 4, of the Copyright Act.
- I understand that, according to §60, Para. 2, and Para. 3, of the Copyright Act, I may use my work - Master‘s thesis, or grant a license for its use, only if permitted by the licensing agreement concluded between myself and Tomas Bata University in Zlín with a view to the fact that Tomas Bata University in Zlín must be compensated for any reasonable contribution to covering such expenses/costs as invested by them in the creation of the thesis (up until the full actual amount) shall also be a subject of this licensing agreement.
- I understand that, should the elaboration of the Master‘s thesis include the use of software provided by Tomas Bata University in Zlín or other such entities strictly for study and research purposes (i.e. only for non-commercial use), the results of my Master ‘s Thesis cannot be used for commercial purposes.
- I understand that, if the output of my Master‘s thesis is any software product(s), this/these shall equally be considered as part of the thesis, as well as any source codes, or files from which the project is composed. Not submitting any part of this/these component(s) may be a reason for the non-defence of my thesis.

I herewith declare that:

- I have worked on my thesis alone and duly cited any literature I have used. In the case of the publication of the results of my thesis, I shall be listed as co-author.
- That the submitted version of the thesis and its electronic version uploaded to IS/STAG are both identical.

In Zlín; dated:

Aleš Navrátil, v. r.
Student´s Signature

ABSTRAKT

Diplomová práce se zabývá problematikou měření radioaktivity přírodního prostředí s využitím laboratorního vybavení FAI UTB ve Zlíně. Důležitou roli zde hraje měření plošného rozložení radiačního pozadí ve vybrané lokalitě a následná interpretaci získaných dat. Pomocí geologické mikrosondy byly měřeny jednotlivé odebrané vrstvy až do hloubky 1,3 m. Pří výkopu byly nacházeny zlomky předmětů, které se staly součástí studia v dané problematice. Na základě získaných dat při terénním a laboratorním měření byl potvrzen výskyt primordiálních a antropogenních radionuklidů. Zjištěné údaje poukazují na souvislost vlivu lidské činnosti a radioaktivním znečišťování zkoumané lokality.

Klíčová slova: radioaktivita, geologická mikrosonda, primordiální radionuklidy, antropogenní radionuklidy.

ABSTRACT

This Master's thesis deals with the measurement of radioactivity in the natural environment using the laboratory equipment of FAI UTB in Zlín. An important role is played by the measurement of the area composition of the radiation background in the selected locality and the subsequent interpretation of the obtained data. Using a geological microprobe, individual sampled layers were measured up to a depth of 1.3 m. Fragments of objects that became part of the study in the given problem-matrix were found during the excavation. Based on the data obtained during field and laboratory measurements, the presence of primordial and anthropogenic radionuclides was confirmed. The findings indicate a link between the influence of human activities and radioactive pollution of the studied site.

Keywords: radioactivity, geological microprobe, primordial radionuclides, anthropogenic radionuclides.

ACKNOWLEDGEMENTS

I would like to express my gratitude to my thesis supervisor doc. RNDr. Vojtěch Křesálek, CSc., who led this work in an exemplary manner. I would also like to thank the Institute of Nuclear Physics of the AV ČR and the Institute of Archaeology of the AV ČR, the Historical Institute of the Homeland Museum in Olomouc, the field archaeologists from the Komenský Museum in Přerov and the geologists from the Museum of South-East Moravia in Zlín for providing data without which this study would have been more difficult to produce. Last but not least, I would like to thank my entire family, who have been my greatest support during the study.

I hereby declare that the print version of my Master 's thesis and the electronic version of my thesis deposited in the IS/STAG system are identical.

CONTENTS

INTRODUCTION

Ionizing radiation is an integral part of the origin and evolution of life on our planet. This radiation is a fundamental building block of our existence. It is a part of us at birth and at death. It is with us in our daily activities, whether we sleep, eat or work. It is important to be aware of its presence and to make reasonable efforts to understand the diversity of its effects on our lives and health. People, their efforts have in some cases crossed an imaginary line in the use of scientific knowledge. In pursuing modern technologies, they do not consider in depth the consequences of his actions. This results in polluting the environment with radionuclides that affect the natural ecosystem.

One of the tasks of the Master's thesis is to measure the area distribution of the radiation background in the selected locality and to determine the possible influence of human activities on the radioactive pollution of the studied landscape. Another part of the thesis is to carry out a geological microprobe to a depth of at least 0.75 m with the gradual removal of soil layers. The final part of the work is the evaluation of the measured data and the proposal of possible further procedures for the investigation of the assigned topic.

The contribution of the Master's thesis should be the determination of the distribution of radioactive cesium ^{137}Cs fallout from nuclear experiments in the 1960s and from the Chernobyl accident in the selected area.

I. THEORY

1 ORIGIN OF IONIZING RADIATION

The origin of ionizing radiation can be traced back to the beginning of the universe and our solar system. Humanity has been dealing with the question of the origin of the universe and the very origin of life on our planet since time immemorial.

1.1 Cosmic Inflation

According to some theories, the origin of the universe is related to the so-called inflationary model, which occurred approximately 13.8 billion years ago [1]. The theory talks about the expansion of the universe after the big bang at an exponential rate in a fraction of a second. This rapid expansion produced certain types of particles called scalars [2]. These particles are thought to have short wavelengths that have spectra corresponding to thermal radiation. The only scalar particle that is assumed to exist is the Higgs boson, also known as the God particle [3; 4; 5].

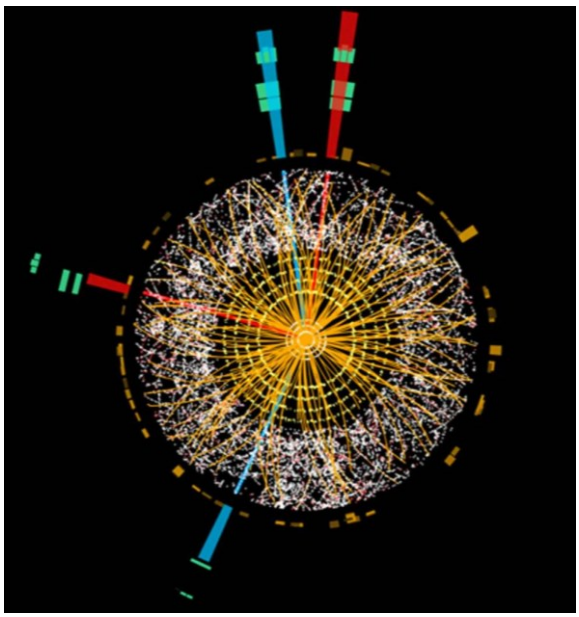

Figure 1. Recorded collision of Higgs boson and its decay into 4 leptons at CERN [6].

In a very short period after the Big Bang, the density approached a critical value, which is still critical today. If the theory of inflation is correct, then the universe could also contain dark matter whose density is close to or exceeds this critical value [4]. The existence of dark matter has not yet been proven and is in the mathematical modelling stage. These models also suggest that dark matter may have existed before the Big Bang [2].

The assumption is that the initial temperature of the universe was extreme. This extreme environment consisted of elementary particles such as quarks, gluons, and electrons. As the

universe expanded, it cooled. During this process, quarks and gluons condensed into hadrons. As the hadrons joined together, atomic nuclei were formed. When an electron was added to the atomic nuclei, atoms were formed as the basic building material of matter [7; 8].

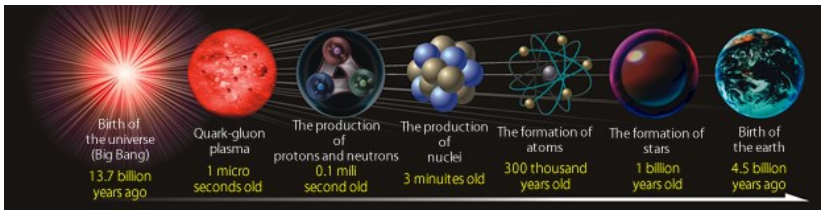

Figure 2. The origin of the universe [7].

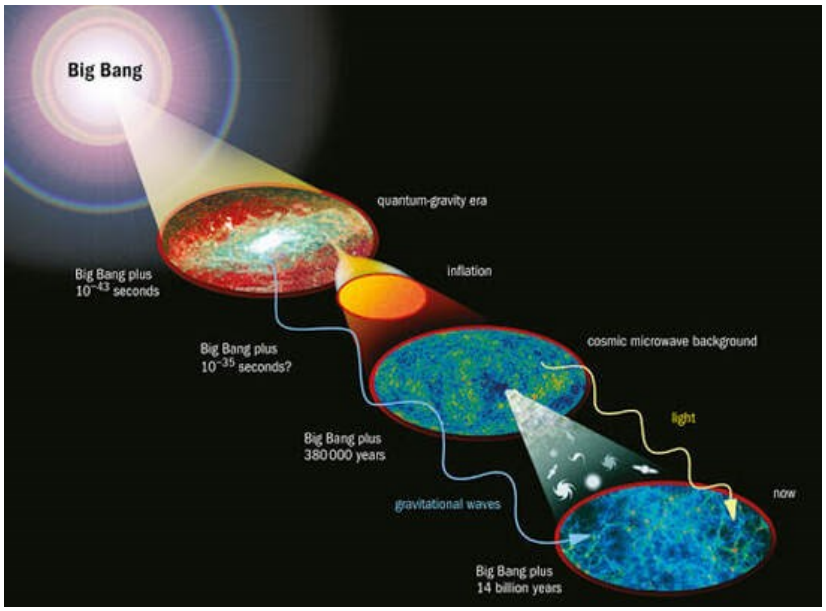

Figure 3. The theory of cosmic background radiation in connection with the theory of the origin of the universe [9].

1.2 Natural Sources of Ionizing Radiation

Natural ionizing radiation is a natural part of the environment that surrounds us on our planet. This radiation is ubiquitous. The intensity of radiation can be influenced by magnetic latitude, solar activity or altitude. In addition, the intensity of radiation is influenced by the composition of rocks in the Earth's crust, the movement of the Earth's plates or volcanic activity [10; 11].

1.2.1 Cosmic Rays

Cosmic rays originate from several sources that are isotropic to the Earth. Determining the source of this radiation is very difficult [11]. This is due to the inhomogeneity of the magnetic fields in space, which affect the motion of particles. In this interaction, all information about the source of the radiation may be lost [12].

1.2.1.1 Primary Cosmic Rays

This is a high-energy radiation of cosmic origin, which consists of a stream of particles whose energy is around 10 GeV in some cases up to 10^{20}eV. This radiation strikes the outer layer of the atmosphere where hadronic reactions are first triggered, followed by electromagnetic cascades [11; 12].

The putative sources of primary cosmic rays include [11; 12]:

- Galactic cosmic rays
  - Pulsars
  - Magnetars
  - Galactic nuclei
  - Galaxy collisions
  - Black holes
  - Supernova explosion

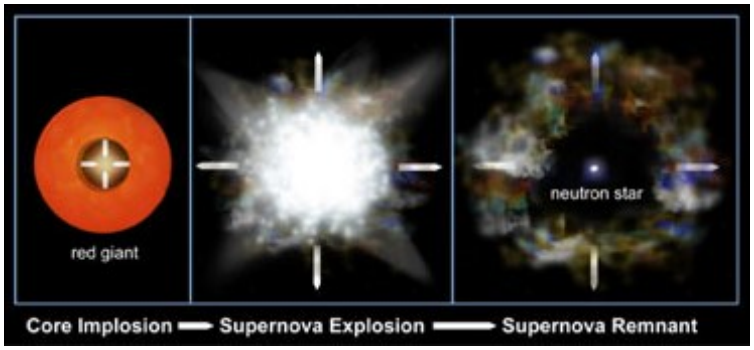

Figure 4. Core-collapse supernova [13].

- Solar cosmic radiation
  - Low energy solar winds
  - High-energy particles from solar flares

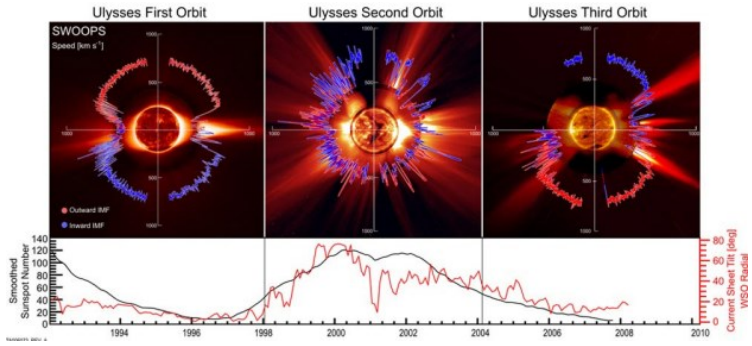

Figure 5. Polar plots of the solar wind speed [14].

- Van Allen radiation belts - inner proton, outer electron. These are bands of energetically charged particles that are an integral part of the Earth's magnetosphere [12].

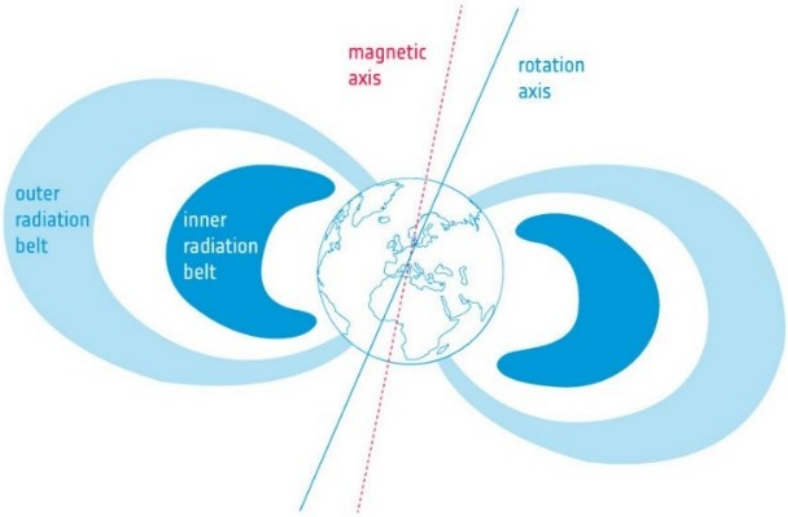

Figure 6. Van Allen radiation belts [15].

1.2.1.2 Secondary Cosmic Rays

High-energy particles collide with air particles mainly with nitrogen and oxygen nuclei as they pass through the atmosphere [17]. This is the so-called cosmic ray cascade. These collisions produce new particles that give rise to secondary cosmic rays. Many nuclear reactions take place, producing a large variety of radionuclides. These iterations occur in the atmosphere mostly at altitudes around 10-30 km [11]. The first interaction when particles collide with the upper atmosphere is the spallation reaction, which produces reaction between the higher energy nucleoids and the target nuclei [17; 18].

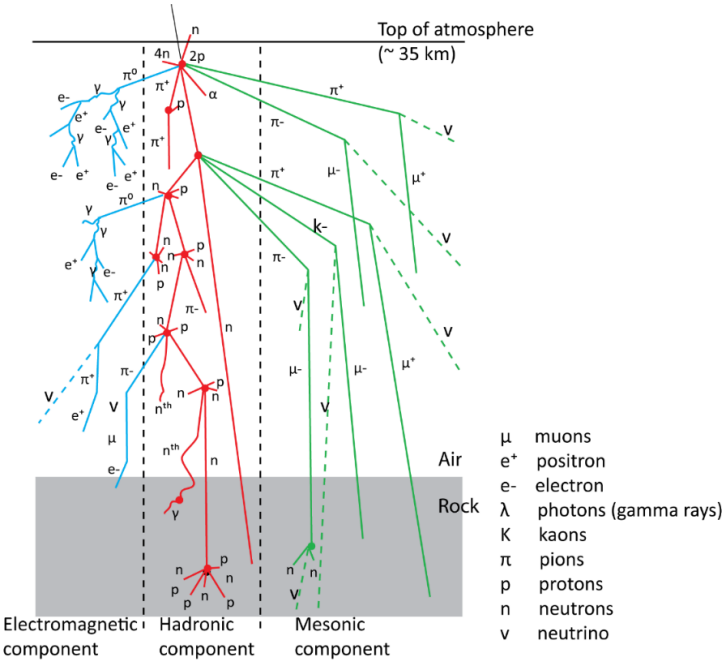

Figure 7. Cosmic radiation cascade [18].

A shower of secondary radiation reaches the Earth's surface. A large part of this radiation is made up of protons (p), helium nuclei (alpha radiation) and heavy metals (about 1%). A small part is made up of electrons (e^-), positrons (e^+), neutrinos (v), neutrons (n) or energetic gamma photons (λ). Then there are positive and negative pions (π), positive and negative kaons (K). Pions and kaons can decay into muons (μ) and neutrinos. Pions can also decay into gamma-ray photons. Another reaction can be the decay of gamma rays and muons into electrons and positrons [18].

1.2.1.3 Carbon ^{14}C

Neutron particles colliding with nitrogen ^{14}N nuclei decay into carbon ^{14}C and protons [11]. The resulting beta radioactive particle has a half-life of 5730 years. In the process, carbon ^{14}C decays back into nitrogen ^{14}N. This time it takes for carbon ^{14}C to decay is called the half-life. Knowing the decay rate allows dating of, for example, the age of archaeological finds [19].

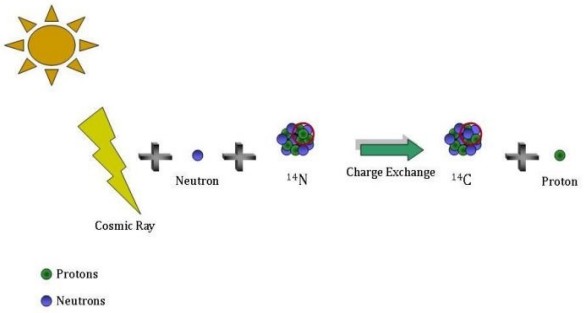

Figure 8. The process of carbon ^{14}C formation [19].

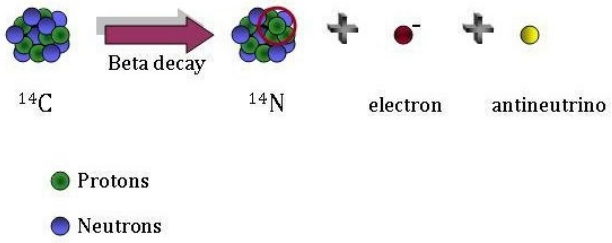

Figure 9. Decay of beta radioactive particle ^{14}C [19].

If we would like to be more specific in the process of carbon ^{14}C dating, we can describe this decay as follows:

After 5730 years, half the amount of ^{14}C carbon is present in the sample. After twice that amount of time, only one quarter of the ^{14}C carbon remains in the sample. After ten times the half-life, the amount of carbon ^{14}C is <0.1% [19].

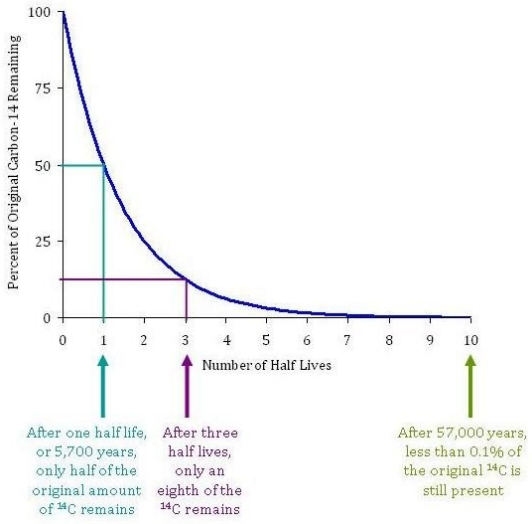

Figure 10. Half-life of carbon ^{14}C [19].

1.2.2 Natural Radionuclides

Natural radionuclides are all around us. These radionuclides migrate through the environment in different ways. During these migrations, radionuclides enter rocks, soil, water sources and air. In addition, internal exposure occurs in living organisms that receive these radionuclides into their bodies through food and fluid intake [20].

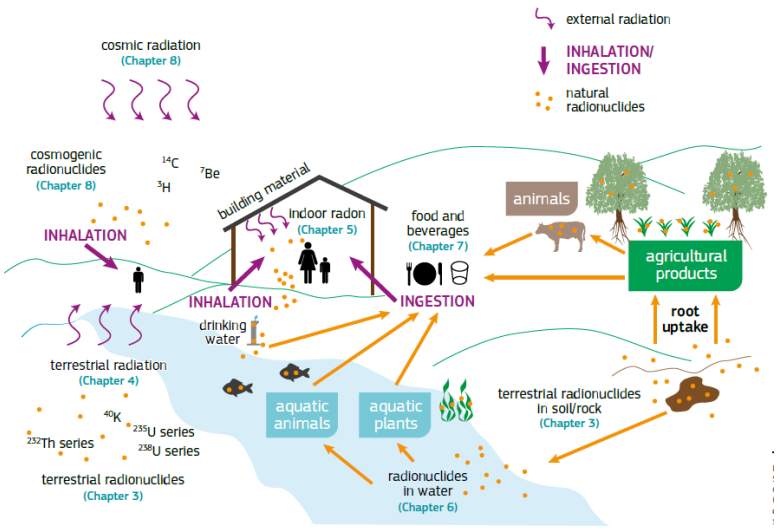

Figure 11. Natural radionuclides [20].

Natural radionuclides are divided into three groups:

1.2.2.1 Primordial Radionuclides

Primordial radionuclides originated long before the Earth was formed. These radionuclides have long half-lives. We can look for their origin in the heart of exploding stars (supernovae). These explosions gave rise to the germ cloud and from it our solar system about 5 billion years ago [21]. Primary radionuclides are also one of the sources of geothermal energy. This means that the Earth's temperature is influenced by radioactive processes in its interior. The amount of thermal geothermal energy that is generated is estimated to be 46 TW. Of this, radionuclides contribute about 15-25 TW. This geothermal flux is released continuously. Exceptions are tectonic plate shifts, earthquakes or volcanic activity. The rest of the heat flux comes from friction and gravitational attraction [22; 23].

The decay of primordial radionuclides in the Earth's core is a continuous process that continuously heats the geological material. These include rocks, gases and underground water sources. Heat values vary with depth. This is a gradual change in temperature called a

geothermal gradient. The estimated average value of the geothermal gradient on Earth is about 25 ^{o}C per 1 km depth [23].

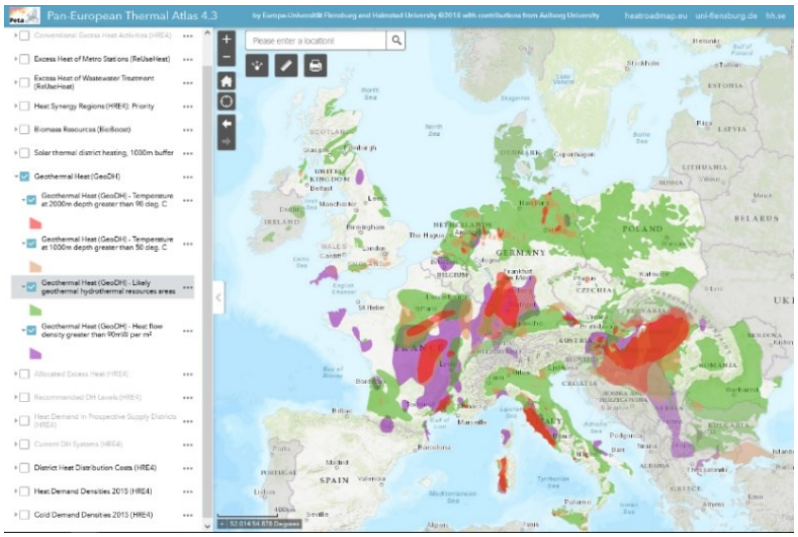

Figure 12. Pan-European thermal atlas [24].

The primordial radionuclides with the longest half-lives include:

Potassium ^{40}K

It is a lithophile element, which is one of the most abundant elements in nature. The half-life is $1{,}25 \times 10^{9}$. Potassium occurs naturally in the form of three isotopes $^{39}K(\sim 93\%)$, $^{40}K(\sim 0{,}012\%)$, $^{41}K(\sim 6{,}9\%)$. Only the isotope ^{40}K undergoes radioactive transformation. The potassium content of ^{40}K in the Earth's crust is around 2.5% [11]. Potassium is also very important for living organisms on our planet. The average potassium content in a 70 kg human body is estimated to be 4400 Bq [20; 21].

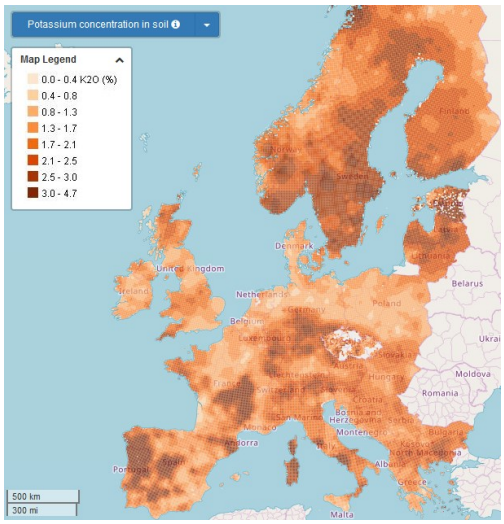

Figure 13. The amount of potassium in the soil layers of Europe [25].

Uranium ^{235}U, ^{238}U

It is an element of the actinide series with atomic number 90 and a long half-life. The isotope $^{238}U(\sim 99{,}274\%)$ with a half-life of $4{,}47 \times 10^9$ is most often found in nature. Another isotope is $^{235}U(\sim 0{,}72\%)$ with a half-life of $7{,}04 \times 10^9$ [26].

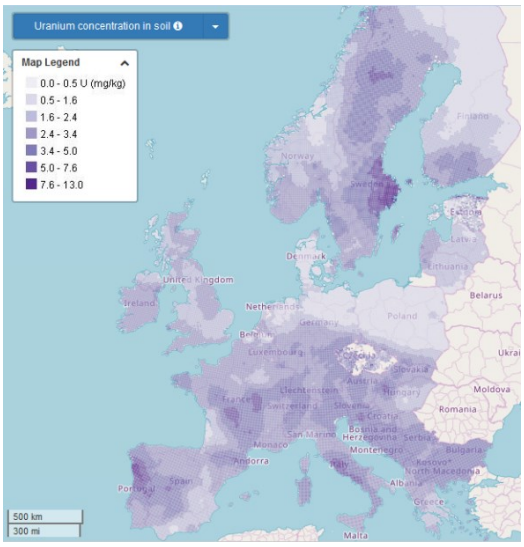

Figure 14. The amount of uranium in the soil layers of Europe [25].

Thorium ^{232}Th

It is a long-lived element of the actinide series with atomic number 90. The half-life of ^{232}Th is $1{,}41 \times 10^{10}$. The occurrence of thorium in the Earth's crust averages about 10.7 ppm. In normal rock, it is 1.6 - 20 ppm [26].

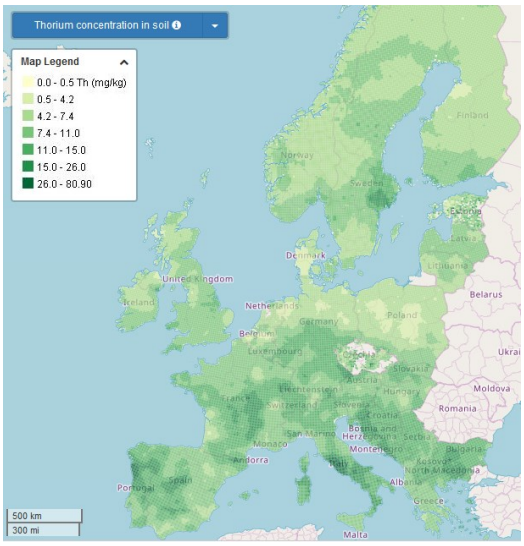

Figure 15. The amount of thorium in the soil layers of Europe [25].

1.2.2.2 Secondary Radionuclides

Secondary radionuclides are produced by the decay of primordial radionuclides. These decays produce radioactive decay series. These decays produce alpha and beta radioactivity. The nuclei in these decays generate gamma rays [26].

In these decay series, α and β^- transformations occur. In some cases, branching occurs, in which the radionuclide may decay into multiple elements. Each series is always terminated by a single stable nuclide [27].

Radioactive decay series:

- uranium - radium (decay series of uranium ^{238}U), beginning uranium ^{238}U and end lead ^{206}Pb, A=4n+2
- uranium - actinium (uranium ^{235}U decay series), beginning uranium ^{235}U and ending lead ^{207}Pb, A=4n+3
- thorium (thorium ^{232}Th decay series), beginning thorium ^{232}Th and ending lead ^{208}Pb, A=4n
- neptunium (decay series of neptunium ^{237}Np, beginning neptunium ^{237}Np and ending thallium ^{205}TI, A=4n+1 [27].

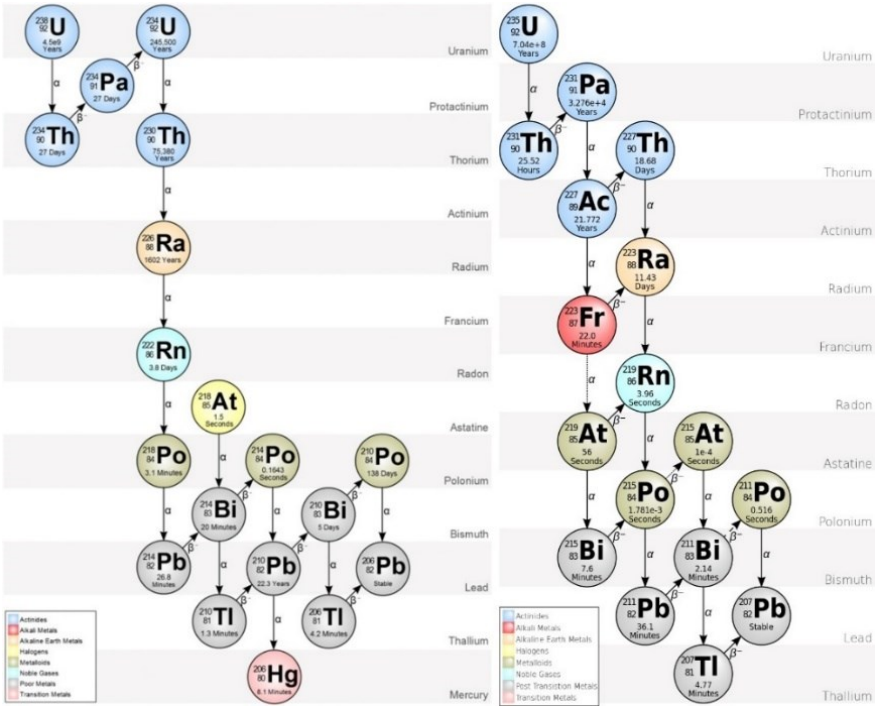

Figure 16. Radioactive decay series of uranium ^{238}U, ^{235}U [28; 29].

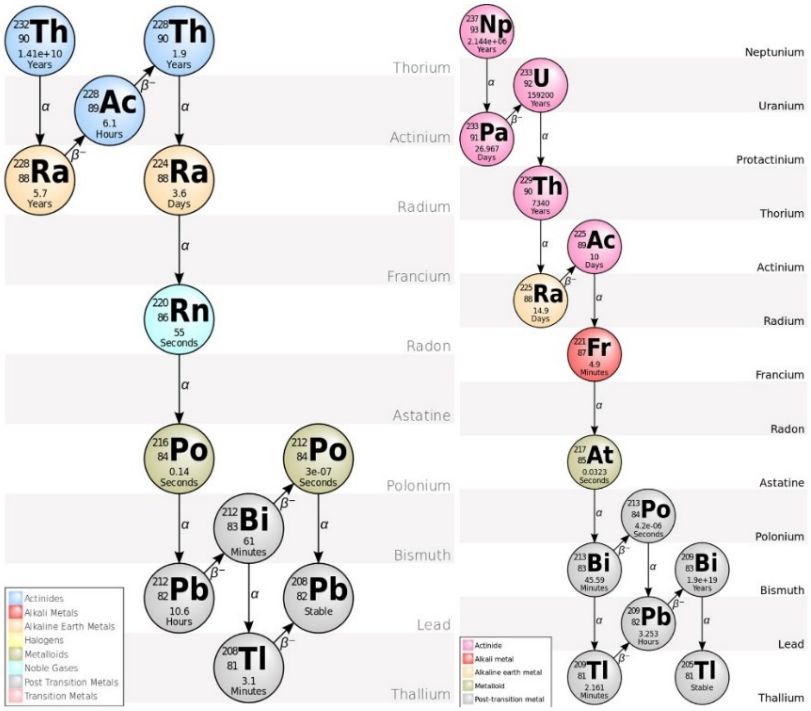

Figure 17. Radioactive decay series of thorium ^{232}Th and neptunium ^{237}Np [29].

1.3 Artificial Sources of Ionizing Radiation

Artificial sources of ionizing radiation are so-called anthropogenic radionuclides, which arise because of human activity [30]. Mankind has managed to create many anthropogenic radionuclides related to the military industry, energy production or health care. In many cases these are negligible, but there are cases where the anthropogenic source of radiation exceeds the natural sources of radiation. However, it should be emphasized that radiation doses of anthropogenic radionuclides used in medicine or industry are always easier to control than, for example, natural radiation, nuclear weapons tests or nuclear power plant accidents [31].

Figure 18. Artificial sources of ionizing radiation. Nuclear tests [32]. Nuclear power plants [33]. CT scanner [34]. Airport X-rays [35]. Particle accelerators [36].

The largest sources of these anthropogenic radionuclides include [30]:

- Nuclear weapons tests
- Nuclear power plants – operation (nuclear fuel cycle), accidents
- Medicine
- Industry
- Science and research

Here is a list of anthropogenic radionuclides created and used in the military, commercial, space, and medical industries [37]:

1.3.1 Americium ^{241}Am

It is a man-made radioactive metallic element. This element is produced during nuclear fission in nuclear reactors or nuclear weapons tests. The half-life is 432.2 years [38]. Americium ^{241}Am is produced by the radioactive decay of uranium $^{238}_{92}U$. Subsequently, β decay produces the isotope plutonium ^{239}Pu [39].

$$^{238}_{92}U \xrightarrow{n,\gamma} {}^{239}_{92}U \xrightarrow{\beta^-} {}^{239}_{93}Np \xrightarrow{\beta^-} {}^{239}_{94}Pu \xrightarrow{2(n,\gamma)} {}^{241}_{94}Pu \xrightarrow{\beta^-} {}^{241}_{95}Am \qquad (1.1)$$

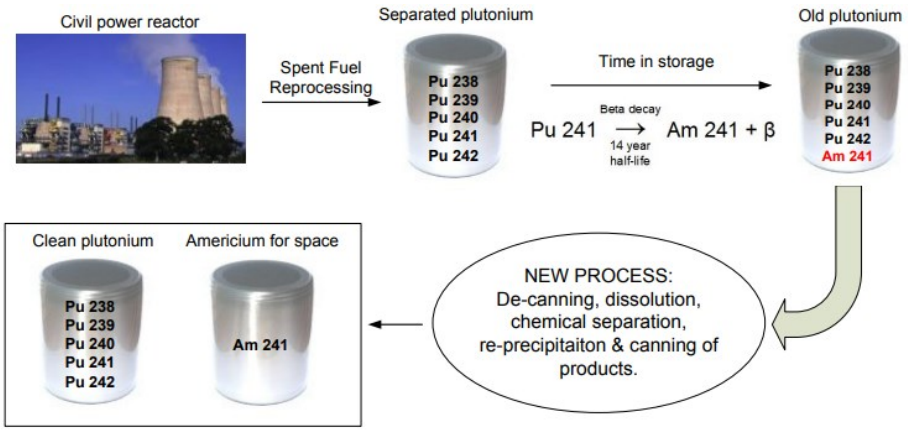

Figure 19. Radioactive decay of plutonium ^{241}Pu and formation of americium ^{241}Am [40].

Americium ^{241}Am is currently used in smoke detectors for its wide range of fire detection [38]. A standard smoke detector contains 0.9 μCi or 33 Bq of Americium ^{241}Am [41].

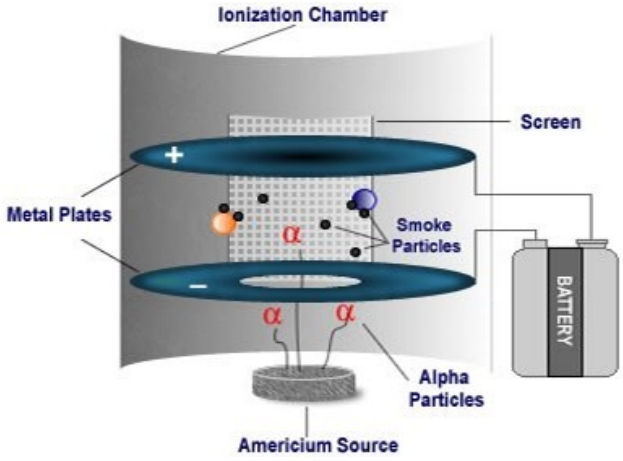

Figure 20. Schematic of a fire detector using americium ^{241}Am [42].

There is now a presumption of the use of americium ^{241}Am in space projects. These include use as an energy source to power spacecraft, satellites and space probes [43].

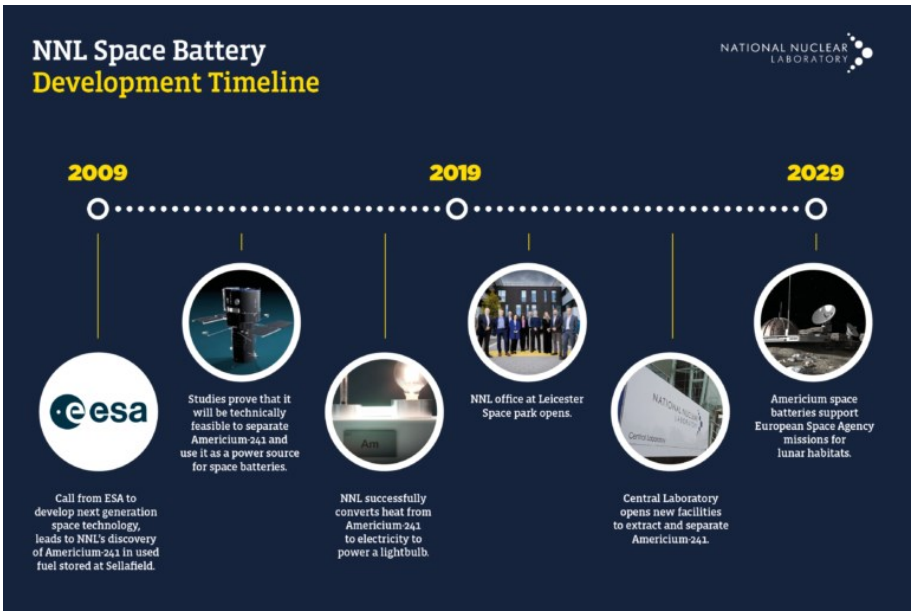

Figure 21. Timeline of the use of americium ^{241}Am in ESA space projects [44].

Americium ^{241}Am increases the risk of cancer if ingested or inhaled. In this contamination, it concentrates in tissues and bones [38].

1.3.2 Cesium ^{137}Cs

It is a fission product with a half-life of 30.17 years (β-decay). This element is produced during nuclear fission in nuclear reactors or nuclear weapons tests. The radionuclide is easily detected by a gamma spectrometer [45].

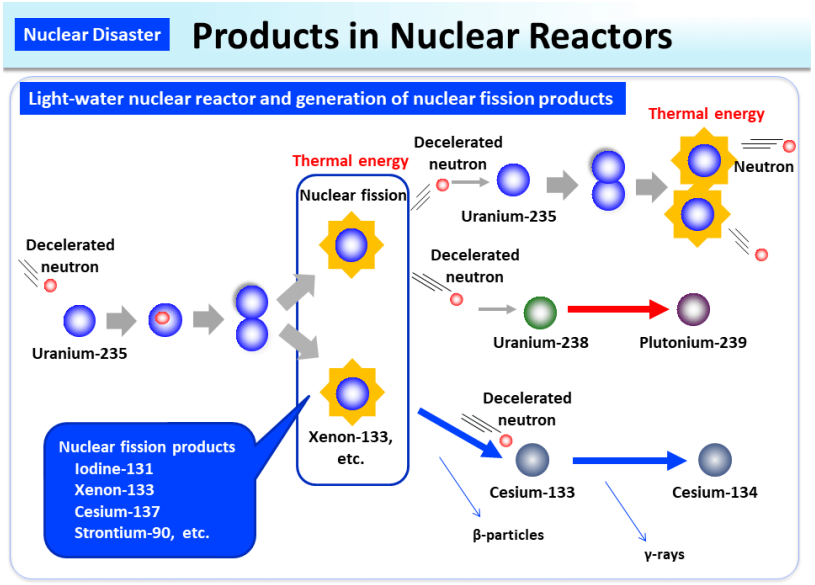

Figure 22. The nuclear fission reaction of uranium ^{137}Cs. This process produces cesium ^{137}Cs [47].

Cesium ^{137}Cs is produced in the nuclear fission reaction of uranium ^{235}U in β decay. Cesium ^{137}Cs produces barium ^{137}Ba from the decay series, which is metastable. After the release of γ radiation, barium ^{137}Ba becomes stable [46].

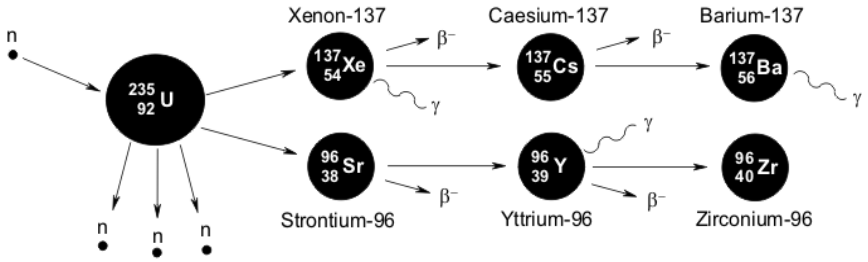

Figure 23. The decay series of the nuclear fission reaction of uranium ^{235}U to the stable radionuclide ^{137}Ba [47].

$$^{137}_{55}Cs \xrightarrow{\beta} {}^{137}_{56}Ba \xrightarrow{\gamma} {}^{137}_{56}Ba \qquad (1.2)$$

Cesium ^{137}Cs is used in medicine for cancer treatment. In industry, cesium is used in measuring fluid flow rates in piping systems or for measuring material thicknesses [48].

Cesium ^{137}Cs is readily airborne and can bind to building materials. When contaminated with soil, it can migrate in plants and vegetation [48].

Figure 24. Use of cesium ^{137}Cs in radiotherapy in nuclear medicine [50].

Cesium ^{137}Cs contamination results in burns and, at high doses, radiation sickness. Exposure to cesium ^{137}Cs leads to an increased risk of cancer [48].

1.3.3 Cobalt ^{60}Co

It is an element that has properties like iron. It has a grey blue color with a half-life of 5.27 years [51]. Natural cobalt is found in minerals with uses such as in the glass industry. Cobalt ^{60}Co is produced by neutron activation of cobalt ^{59}Co when steel structures are exposed to neutron radiation in nuclear reactors [52]. It involves β decay to form ^{60}Ni simultaneously with the emission of γ radiation [53].

$$^{59}_{27}Co + ^{1}_{0}n \rightarrow ^{60}_{27}Co \rightarrow ^{60}_{28}Ni + ^{0}_{-1}\beta + 2^{0}_{0}\gamma \qquad (1.\ 3)$$

Cobalt ^{60}Co is used in industry for example in levelling equipment or in instruments for measuring the thickness of materials. It also plays an important role in radiation therapy [51].

Cobalt ^{60}Co contamination leads to absorption in soft tissues where it can cause cancer [51].

1.3.4 Iodine ^{129}I, ^{131}I

It is a purplish red crystalline element. The property of this radionuclide is its ability to directly change from solid to gaseous state [54]. Iodine ^{129}I has a half-life of $1{,}57 \times 10^{7}$ and iodine ^{131}I has a half-life of 8.02 days. Both iodine emits β particles during radioactive

decay. Iodine ^{129}I comes only from nuclear experiments. Iodine ^{131}I comes from both nuclear experiments and nuclear reactors [55].

Iodine ^{131}I is produced during nuclear fission, when enriched uranium ^{235}U, ^{238}U is bombarded with neutrons. During this process, in addition to iodine ^{131}I, xenon ^{133}Xe, cesium ^{137}Cs, or strontium ^{90}Sr are produced [49].

The use of iodine ^{131}I is, for example, in medicine in the diagnosis and treatment of thyroid cancer. When contaminated with iodine, skin and eye burns occur. Internal exposure affects thyroid function [55].

1.3.5 Plutonium ^{238}Pu, ^{239}Pu, ^{240}Pu

It is a silver-gray radioactive element that changes color to yellow when in contact with air [56]. Plutonium ^{238}Pu belongs to the group of fertile isotopes (α decay). The half-life is 87.7 years. Plutonium ^{239}Pu is classified as fissile isotopes (α decay). The half-life is $2{,}41 \times 10^4$. Plutonium ^{239}Pu is produced by the radioactive decay of uranium ^{238}U. Neutron absorption produces ^{239}U with a half-life of 23.5 minutes. The β decay of uranium ^{239}U produces neptunium ^{239}Np with a half-life of 2.36 days. The final phase of the entire nuclear fission is β decay to ^{239}Pu [57].

$$^{238}_{92}U + ^{1}_{0}n \rightarrow ^{239}_{92}U \xrightarrow[23.5\ min]{\beta^-} ^{239}_{93}Np \xrightarrow[2.35\ min]{\beta^-} ^{239}_{94}Pu \qquad (1.\ 4)$$

Plutonium ^{240}Pu belongs to the group of fertile isotopes (α decay). The half-life is 6.564 years [57].

In the natural environment, the concentration of plutonium is very low. Plutonium is produced in nuclear weapons tests and in nuclear reactors. It is used in space projects as a source of energy or to produce nuclear weapons [56].

Figure 25. Installation of one of three radioisotope thermoelectric generators (RTG) on the Cassini spacecraft (Plutonium ^{238}Pu) [58].

Plutonium particles are harmful if inhaled. These particles are deposited in the lungs and can continue into the bloodstream. This can cause more serious diseases such as cancer of lungs or other organs [56].

1.3.6 Strontium ^{90}Sr

It is a soft, silvery metal that turns yellow when it reacts with air. The half-life is 29 years [59]. Strontium ^{90}Sr is produced during nuclear fission in nuclear reactors or during nuclear weapons tests [60]. Strontium ^{90}Sr is converted to yttrium ^{90}Y during β decay, which has a half-life of 64 hours. The final stable element is zirconium ^{90}Zr [46].

$$^{90}_{38}Sr \xrightarrow[28\ y]{\beta^-} {}^{90}_{39}Y \xrightarrow[64\ h]{\beta^-} {}^{90}_{40}Zr \qquad (1.\ 5)$$

Strontium ^{90}Sr occurs in nature in very small amounts. These are the remains of nuclear tests in the atmosphere and nuclear accidents [59].

1.3.7 Technetium ^{99}Tc, ^{99m}Tc

It is a silver-gray radioactive metal. Technetium ^{99}Tc has a half-life of $2{,}11 \times 10^5$. Technetium is produced in nuclear reactors and during nuclear weapons tests. Technetium ^{99m}Tc is a metastable element with a half-life of 6 hours. Technetium ^{99m}Tc is used in medical diagnostic devices [61].

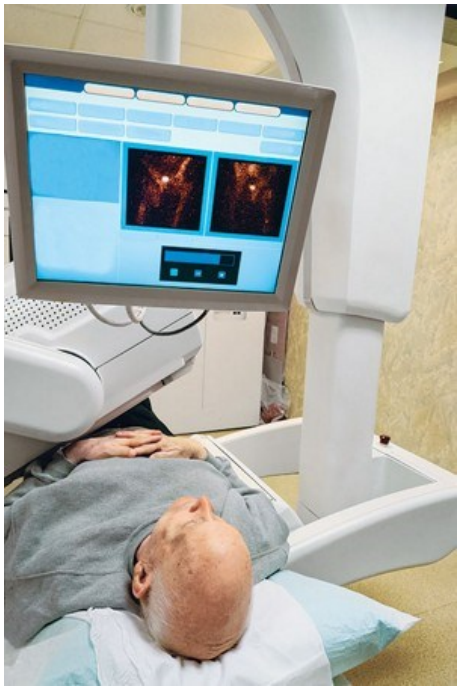

Figure 26. Use of technetium ^{99m}Tc in gamma camera diagnostics [62].

2 IONISING RADIATION LOAD ON THE LANDSCAPE

A certain comfort is important for today's society without which we cannot imagine life. As the population grows, great demands are being placed on the energy, engineering, military, food, agricultural and pharmaceutical industries. In all these industries we can find the origin of the current increase in the country's ionizing radiation burden.

2.1 Combustion of Coal and Fossil Fuels

A large part of the production of electricity and heat is based on the classical combustion of fossil fuels [63]. When burning coal or oil, radioactive elements such as uranium ^{238}U and thorium ^{232}Th are released [64]. It can also be arsenic, radium, radon, polonium and mercury. A coal-fired power plant produces ten times more radiation than a nuclear power plant when producing the same amount of energy [65].

- For a thermal power plant, the dose equivalent from operation for a person is 0.3 μSv per year (distance from the power plant 80 km).
- For a nuclear power plant, the dose equivalent from operation for a person is 0.09 μSv per year (distance from the power plant 80 km) [11].

2.2 Phosphate Industry

Another activity by which humans influence the radiation load on the landscape is the phosphate industry. These are mainly phosphate fertilizers which contain uranium ^{238}U, thorium ^{232}Th, potassium ^{40}K. It can also be the radioactive elements polonium ^{210}Po, lead ^{210}Pb, radium ^{226}Ra [66].

Figure 27. Use of phosphate fertilizers in the agricultural industry [67].

2.3 Nuclear Weapons Tests

The beginning of the nuclear age began on 16 July 1945 with the first successful explosion of the atomic bomb. This test was conducted at Los Alamos, New Mexico, under the code name "Trinity". From that date on, the race to develop nuclear weapons began. Tests were conducted all over the world and in different environments. These included detonating nuclear bombs in the atmosphere, on land, underwater (at a depth of ~600m), underground (at a depth of ~2400m) or in horizontal tunnels [68].

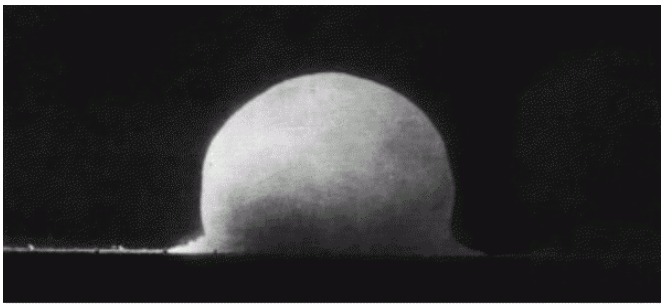

Figure 28. The first nuclear explosion during the Trinity test [68].

2.3.1 Atmospheric Nuclear Weapons Tests

These were tests at high altitudes in the atmosphere. Of the more than 2,000 tests conducted during 1945 to 1998, 25% were in the atmosphere [68]. This amounts to approximately 440 Mt. Tests in the USA were conducted at low latitudes. In the USSR, tests were conducted at high latitudes. Other tests were conducted by China, which designated an area in the central part of the northern hemisphere. In the case of France and Great Britain, atmospheric tests were conducted in the southern hemisphere [69].

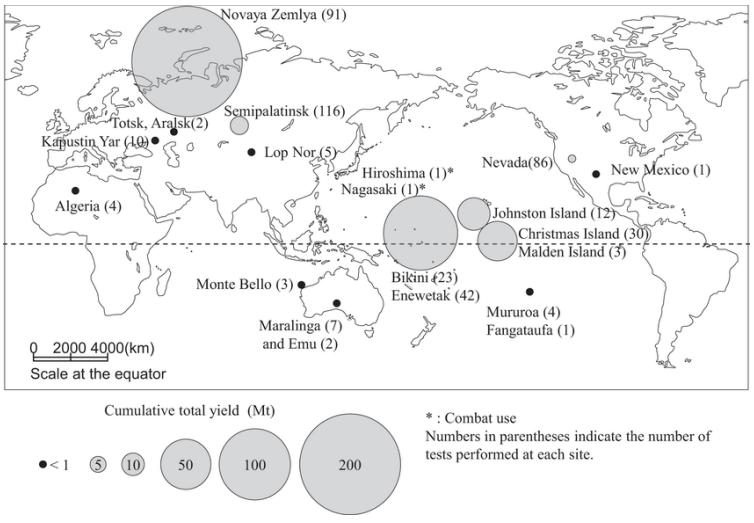

Figure 29. Map of nuclear test locations [69].

Nuclear explosions release artificial radionuclides into the upper atmosphere and disperse them over long distances. The strongest fallout was after atmospheric tests in the early 1960s. Among the radioactive elements that formed the main fallout are cesium ^{137}Cs and strontium ^{90}Sr [70]. Other radioactive elements may include americium ^{241}Am, iodine ^{131}I, plutonium ^{238}Pu, and plutonium ^{239}Pu [72; 73].

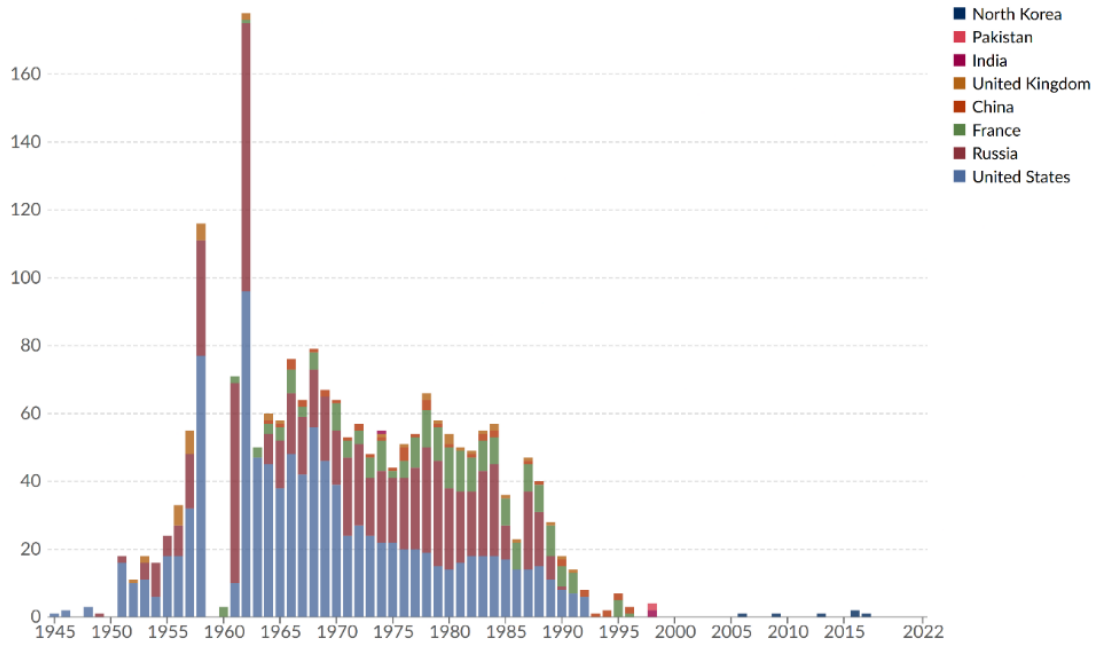

Figure 30. Nuclear test intensity from 1945 to 2022. The graph shows the number of nuclear tests on the vertical axis and the number of years on the horizontal axis [73].

Table 1. Radionuclides and their levels dispersed into the atmosphere during nuclear tests from 1945 to 1980. The data come from Argentina, Denmark and the United States of America [74].

Radionuclides	Half-life [E7]	Decay mod	Fission yield (%)	Estimates of amounts released into the atmosphere (excluding local fallout)		
				Total (F.Bq)	Normalized release (PBq Mt^{-1})	
					Fission	Fusion
^{3}H	12.32 a	β	-	240	0.026	740
^{14}C	5730 a	β	-	0.22	-	0.67
^{54}Mn	3125 d	EC, γ	-	5.2	-	15.9
^{55}Fe	2.74 a	EC	-	2	-	6.1
^{89}Sr	50.55 d	β	2.56	91.4	590	-
^{90}Sr	28.6 a	β	3.50	0.604	3.90	-
^{91}Y	58.51 d	β	3.76	116	748	-
^{95}Zr	64.03 d	β, γ	5.07	143	922	-
^{103}Ru	39.25 d	β, γ	5.20	238	1540	-

^{106}Ru	371.6 d	β, γ	2.44	11.8	76.4	-
^{125}Sb	2.73 a	β, γ	0.29	0.524	3.38	-
^{131}I	8.02 d	β, γ	2.90	651	4200	-
^{137}Cs	30.14 a	β, γ	5.57	0.912	5.89	-
^{140}Ba	12.75 d	β, γ	5.18	732	4730	-
^{141}Ce	32.50 d	β, γ	4.58	254	1640	-
^{144}Ce	284.9 d	β, γ	4.69	29.6	191	-
^{239}Pu	24100 a	β, γ	-	0.00652	-	-
^{240}Pu	6560 a	β, γ	-	0.00435	-	-
^{241}Pu	14.4 a	β	-	0.142	-	-

Table 2. Average measured levels of the radionuclide's cesium ^{137}Cs and strontium ^{90}Sr in food in atmospheric tests from 1945 to 1980. Data are from Argentina, Denmark and the United States of America [74].

Component	Transfer factor	Contribution to total transfer	Contribution to component transfer from food categories (%)				
			Milk	Grain	Vegetables	Fruit	Meat
^{90}Sr							
Direct deposition	0.8 ± 0.4	22%	43%	38%	6%	8%	5%
Lagged transfer	1.0 ± 0.8	27%	23%	72%	0.4%	2%	3%
Transfer from deposit	1.8 ± 0.6	51%	32%	28%	26%	10%	4%
Total transfer	3.6 ± 1.7	100%	32%	42%	15%	7%	4%
^{137}Cs							
Direct deposition	3.8 ± 0.4	45%	36%	11%	13%	5%	35%
Lagged transfer	2.9 ± 0.4	35%	15%	71%	8%	6%	0%
Transfer from deposit	1.7 ± 1.0	20%	15%	4%	7%	7%	67%
Total transfer	8.4 ± 2.8	100%	25%	30%	10%	6%	29%

The last atmospheric nuclear test occurred in the Makan Desert in Xinjiang Province, China, on 16 October 1980 [75]. This test was documented in detail, including atmospheric air movements with migrations of radioactive isotopes. [76].

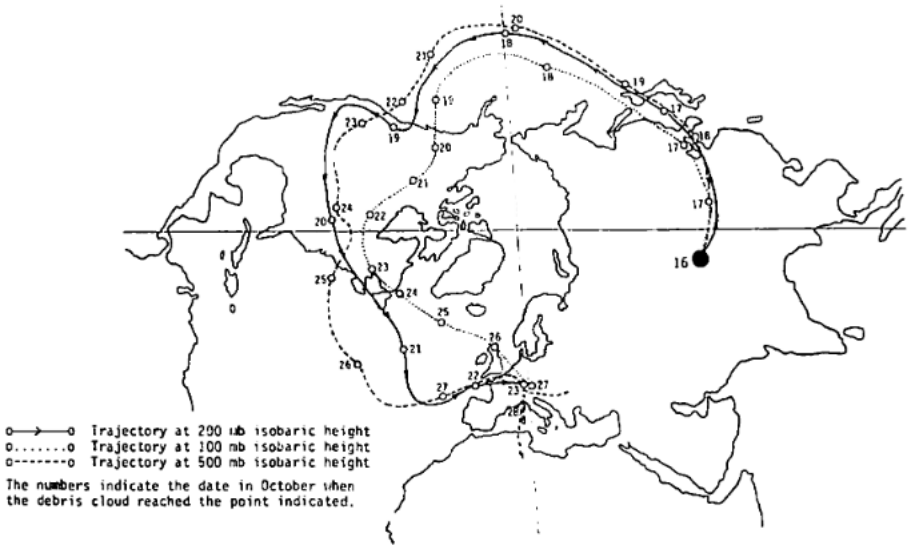

Figure 31. Meteorological data of airborne migration of radioactive isotopes during the Chinese atmospheric nuclear test on 16 October 1980 [76].

The average residence time of particles in the lower stratosphere ranges from 3 to 12 months in the polar regions. In the equatorial regions, the residence time of particles varies from 8 to 24 months. Important factors for the migration of radioactive isotopes in nuclear tests are air currents, latitude and season. [76].

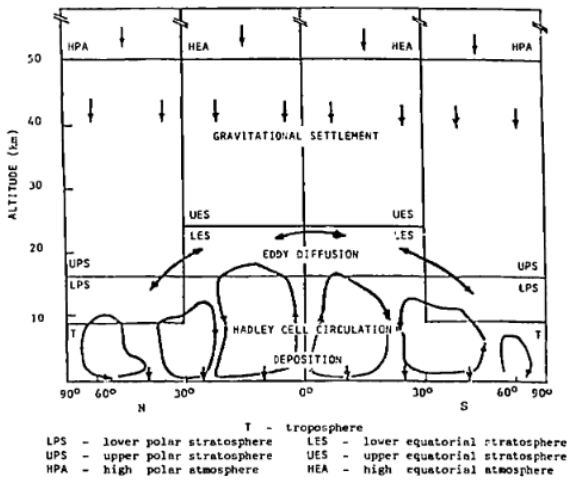

Figure 32. Atmospheric layers and the principle of atmospheric transfer of radioactive isotopes [76]

Within the Czech Republic, surface radioactive loadings of cesium ^{137}Cs, strontium ^{90}Sr originate from nuclear tests in the 1960s and after the Chernobyl nuclear power plant accident [77]. Fallout values from nuclear tests in the Northern Hemisphere between $40^o - 50^o$ were as high as (5 kBq/m^2) for cesium ^{137}Cs and for strontium ^{90}Sr (3,23 kBq/m^2) [78].

2.4 Nuclear Power Plant Accidents

The world is currently facing major challenges in energy production and distribution. The problem of safe and low-carbon energy infrastructure is being addressed globally [79]. Climate change is forcing a transformation of energy dependence on fossil fuels. Renewables and nuclear energy play an important role in the decarbonization set. The intensive deployment of renewable technologies is also driven by concerns about possible nuclear power plant accidents in the past [80].

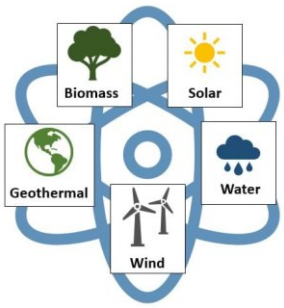

Figure 33. Renewable sources of electricity production [81].

This mistrust is linked to two nuclear accidents that had a global impact. These are the Chernobyl accident and the Fukushima accident [82].

2.4.1 The Accident at the Chernobyl Nuclear Power Plant

The Chernobyl accident was the first nuclear accident to affect the whole world. The accident immediately claimed 29 human lives and many more lives after the exposure and subsequent fallout of radioactive material [83].

The crash occurred on April 26 at 1:24 1986. The main cause of the accident was a design flaw in the reactor and a violation of safety rules. As a consequence of these errors, two consecutive explosions occurred, which destroyed the reactor, the reactor building and the engine room [84].

These two thermal explosions were the initial release of radioactive material into the surrounding area. The dispersal occurred in the form of a plume that reached into the atmosphere. The subsequent fire resulted in the continued release of large amounts of radioactive material into the atmosphere [84].

Figure 34. The destroyed 4th unit of the nuclear power plant in Chernobyl [84].

Radioactive particles were quickly dispersed across Europe by atmospheric currents. Belarus, Ukraine, and Russia were the most affected. These were mainly iodine ^{131}I and cesium ^{137}Cs [83]. Overall, radioactive material was dispersed throughout the northern hemisphere and was also measured in Japan [84].

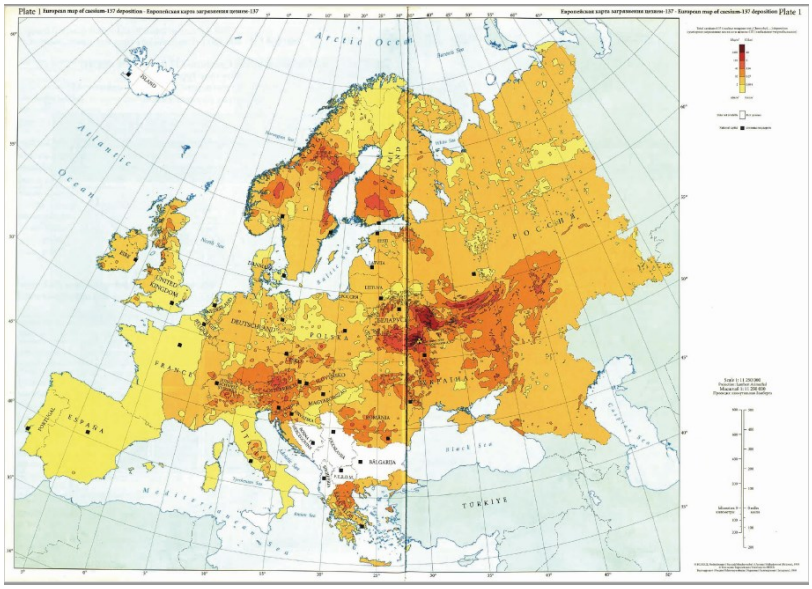

Figure 35. A map from 1986 shows cesium ^{137}Cs fallout values after the Chernobyl nuclear power plant accident [84].

Within the Czech Republic, several area measurements for radioactive fallout after the Chernobyl accident were carried out. The hunger measurements were carried out between 16 and 18 June 1986. Sites were selected for this purpose that were not shaded by buildings, bushes and trees. Another condition was that the land had not been cultivated since 26 April 1986.

Samples were taken from areas of 0.09 m^2 to a depth of 3 cm. The soil was dried before the actual measurements. Studies from other years are not included here because of sampling from greater depths. These were mostly at depths of 20 cm, where cesium ^{137}Cs radionuclides from the Chernobyl nuclear power plant accident and atmospheric nuclear tests are already intermingled [85].

Table 3. Mean values of a survey conducted in 1986 [85].

Data from the period	Number of data	Arithmetic mean	
from 1. 5. 1986	909	4242	Bq/m^2
from 6. 5. 1986	868	4147	Bq/m^2
from 10. 5. 1986	846	4143	Bq/m^2
16.6. - 18. 6. 1986	798	4199	Bq/m^2

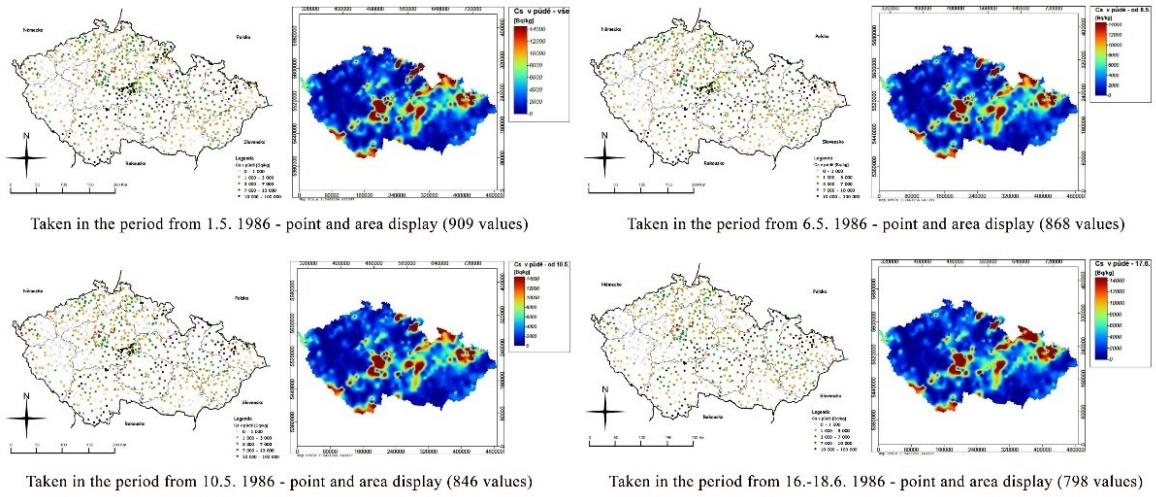

Figure 36. The contaminated area of the Czech Republic with cesium ^{137}Cs as a result of the Chernobyl nuclear power plant accident. Correction the correct unit in the legend is Bq/m^2 [85].

2.4.2 The Accident at the Fukushima Daiichi Nuclear Power Plant

The accident at the Fukushima nuclear power plant occurred on 11 March 2011 at 14:46. It was caused by an earthquake measuring 9 on the Richter scale, the epicenter of which was 130 km from Sendai in Miyagi Prefecture on the island of Honshu. The subsequent tsunami inundated approximately 560 km^2. There were no casualties from the nuclear accident, with only three plant workers dying in the earthquake and tsunami [86].

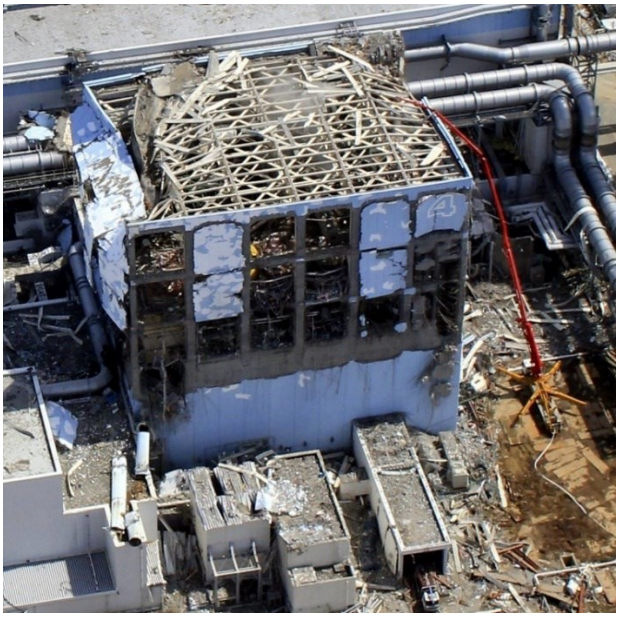

Figure 37. The destroyed building of reactor No. 4 of the Fukushima Daiichi nuclear power plant [87].

This earthquake confirmed the shock resistance of all the reactors at Fukushima, but the primary power supplies were damaged in the tremors. As a result of this loss, backup diesel generators were automatically started to keep the reactors' cooling systems running. As a result of the successive tsunami waves, the generators and switchgear were flooded. These events led to the failure of the power supply, which played an important role in cooling the reactor. Overall, several hydrogen explosions occurred, but did not significantly damage the reactors [86].

Post-accident cesium contamination measurements and analysis were carried out at 81 sites from 12 to 22 December 2011. In addition, the periods were 17-19 April 2012 at three sites, 21 August to 26 September 2012 at 85 sites and 26 November to 26 December 2012 at 85 sites. Three mixes were in zones up to 20 km that were closed to the public. The sampling radius was up to 100 km. When the measured samples were evaluated, most of the radioactive cesium was found to be within 5 cm [88].

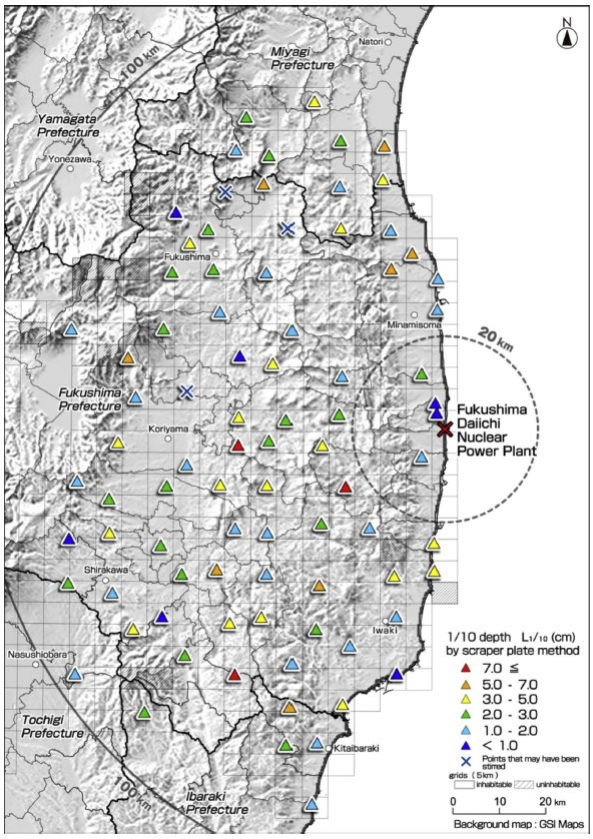

Figure 38. Locations where cesium values were measured in 2011-2012 [88].

Average measured values with cesium ^{137}Cs readings from December 2011, August 2012 and November 2012 [88]:

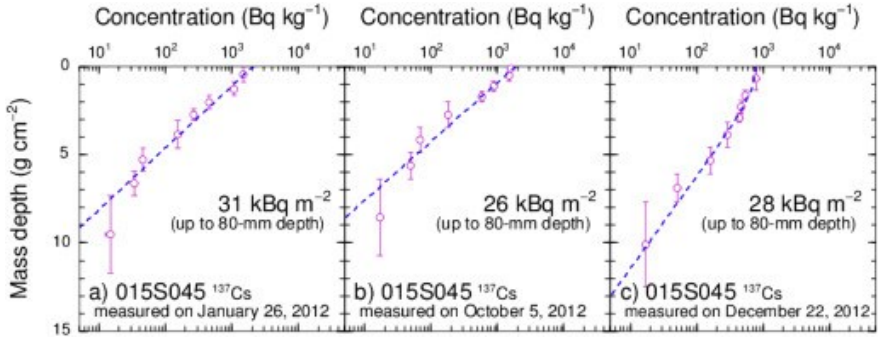

Figure 39. Depth profiles for ^{137}Cs concentration versus mass depth (wet weight) [88].

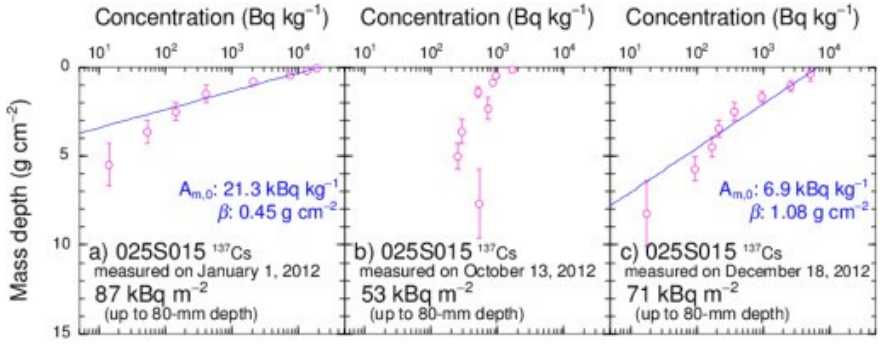

Figure 40. Depth profiles for ^{137}Cs concentration versus mass depth (wet weight). For the measured values of (b), this was a mixing of layers due to human activities or natural processes [88].

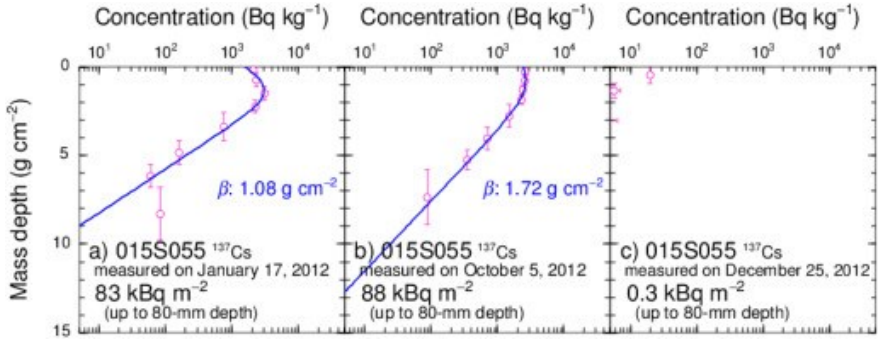

Figure 41. Depth profiles for ^{137}Cs concentration versus mass depth (wet weight). The measured values of c) were the influence due to decontamination works [88].

2.4.3 Vertical Migration of Cesium ^{137}Cs

Studies have shown that soil properties such as soil organic content, acidity and weather conditions have an influence on the increasing residence time and migration of cesium ^{137}Cs in natural ecosystems. The type of biomass exposed to this migration of cesium ^{137}Cs is very important. Very slow migration occurs in the humic horizon at approximately 0.04 - 0.06 cm/y. In contrast, rapid migration occurs in peat soils [46].

In the study of the environmental impact of the Fukushima accident, measurements were made on the vertical migration of cesium ^{137}Cs and cesium ^{137}Cs. Samples were collected within a 20 km perimeter of the plant during November 2012 and July 2013. When the measurements were analyzed, the migration of cesium ^{137}Cs was faster in forest soil compared to grassed areas. From the data, migration rates were found to be 1.1 - 1.7 cm/y for grassland and 0.85 - 3.5 cm/y for forest soil [89].

The accident contaminated many orchards in Fukushima Prefecture with cesium ^{137}Cs. This is a risk of transfer of cesium ^{137}Cs to fruit-bearing plants via the root system and thus a longer persistence of cesium ^{137}Cs in the soil layers. Furthermore, the use of nitrogen fertilizers and their effect on the vertical migration of cesium ^{137}Cs has been compared [90].

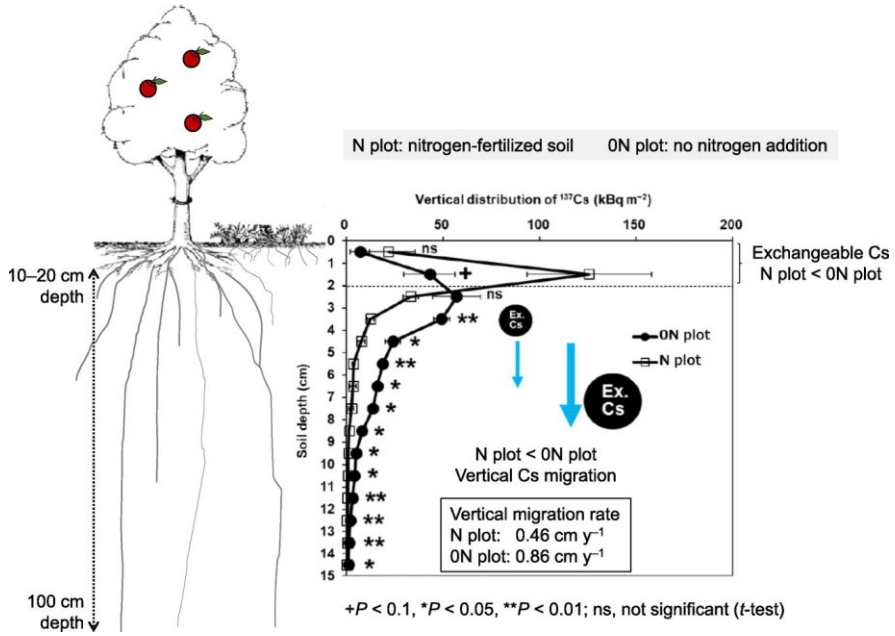

Figure 42. Nitrogen fertilizers and their effect on the vertical migration of cesium ^{137}Cs [90].

2.5 Detection and Measurement of Ionizing Radiation

Many detectors and spectrometers are used to detect ionizing radiation. These devices use different physical principles and modern technologies [91].

The detectors are divided [91]:

1. Detectors according to the time course of detection
2. Detectors according to the detection principle
3. Detectors according to the complexity of the measured information

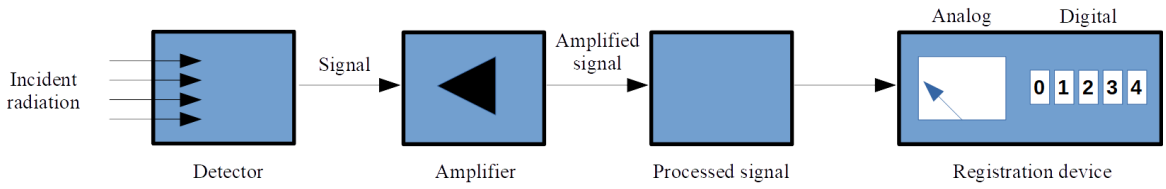

Figure 43. Detection device [91].

2.5.1 Detectors According to the Time Course of Detection

- Continuous "on-line" detectors – detection of instantaneous radiation intensity or number of quanta of ionizing radiation. If the detector stops irradiating, the signal at the output drops to the background value or to a value equal to zero.
- Cumulative integral detectors – during exposure, detectors accumulate increasing denoise. The signal or measurement result remains in the detector and thus there is an additional evaluation of the measurement after the exposure has ended [91].

2.5.2 Detectors According to the Detection Principle

- Photographic detectors – detectors work on the principle of photochemical effects of radiation (nuclear emulsions, X-ray films, film dosimeters). In addition, it can be the use of photographic imaging of traces of particles in a material environment (bubble or fog chambers) [91].

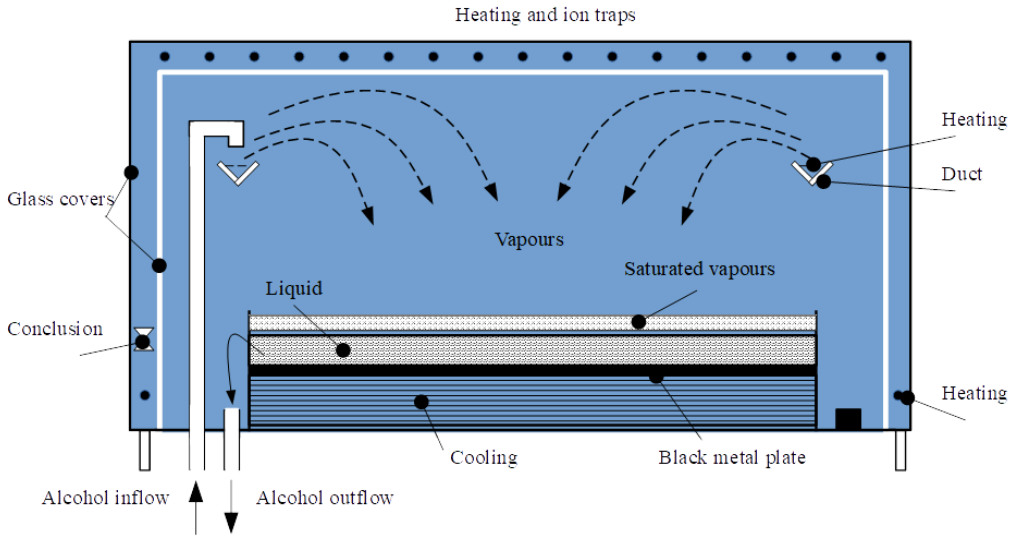

Figure 44. Wilson's fog chamber [91].

- Electronic detectors – the energy of ionizing radiation is converted into an electric current or pulse and then evaluated in electrical circuits. These are, for example, scintillation detectors, magnetic spectrometers or semiconductor detectors [91].

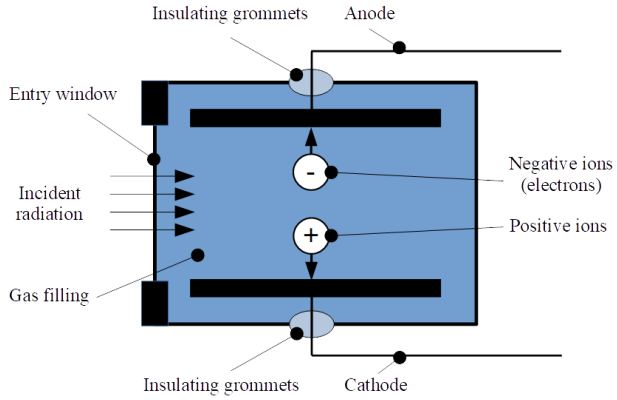

Figure 45. Principle of ionization chamber with gas filling [91].

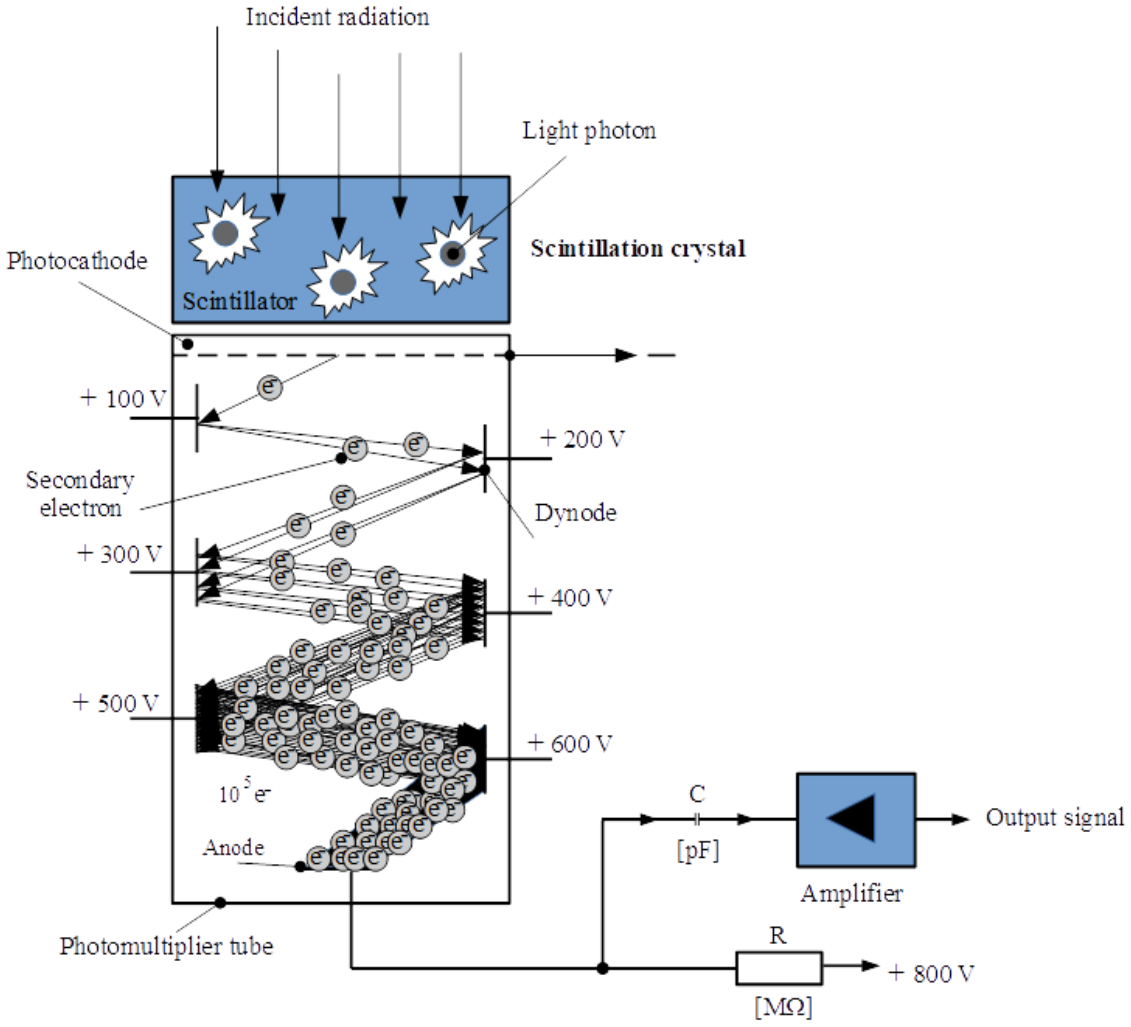

Figure 46. The principle of the scintillation probe [91].

- Material detectors - detectors based on the principle of long-term changes in the properties of liquids. These are, for example, trace detectors. The impact of particles causes small disturbances in the crystal lattice of certain materials. These are micas, special glasses, or organic polymers [91].

2.5.3 Detectors According to the Complexity of the Measured Information

- Detectors – measure only the intensity of radiation (number of radiation quanta). They do not provide information about the type of radiation and its energy. These are, for example, ionization chambers, GM detectors or thermoluminescence dosimeters.
- Spectrometers – these devices measure the intensity and number of quanta of radiation. These devices include, for example, scintillation detectors, magnetic spectrometers, or semiconductor detectors [91].

II. ANALYSIS

3 MEASUREMENT OF IONIZING RADIATION IN NATURAL AND LABORATORY CONDITIONS

At the beginning, it was necessary to create a list of equipment and tools that would be required for the surface measurement and excavation work. It was also important to establish a schedule and procedure for the work to be carried out. This involved creating a timeline so that the progression of the exterior work corresponded with the seasons.

For the surface measurements, the period from February to May was chosen. It was easier to move around the field during this period. The soil was frozen and the sown field crops were not sufficiently grown.

The period from June to July was chosen for excavation. The summer period was important for drying out the excavation layers, which were later transported to the laboratory.

The final stage was to schedule laboratory measurements at the Faculty of Applied Informatics of UTB in the Forensic Sciences Laboratory.

3.1 Measuring Components

For measurement and precision work I used:

- GT40 - multi-purpose gamma spectrometer
- Laser level EINHELL TC - LL 1 Classic
- Wooden measuring bar
- Mortar bucket PE 50 l
- Laptop Dell Inspiron 5770
- GEOMON software for the GT 40 gamma spectrometer
- ArcGIS Pro software
- Lead box FAI UTB (forensic laboratory)
- Laboratory scale Entris 822 - 1S
- Home scale
- Tripod for digital spirit level
- Lead Meter

3.1.1 GT 40 – Multipurpose Portable Gamma Spectrometer

The multi-purpose portable gamma spectrometer is designed to detect radiation with high sensitivity for both survey and determination of nuclide abundances and activities. This detector has a detection sensitivity range from 15 keV to 3000 keV. The sensitivity for 1 MBq ^{137}Cs at distance of 1 m is 386 imp/s. Other detector parameters [92]:

- NaI (Tl) detector, volume 345 cm^3, diameter 76 x 76 mm, bi-alkaline photomultiplier.
- DSP Linearized spectrometer 1024 channel, 40 MHz. Superimposed pulse eliminator, resolution 200 ns.
- Automatic energy calibration of spectrometer based on natural background radiation of potassium ^{40}K, uranu ^{238}U, thoria ^{232}Th.
- Algorithm for evaluating the abundances or activities of up to 6 selected radionuclides in different geometries.
- Integrated GPS module.
- Integrated microphone for voice recording.
- Internal rechargeable Li-ion battery module.

Calibration Reference Point

The GT-40 is equipped with a 3x3" NaI (Tl) detector. It is a scintillation assembly that contains a NaI (Tl) crystal. The measurement assumes incident radiation from the underside of the instrument. The calibration reference point of the GT 40 gamma spectrometer is 5.7 cm from the bottom wall in the instrument axis. Based on these data, the gamma spectrometer was carefully placed in the correct position during the measurement. [93].

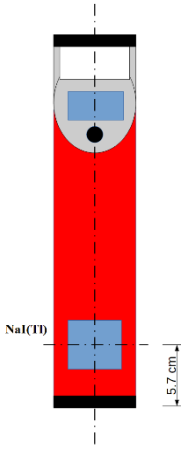

Figure 47. GT 40 gamma spectrometer calibration reference point [93].

Sensitivity Determination

The individual soil contamination determinations at a 300 s time measurement for the minimum detectable content are: potassium ^{40}K - 0.3%, uranium ^{238}U - 0.3 ppm, thorium ^{232}Th - 0.9 ppm and cesium ^{137}Cs - 0.4 kBq/m^2.

Figure 48. GT 40 – multipurpose portable gamma spectrometer.

Basic Procedure for Working with the GT 40 Gamma Spectrometer

When the instrument is switched on, the basic data is displayed, and the spectrometer then enters Survey mode. The instrument is not yet stabilized after startup. This stabilization takes 2 minutes. During this time the energy calibration takes place. When the stabilization icon is displayed, the instrument is ready for measurement [93].

In Survey mode, the instantaneous dose rate value in the selected units is displayed. The accumulated dose rate integral is also displayed. The frequency graph displays the real-time waveform of the frequency of the registered pulses [93].

- BG – background
- DR - batch power input
- Dose - accumulated dose

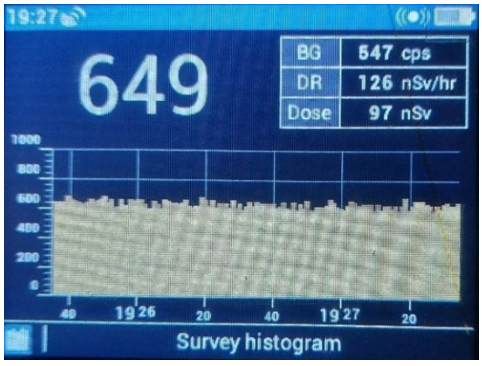

Figure 49. Exploration mode.

Assay Mode

This is a fully automatic mode that evaluates in detail a detailed assessment of the values in the given space.

The GT 40 gamma spectrometer was used in two determination methods [93]:

- Method Geo_300 – Basic method for assay of potassium ^{40}K, uranium ^{238}U, thorium ^{232}Th. This method was used for surface measurement of natural nuclides in the vicinity of Popůvky.

Figure 50. Geo_300 method used.

- Method Area_300E – Method for assay cesium ^{137}Cs in the Northern Hemisphere environment. This method was used: Surface measurement of cesium ^{137}Cs during climatic changes Measurement of samples of natural and artificial ionizing radiation from the excavation. Radionuclides potassium ^{40}K, uranium ^{238}U, thorium ^{232}Th and cesium ^{137}Cs.

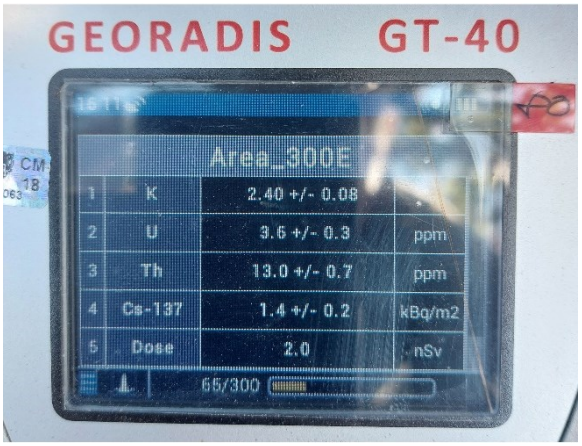

Figure 51. Area_300E method used.

Work with Data

The gamma spectrometer GT 40 has a large memory card for storing metadata, measured data, information from GPS and audio recordings.

Types of sections for displaying data [93]:

- Identification
- Assay
- Device stabilization
- Calibration
- System function logs

3.1.2 Laser Spirit Level EINHELL TC – LL 1 Classic

The laser level helped in accurately sampling each layer in the excavation. It is a commonly available laser level that has a wide range of applications. For example, for levelling work or the precise installation of suspension systems [94].

Figure 52. Laser spirit level EINHELL TC – LL 1 Classic.

Figure 53. Using the EINHELL TC – LL 1 Classic laser spirit level during excavation.

3.1.3 Wooden Measuring Stick

A wooden measuring bar was used to measure the depth of the excavation. The measuring bar was self-built.

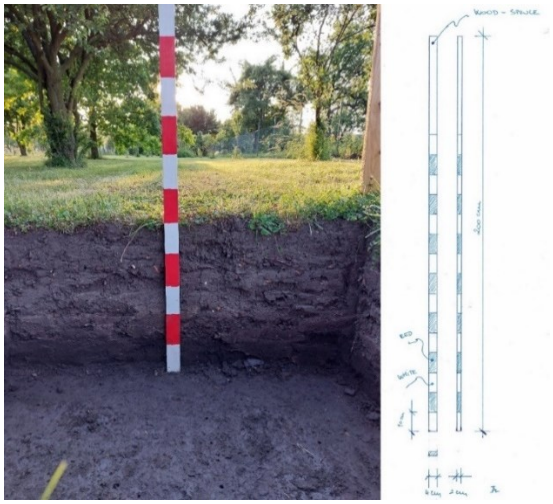

Figure 54. The use of a wooden measuring batten during excavation and a technical drawing of a wooden measuring batten.

3.1.4 PE Mortar Bucket 50 l

He folded the plastic bucket to measure samples from the excavation.

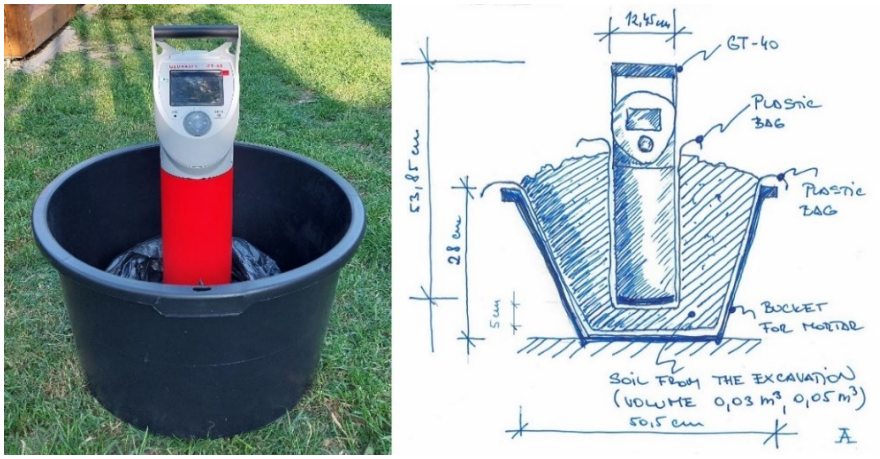

Figure 55. The use of a mortar bucket for outdoor measurements and a technical drawing of the measurement application.

3.1.5 Laptop Dell Inspiron 5770

The laptop was loaned to FAI UTB, for importing data from GT 40 and for visualization in the ArcGIS Pro program.

The parameters of the notebook are:

- Processor - Intel(R) Core (MT) i5-8250U.
- Operating memory - 8 GB.
- System type – Windows 10 Home 64-bit operating system.

3.1.6 GEOMON Software

The GEOMON software version 0.5.53 is part of the GT 40 multi-purpose portable gamma spectrometer. GEOMON is used to determine the measured data from the GT 40 gamma spectrometer [93]. Before connecting the instrument to a laptop, the USB must be set to USB direct mode in the GT 40. The data could be analyzed directly in the program or in my case the data export was used. The exported data was visualized as graphs or in ArcGIS Pro.

Procedure for connecting and exporting data [93]:

1. Connecting the GT 40 to the laptop.
2. Click the Stored data button.
3. Click on the Assay button.
4. Click on the Read assay button.

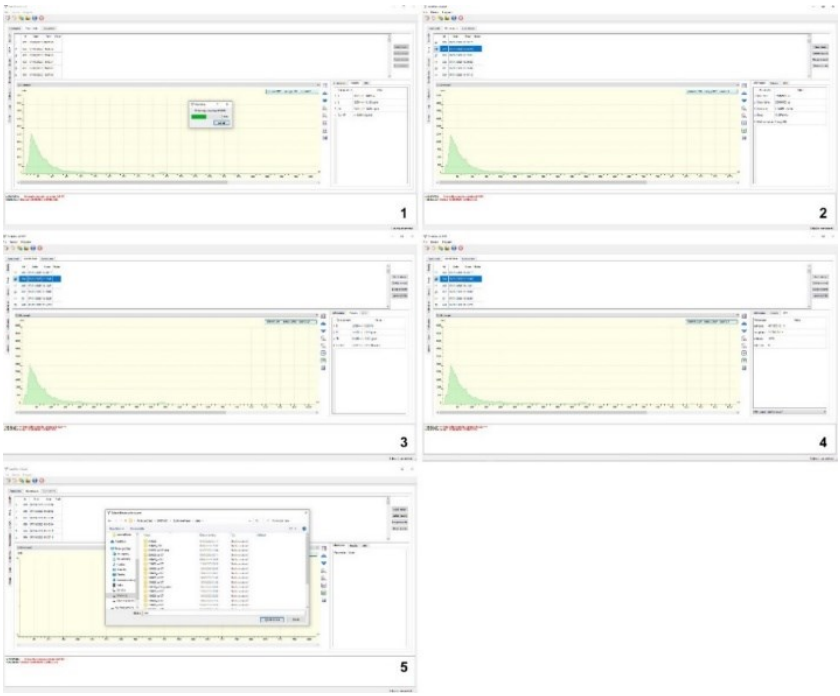

Figure 56. The procedure of loading and exporting the measured data. Figure 1. data loading, figure 2. information about the loaded data, figure 3. result, figure 4. GPS data, figure 5. data export.

3.1.7 ArcGIS Pro

ArcGIS Pro software is a desktop GIS application. ArcGIS Pro is designed for processing spatial data, 2D, 3D, 4D visualizations and for map analysis [95].

ArcGIS Pro was used to visualize data measured during surface measurements of natural ionizing radiation in the vicinity of Popůvky near Kojetín. The data were exported with GT 40 gamma spectrometer to GEOMON. Furthermore, the data were saved with GEOMONT in .csv format, which was opened in Microsoft Excel and then saved in .xls format. The data were then imported into ArcGIS Pro. Here, the data were attached using attribution tables to the layers based on the coordinates that were part of the GT 40 gamma spectrometer data.

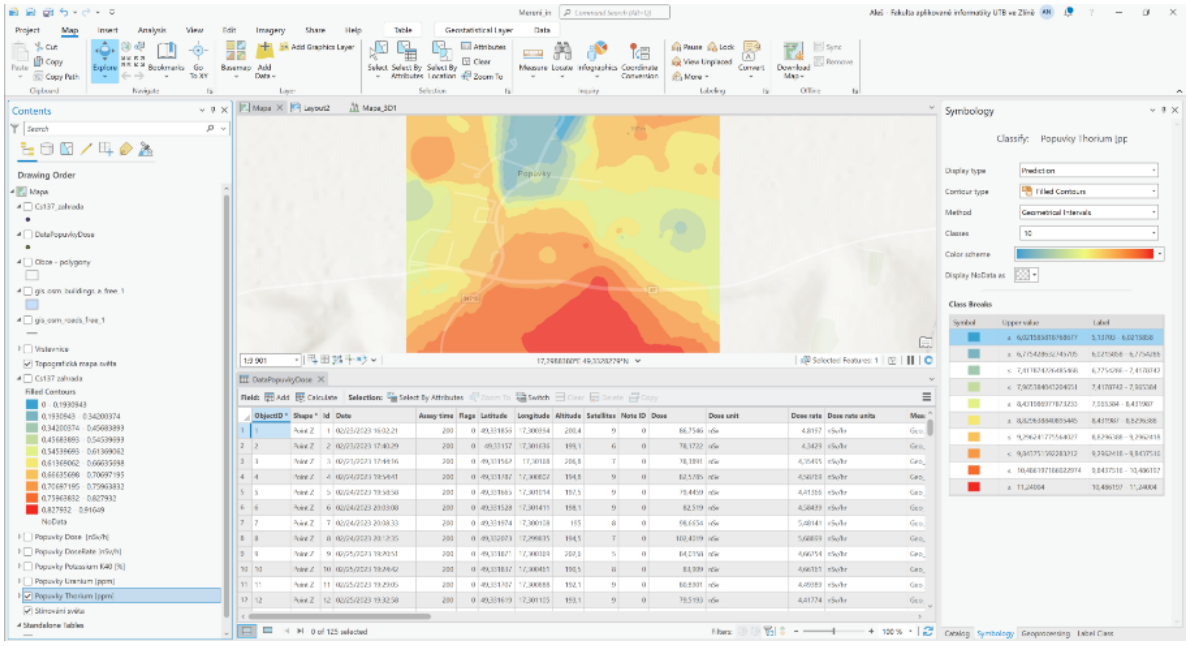

Figure 57. The ArcGIS Pro program environment and a sample of measured data processing.

3.1.8 Lead Box

The lead box was used to minimize background values that would increase the measurement uncertainty. The dimensions of the box base are 0.4 x 0.05 x 0.4 m. The box itself has external dimensions of 0.3 x 0.3 x 0.35 m.

Figure 58. The lead box is part of the FAI UTB forensic laboratory.

3.1.9 Laboratory Balance Entris 822 – 1S

The laboratory scale was used to determine the weight of individual findings in individual layers. It is a scale with a maximum capacity of 820 g and external calibration [96].

Figure 59. Laboratory balance Entris 822 – 1S.

3.1.10 Home Scale Eta 0775

The home scale was used to accurately weigh the layers removed from the excavation, for laboratory measurements. The maximum weight capacity is 150 kg.

Figure 60. Home scale Eta 0775.

3.1.11 Tripod for Bosch BS 150 Professional Digital Spirit Level

The tripod was used to place the digital spirit level. The horizontal movement of the tripod during measurement with a digital spirit level enabled more accurate removal of individual layers.

Figure 61. Tripod for working with a digital spirit level.

3.2 Surface Measurement of Natural Ionizing Radiation in the Vicinity of the Village of Popůvky Near Kojetín

Surface measurements were focused on the occurrence of natural radionuclides in the selected locality Popůvky near Kojetín. The site is located at an altitude of 194 m with prevailing north-northwest winds. The measurement perimeter was one kilometer with an elevation of 44 meters. In this area measurements of the abundance of primary natural radionuclides potassium ^{40}K, uranium ^{238}U, thorium ^{232}Th were carried out. The measurements were carried out from February to May 2023. The number of measurement points was set at 125 with a measurement time of 200 s.

Figure 62. Measurement of natural ionizing radiation in the vicinity of Popůvky.

Measured average values of natural nuclides:

- Potassium ^{40}K – (1.4 ± 0.1) %
- Uranium ^{238}U – (2.4 ± 0.2) ppm
- Thorium ^{232}Th – (8.5 ± 0.4) ppm

Data were imported into attribute tables within ArcGIS Pro software and further visualized. Using the IDW (Spatial Analyst) function, areas were displayed to determine the abundance values for each radionuclide.

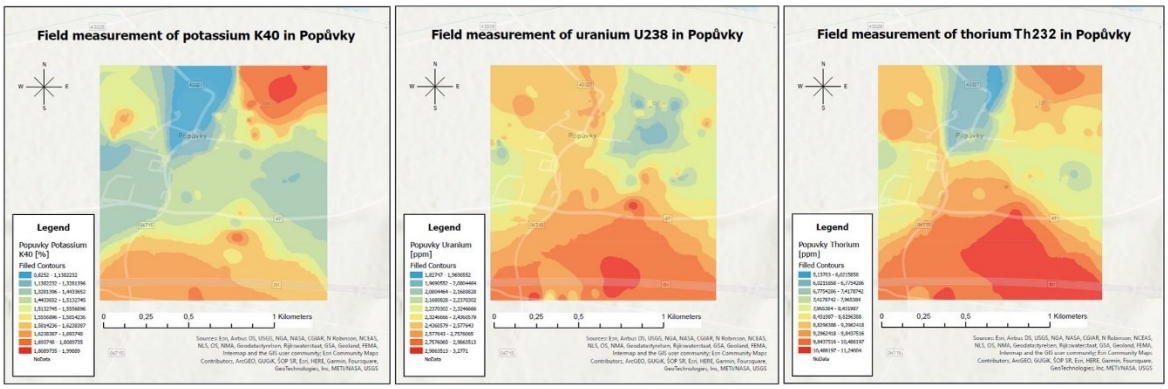

Figure 63. Visualized data from ArcGIS Pro. Surface measurement of potassium ^{40}K, uranium ^{238}U and thorium ^{232}Th in the vicinity of Popůvky.

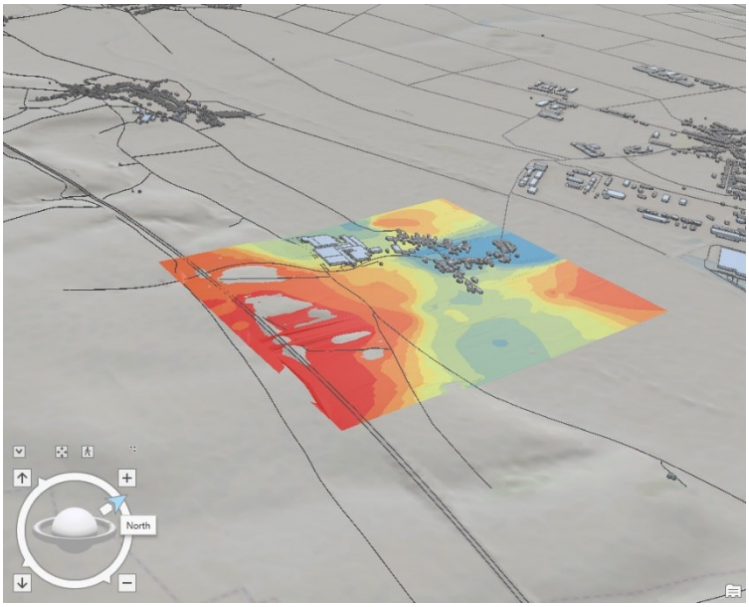

Figure 64. The 3D visualization shows the possible influence of human activity on the concentration of natural radionuclides when burning coal or using phosphate fertilizers.

3.2.1 Evaluation of Surface Measurements of Natural Ionizing Radiation in the Vicinity of Popůvky Near Kojetín

The measured values and their surface distribution point to the possibility of the influence of human activity and its impact on the radiation load on the landscape. This is the effect of coal burning and the use of phosphate fertilizers in agricultural activities.

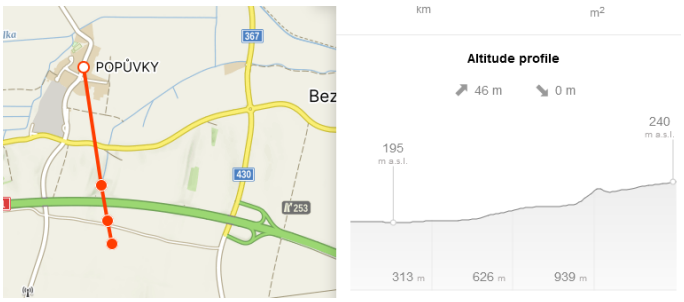

Figure 65. The height profile greatly affects the radiation load of the landscape [97].

During measurements and observations of the landscape around Popůvky, it was concluded that the coal burning in this area has for a long time caused the deposition of natural radionuclides on the northern part of the hilly area Litenčická pahorkatina. This part can be seen from the visualization in ArcGIS Pro. The values with the highest concentrations are located south of Popůvky and are shown in red.

The highest measured values of natural nuclides in the Popůvky area:

- Potassium ^{40}K– (1.9 ± 0.1) %
- Uranium ^{238}U– (3.3 ± 0.2) ppm
- Thorium ^{232}Th – (11.2 ± 0.3) ppm

3.3 Surface Measurement of Cesium During Climatic Weather Changes

Surface measurements of cesium ^{137}Cs during meteorological weather changes were made to compare the behavior of cesium ^{137}Cs during rainy and sunny weather. Cesium ^{137}Cs belongs to the same chemical group as potassium. During soil contamination, cesium is involved in active bio-ecological cycling processes [99].

The first measurement was taken on 1 July 2023 at 11:42 hours. It was a rainy period.

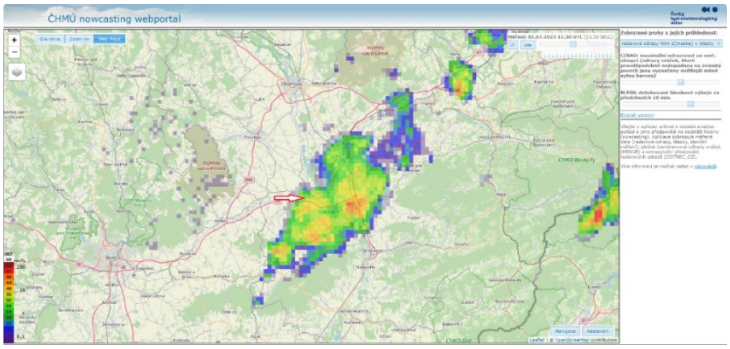

Figure 66. Meteorological situation on 1 July 2023 over the measured area Popůvky [98].

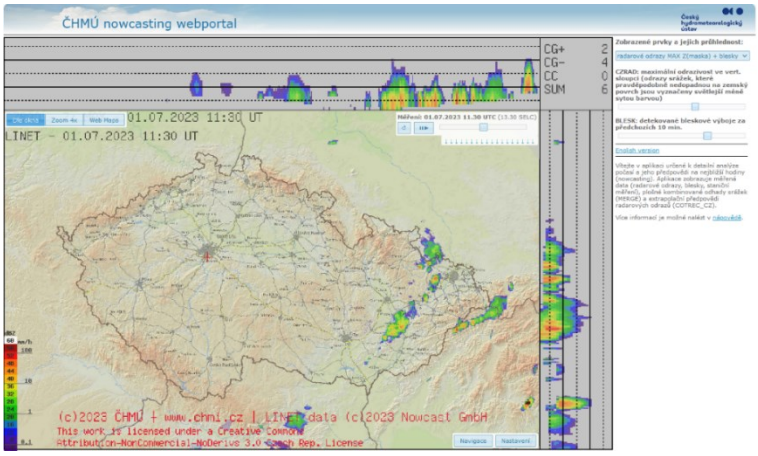

Figure 67. Meteorological situation on 1 July 2023 over the measured area Popůvky [98].

The second measurement was carried out on 16 July 2023 at 18:00. This was a sunny period.

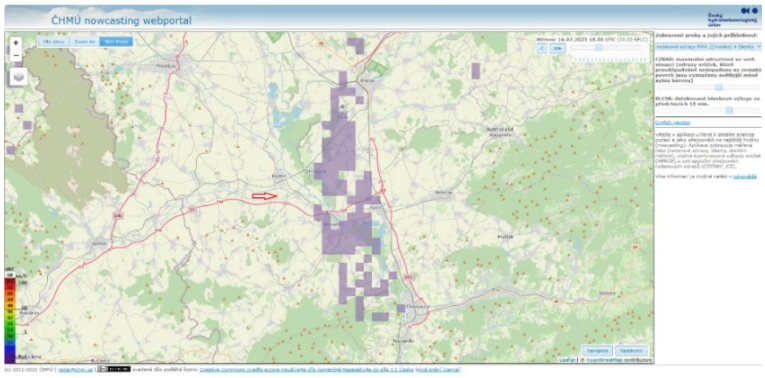

Figure 68. Meteorological situation on 16 July 2023 over the measured area Popůvky [98].

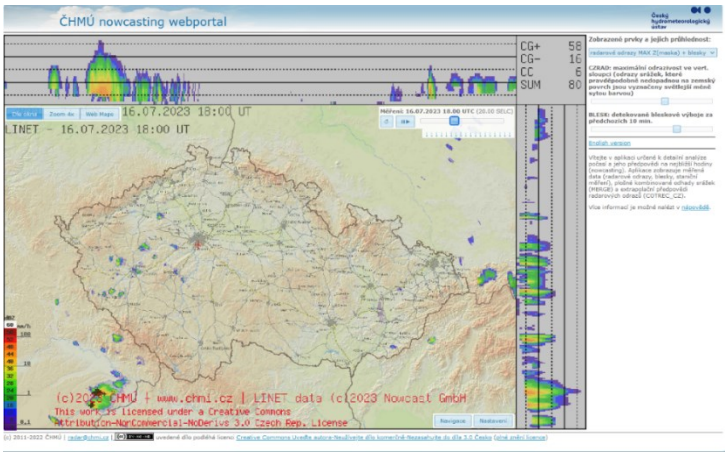

Figure 69. Meteorological situation on 16 July 2023 over the measured area Popůvky [98].

Measured average values:

- Rain: Cesium ^{137}Cs – (0.7 ± 0.2) kBq/m^2
- Sunny: Cesium ^{137}Cs – (1 ± 0.1) kBq/m^2

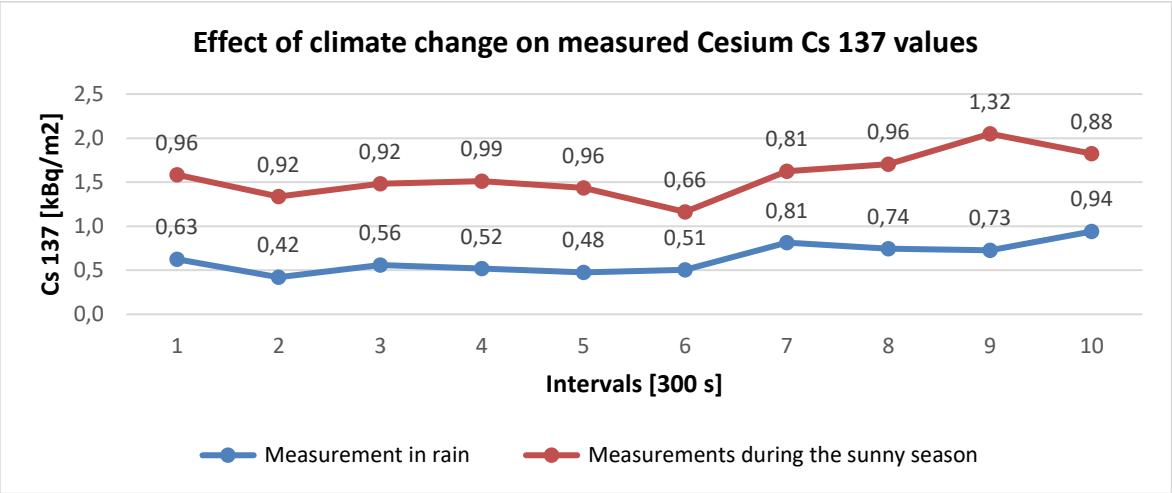

Figure 70. Effect of climate change on measured values of cesium ^{137}Cs.

3.3.1 Evaluation of Cesium Measurements During Climate Change

The measured values show higher cesium ^{137}Cs values in a dry climate. In rainy weather, cesium in the atmosphere is eliminated and therefore measured cesium ^{137}Cs values are lower than in dry and dusty conditions. However, according to a Japanese study, rain-induced circulation processes may also occur in forest environments [99].

3.4 Measurement of Samples of Natural and Artificial Ionizing Radiation from the Excavation

The excavation was carried out in the locality of Popůvky near Kojetín. The condition was to select a site that had not been cultivated for at least 70 years. An orchard on my land was chosen as such a site. This plot is fenced and ensures undisturbed work.

Figure 71. A selected and marked space for carrying out a geological microprobe.

The site for the excavation was chosen near a plum tree that was cut down in 2016. A sample was taken from the stump of the felled plum tree for more accurate dating. Based on the clearly visible tree rings, the approximate time of planting of the tree was determined to be 1911 and the approximate age of the tree to be 105 years.

Figure 72. Area of the excavation with the sampled stump and essential data marked according to the year rings.

The size of the excavation was set at 1 x 1 x 1.3 meters. Using a laser level, a tape measure, and a measuring batten, the thickness of each layer was accurately measured.

Figure 73. The procedure and measurement of the sampling of each layer.

3.4.1 Archaeological Assessment of Individual Layers and Their Dating

Shards of pottery, fist wedges, bone fragments and metal objects were found during the excavation. All finds were documented and marked in which layers they were found.

Figure 74. Documenting findings directly in layers.

To date the individual layers and to create a frame timeline, the entire photo documentation of the finds was sent to the Homeland Museum in Olomouc at the Historical Institute. The archaeologist Lukáš Hlubek dated the finds between the Middle Ages and the Younger Stone Age (Neolithic). The Comenius Museum in Přerov was also contacted to verify the original dating. Archaeologist Mgr. Zdeněk Schenk, PhD. confirmed the dating of the finds.

Figure 75. Documentation of findings in layers.

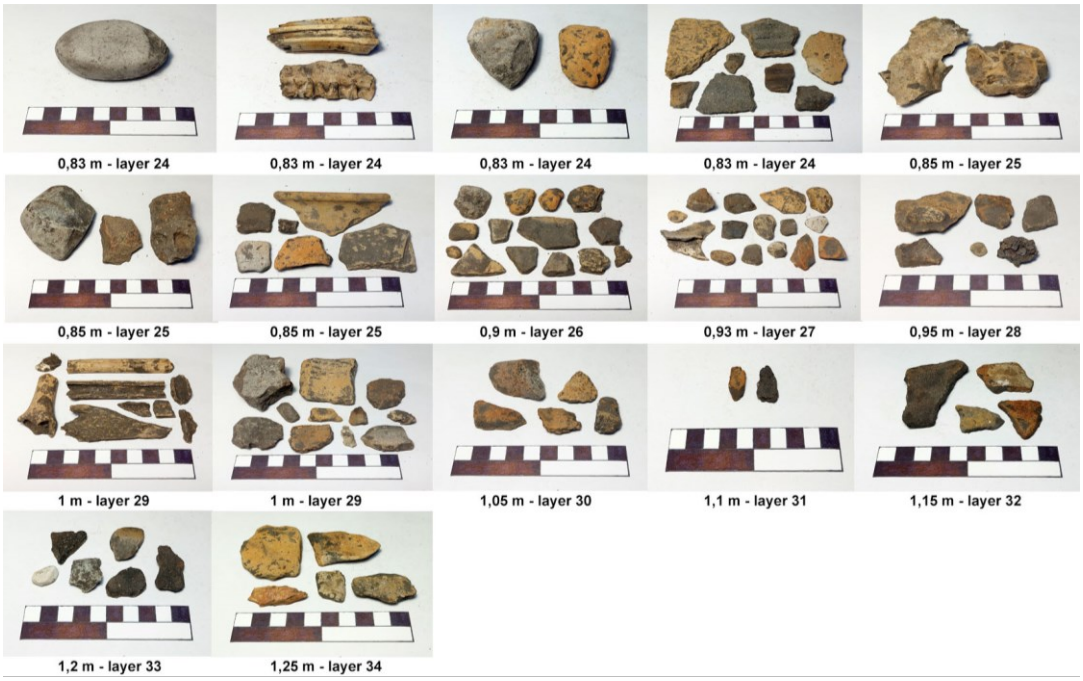

Figure 76. Documentation of findings in layers.

3.4.2 Radiocarbon Dating of Selected Bone Fragments from Individual Layers

The findings of bone fragments in some layers of the geological microprobe played an important role in determining the timeline of the layers.

These were bone fragments at depths of 0.53 m; 0.63 m; 0.73 m; 0.75 m; 0.8 m; 0.83 m; 0.85 m; 0.93 m; 0.95 m and 1 m.

These bone fragments were sent to the Czech Radiocarbon Laboratory. This is a joint workplace of the Institute of Nuclear Physics of the CAS and the Institute of Archaeology of the CAS [100].

All data presented below were obtained from the Czech Radiocarbon Laboratory. A document on the procedure for obtaining radiocarbon dating data is attached in Annex 1.

Radiocarbon dating and carbon ^{14}C analyses using accelerator mass spectrometry (hereafter AMS) were used to determine the timeline. The data were processed using BATS software. This software performed background correction, correction for the effect of fractionation using the $\delta^{13}C$ value measured by AMS and normalization to HOX II standards. The measured activity and the combined carbon uncertainty ^{14}C were expressed in BP (Before Present) years as Conventional Radiocarbon Age (CRA). The combined uncertainty reported for the conventional radiocarbon age values corresponds to a probability of approximately

68%. For a two-sigma uncertainty interval, the determination of 14C activity corresponds to a probability of approximately 95%.

For sample 24_0022, the CALIBomb calibration program was used with a combination of IntCal20 calibration curves. This is a classification dating of northern hemisphere terrestrial samples. Furthermore, the LEVIN program was used, which is designed for bomb peak dating of terrestrial samples originating from Europe. For other samples, the OxCal 4.4 calibration program with the IntCal20 calibration curve was used.

Table 4. Description and characteristics of samples.

Lab. Number	Marking of samples	Material/Properties	Collagen concentration (mg/g)
CRL24_0022	layer 15, 0,53m	bone, stronger, quality 5,5	13
CRL24_0023	layer 18, 0,63m	bone, brittle, quality 4,5	36
CRL24_0024	layer 21, 0,73m	bone, brittle, spongy, quality 5,5	17
CRL24_0025	layer 22, 0,75m	bone, brittle, spongy, quality 5,5 (6)	10
CRL24_0026	layer 23, 0,8m	bone, brittle, spongy, quality 5,5	16
CRL24_0027	layer 24, 0,83m	bone, brittle, quality 5	21
CRL24_0028	layer 25, 0,85m	bone, brittle, quality 5	18
CRL24_0029	layer 27, 0,93m	bone, brittle, spongy, quality 4,5	41
CRL24_0030	layer 28, 0,95m	burnt bone, without the presence of carbonates	-
CRL24_0031	layer 29, 1m	bone, stronger, quality 4,5	31

Evaluation of the quality of the bone/tooth sample: 1 – best, 6 – unsatisfactory. Careful handling of the dating results is recommended for samples with a quality rating of 4.5 and worse.

Table 5. Radiocarbon dating results (calibrated age intervals)

Lab. Number	Marking of samples	Conventional radiocarbon age (BP)	Calibrated age (AD, BC)		P (%)
CRL24_0022	layer 15, 0,53m	119 ± 16	1687 – 1924 AD	connected interval	97
CRL24_0023	layer 18, 0,63m	275 ± 16	1524 – 1662 AD	connected interval	96
CRL24_0024	layer 21, 0,73m	271 ± 18	1524 – 1794 AD	connected interval	97
CRL24_0025	layer 22, 0,75m	340 ± 16	1480 – 1635 AD	connected interval	96
CRL24_0026	layer 23, 0,8m	438 ± 16	1432 – 1466 AD		95
CRL24_0027	layer 24, 0,83m	2227 ± 17	376 – 203 BC	connected interval	96
CRL24_0028	layer 25, 0,85m	2227 ± 17	376 – 203 BC	connected interval	96

CRL24_0029	layer 27, 0,93m	2252 ± 17	390 – 208 BC	connected interval	96
CRL24_0031	layer 29, 1m	2405 ± 18	541 – 403 BC		95

3.4.3 Outdoor Measurement of Excavation Samples

A location closer to the development was determined for the measurement of the sample values due to possible post-wind conditions. Before the actual measurement of the samples, a background measurement was taken so that this value could be subtracted during the actual data analysis to obtain more accurate results. The actual measurement was carried out from 3 June to 1 July 2023.

Figure 77. Space for measurement.

After the measurements, each layer was placed separately in a garden plot, so that the individual layers could later be transported to the Faculty of Applied Informatics at the University of Technology in Zlín for laboratory measurements.

Figure 78. Saving individual layers after measurement.

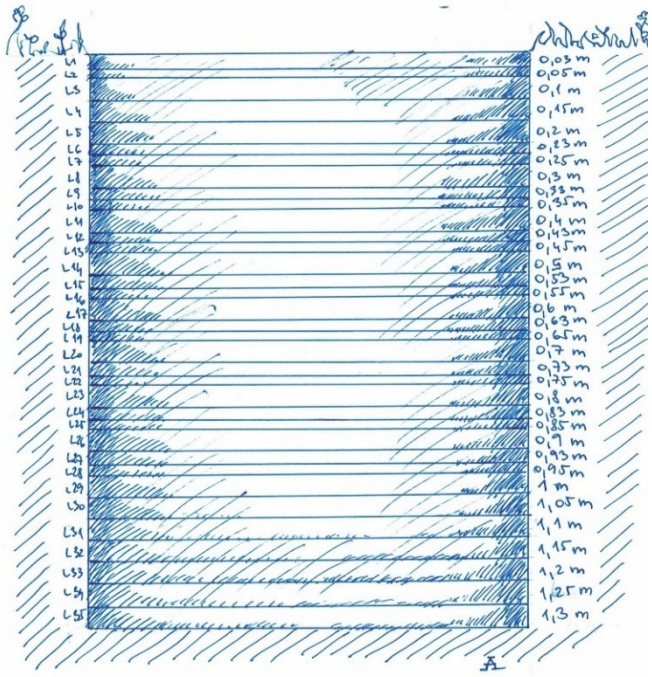

Figure 79. Numbered individual layers taken.

3.4.4 Results of Outdoor Background Measurements

Average measured background values:

- Potassium ^{40}K – (2 ± 0.1) %
- Uranium ^{238}U – (2.9 ± 0.2) ppm
- Thorium ^{232}Th – (9.7 ± 0.3) ppm
- Cesium ^{137}Cs – (0.5 ± 0.1) kBq/m^2

3.4.5 Measurement Results of Potassium ^{40}K, uranium ^{238}U, thorium ^{232}Th from the Excavation

When working in the field, all measurements and documenting the procedures was done as accurately and carefully as possible. When evaluating the data, measurements for each layer were taken at intervals of ten with a duration of 300 seconds. The total weight of soil excavated and measured was 2 tons.

The highest measured values of primordial radionuclides from the geological microprobe:

- Potassium ^{40}K – (0.8 ± 0.1) %, layer 9, depth 0.33 m.
- Uranium ^{238}U – (1.3 ± 0.2) ppm, layer 8, depth 0.3 m.
- Thorium ^{232}Th – (4.8 ± 0.3) ppm, layer 8, depth 0.35 m.

3.4.6 Measurement Results of Individual Layers

Potassium ^{40}K

Table 6. Potassium ^{40}K values after subtracting the measured background.

Layers	K40 [%]	Depth of the measured layer [m]	Background subtraction from measured data K40 [%]	Standard Deviation SD [+/-]	Weight (kg)
L1	2,4	0,03	0,4	0,1	45
L2	2,5	0,05	0,6	0,1	75
L3	2,6	0,1	0,6	0,1	75
L4	2,6	0,15	0,6	0,1	75
L5	2,6	0,2	0,7	0,1	75
L6	2,6	0,23	0,7	0,1	45
L7	2,5	0,25	0,5	0,1	30
L8	2,7	0,3	0,7	0,1	75
L9	2,7	0,33	0,8	0,1	45
L10	2,7	0,35	0,7	0,1	30
L11	2,5	0,4	0,6	0,1	75
L12	2,6	0,43	0,7	0,1	45
L13	2,6	0,45	0,7	0,1	30
L14	2,7	0,5	0,7	0,1	75
L15	2,6	0,53	0,7	0,1	45
L16	2,6	0,55	0,7	0,1	30
L17	2,6	0,6	0,7	0,1	75
L18	2,6	0,63	0,7	0,1	45
L19	2,6	0,65	0,7	0,1	30
L20	2,6	0,7	0,6	0,1	75
L21	2,6	0,73	0,6	0,1	45
L22	2,6	0,75	0,7	0,1	30
L23	2,5	0,8	0,6	0,1	75
L24	2,6	0,83	0,7	0,1	45
L25	2,6	0,85	0,7	0,1	30
L26	2,6	0,9	0,6	0,1	75
L27	2,7	0,93	0,7	0,1	45
L28	2,4	0,95	0,5	0,1	30
L29	2,6	1	0,7	0,1	75
L30	2,6	1,05	0,6	0,1	75
L31	2,6	1,1	0,6	0,1	75
L32	2,6	1,15	0,7	0,1	75
L33	2,6	1,2	0,7	0,1	75
L34	2,6	1,25	0,6	0,1	75
L35	2,6	1,3	0,6	0,1	75

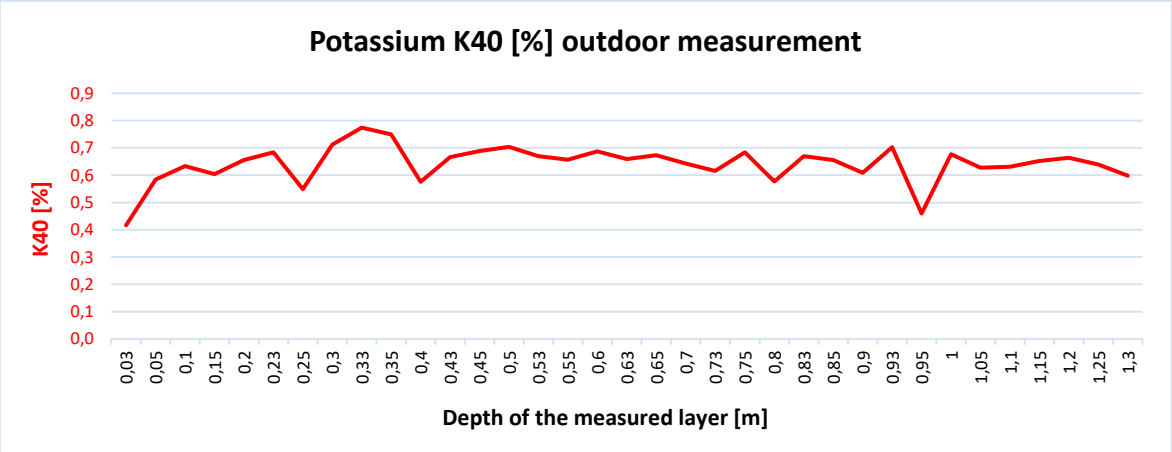

Figure 80. Potassium ^{40}K, outdoor measurement.

Uranium ^{238}U

Table 7. Uranium ^{238}U values after subtraction of the measured background.

Layers	U238 [ppm]	Depth of the measured layer [m]	Background subtraction from measured data U238 [ppm]	Standard Deviation SD [+/-]	Weight (kg)
L1	3,4	0,03	0,5	0,2	45
L2	3,6	0,05	0,8	0,2	75
L3	3,9	0,1	1,0	0,2	75
L4	3,9	0,15	1,0	0,2	75
L5	4,1	0,2	1,3	0,2	75
L6	4,0	0,23	1,2	0,2	45
L7	3,8	0,25	1,0	0,2	30
L8	4,2	0,3	1,3	0,2	75
L9	4,0	0,33	1,1	0,2	45
L10	3,9	0,35	1,1	0,2	30
L11	3,5	0,4	0,7	0,2	75
L12	3,6	0,43	0,8	0,2	45
L13	3,5	0,45	0,7	0,2	30
L14	3,6	0,5	0,7	0,2	75
L15	3,8	0,53	0,9	0,2	45
L16	3,5	0,55	0,6	0,2	30
L17	3,7	0,6	0,8	0,2	75
L18	3,5	0,63	0,7	0,2	45
L19	3,4	0,65	0,6	0,2	30
L20	3,4	0,7	0,6	0,2	75
L21	3,3	0,73	0,5	0,2	45
L22	3,6	0,75	0,7	0,2	30
L23	3,6	0,8	0,8	0,2	75
L24	3,5	0,83	0,6	0,2	45
L25	3,5	0,85	0,6	0,2	30

L26	3,4	0,9	0,5	0,2	75
L27	3,6	0,93	0,7	0,2	45
L28	3,2	0,95	0,4	0,2	30
L29	4,0	1	1,2	0,2	75
L30	3,4	1,05	0,6	0,2	75
L31	3,3	1,1	0,5	0,2	75
L32	3,5	1,15	0,7	0,2	75
L33	3,5	1,2	0,7	0,2	75
L34	3,4	1,25	0,6	0,2	75
L35	3,6	1,3	0,8	0,2	75

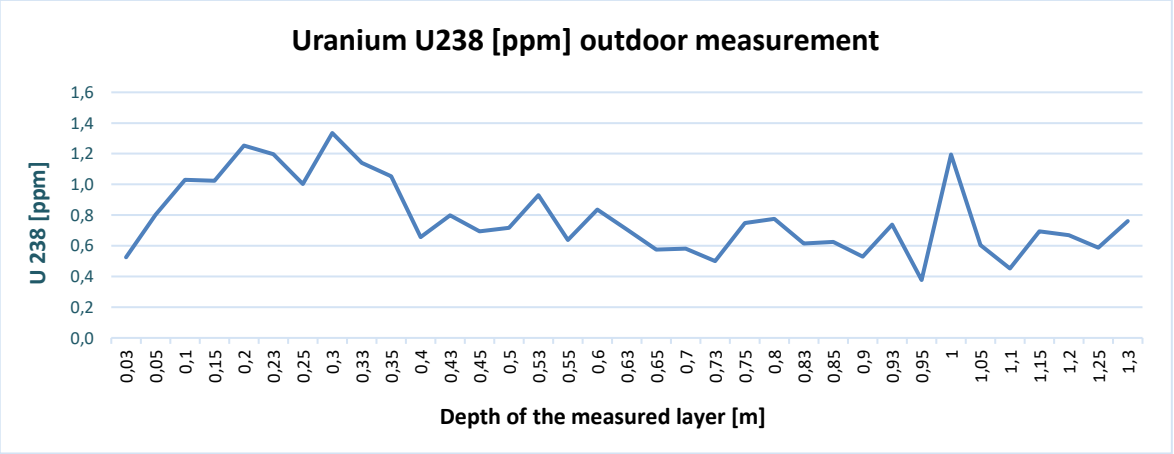

Figure 81. Uranium ^{238}U, outdoor measurements.

Thorium ^{232}Th

Table 8. Thorium ^{232}Th values after subtracting the measured background.

Layers	Th232 [ppm]	Depth of the measured layer [m]	Background subtraction from measured data Th232 [ppm]	Standard Deviation SD [+/-]	Weight (kg)
L1	12,0	0,03	2,3	0,3	45
L2	13,2	0,05	3,6	0,3	75
L3	13,6	0,1	4,0	0,3	75
L4	13,6	0,15	3,9	0,3	75
L5	14,1	0,2	4,4	0,3	75
L6	14,1	0,23	4,4	0,3	45
L7	13,7	0,25	4,1	0,3	30
L8	14,3	0,3	4,6	0,3	75
L9	14,0	0,33	4,4	0,3	45
L10	14,5	0,35	4,8	0,3	30
L11	13,7	0,4	4,0	0,3	75
L12	13,6	0,43	3,9	0,3	45
L13	14,2	0,45	4,5	0,3	30

L14	14,4	0,5	4,7	0,3	75
L15	13,9	0,53	4,2	0,3	45
L16	13,6	0,55	3,9	0,3	30
L17	13,7	0,6	4,1	0,3	75
L18	13,8	0,63	4,1	0,3	45
L19	13,8	0,65	4,1	0,3	30
L20	13,6	0,7	3,9	0,3	75
L21	13,3	0,73	3,7	0,3	45
L22	13,7	0,75	4,0	0,3	30
L23	13,3	0,8	3,6	0,3	75
L24	13,2	0,83	3,5	0,3	45
L25	13,0	0,85	3,3	0,3	30
L26	13,3	0,9	3,6	0,3	75
L27	13,4	0,93	3,8	0,3	45
L28	12,2	0,95	2,5	0,3	30
L29	13,4	1	3,8	0,3	75
L30	13,4	1,05	3,8	0,3	75
L31	13,2	1,1	3,5	0,3	75
L32	12,9	1,15	3,3	0,3	75
L33	13,3	1,2	3,7	0,3	75
L34	13,2	1,25	3,5	0,3	75
L35	12,7	1,3	3,0	0,3	75

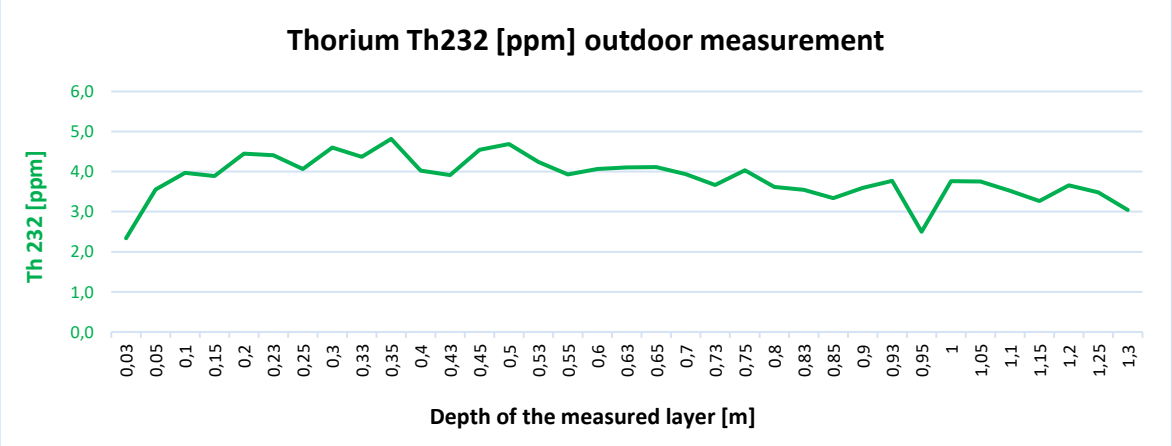

Figure 82. Thorium ^{232}Th, outdoor measurements.

3.4.7 Results of Measurements of Cesium ^{137}Cs Values

In the outdoor measurement, cesium ^{137}Cs was measured down to a depth of 23 cm. This is a vertical migration of cesium in undisturbed soil layers.

The highest measured values of anthropogenic radionuclides from the geological micro-probe:

Cesium ^{137}Cs – (1.1 ± 0.2) kBq/m^2, layer 2, 0.05 m depth.

Cesium 137 ^{137}Cs

Table 9. Cesium ^{137}Cs values after subtraction of the measured background.

Layers	Cs137 [kBq/m2]	Cs137 [Bq/m2]	Depth of the measured layer [m]	Background subtraction from measured data [kBq/m2]	Standard Deviation SD [+/-]	Weight (kg)
L1	1,3	1340	0,03	0,9	0,2	45
L2	1,6	1572	0,05	1,1	0,2	75
L3	1,4	1419	0,1	1,0	0,2	75
L4	1,0	984	0,15	0,5	0,2	75
L5	0,7	681	0,2	0,2	0,2	75
L6	0,5	518	0,23	0,1	0,2	45
L7	0,3	335	0,25	0,0	0,2	30
L8	0,3	271	0,3	0,0	0,2	75
L9	0,3	254	0,33	0,0	0,2	45
L10	0,2	155	0,35	0,0	0,2	30
L11	0,3	252	0,4	0,0	0,2	75
L12	0,2	244	0,43	0,0	0,2	45
L13	0,3	274	0,45	0,0	0,2	30
L14	0,3	267	0,5	0,0	0,2	75
L15	0,3	287	0,53	0,0	0,2	45
L16	0,3	253	0,55	0,0	0,2	30
L17	0,2	221	0,6	0,0	0,2	75
L18	0,2	204	0,63	0,0	0,2	45
L19	0,2	236	0,65	0,0	0,2	30
L20	0,2	170	0,7	0,0	0,2	75
L21	0,3	269	0,73	0,0	0,2	45
L22	0,2	164	0,75	0,0	0,2	30
L23	0,2	190	0,8	0,0	0,2	75
L24	0,2	186	0,83	0,0	0,2	45
L25	0,2	200	0,85	0,0	0,2	30
L26	0,2	194	0,9	0,0	0,2	75
L27	0,2	208	0,93	0,0	0,2	45
L28	0,2	178	0,95	0,0	0,2	30
L29	0,2	208	1	0,0	0,2	75
L30	0,2	151	1,05	0,0	0,2	75
L31	0,0	0	1,1	0,0	0,2	75
L32	0,2	195	1,15	0,0	0,2	75
L33	0,2	246	1,2	0,0	0,2	75
L34	0,2	190	1,25	0,0	0,2	75
L35	0,3	294	1,3	0,0	0,2	75

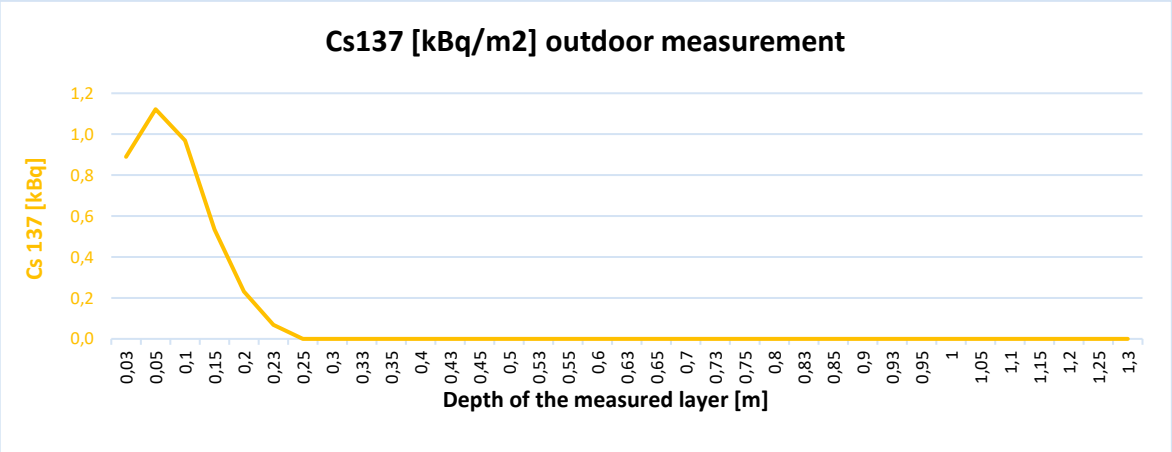

Figure 83. Cesium ^{137}Cs, outdoor measurement.

3.5 Measurement of Natural and Artificial Ionizing Radiation Samples from an Excavation Under Laboratory Conditions

The laboratory measurements were performed at the Faculty of Applied Informatics of UTB in the Laboratory of Forensic Sciences. The measurements were carried out from 6 September to 9 September 2023.

Figure 84. Laboratory measurement at the Faculty of Applied Informatics, UTB in the forensic science laboratory.

For the laboratory measurements, the weight for each layer was determined to be 6 kg. Each layer was weighed and placed in a plastic bag which was labelled with the layer number. The total weight of the measured samples transferred to the laboratory was 210 kg.

Figure 85. Weighing the layers.

Laboratory measurements were performed in Area_300E mode with a duration of 300 seconds for five repetitions.

Figure 86. Measurement of individual layers in the lead box.

3.5.1 Laboratory Background Measurement Results

Average background values in the lead box:

- Potassium ^{40}K – (0.2 ± 0.1) %
- Uranium ^{238}U – (0.2 ± 0.1) ppm
- Thorium ^{232}Th – (0.7 ± 0.1) ppm
- Cesium ^{137}Cs – (0.1 ± 0.1) kBq/m^2

3.5.2 Measurement Results of Individual Layers During Laboratory Measurement

Highest measured laboratory values of primordial radionuclides from the geological microprobe:

- Potassium ^{40}K– (1.0 ± 0.1) %, layer 18, depth 0.9 m.

- Uranium ^{238}U – (1.2 ± 0.1) ppm, layer 7, depth 0.25 m.
- Thorium ^{232}Th – (3.8 ± 0.2) ppm, layer 22, depth 0.75 m.

Potassium ^{40}K

Table 10. Potassium ^{40}K values after subtracting the measured background.

Layers	K40 [%]	Depth of the measured layer [m]	Background subtraction from measured data K40 [%]	Standard Deviation SD [+/-]	Weight (kg)
L1	0,7	0,03	0,6	0,1	6
L2	0,8	0,05	0,7	0,1	6
L3	0,8	0,1	0,7	0,1	6
L4	0,9	0,15	0,7	0,1	6
L5	0,8	0,2	0,7	0,1	6
L6	0,9	0,23	0,8	0,1	6
L7	0,9	0,25	0,8	0,1	6
L8	0,9	0,3	0,7	0,1	6
L9	0,9	0,33	0,8	0,1	6
L10	0,9	0,35	0,8	0,1	6
L11	0,9	0,4	0,8	0,1	6
L12	0,9	0,43	0,7	0,1	6
L13	0,9	0,45	0,8	0,1	6
L14	0,8	0,5	0,7	0,1	6
L15	0,9	0,53	0,8	0,1	6
L16	0,9	0,55	0,7	0,1	6
L17	1,0	0,6	0,8	0,1	6
L18	1,0	0,63	0,9	0,1	6
L19	0,9	0,65	0,7	0,1	6
L20	1,0	0,7	0,8	0,1	6
L21	1,0	0,73	0,8	0,1	6
L22	1,1	0,75	0,9	0,1	6
L23	1,0	0,8	0,9	0,1	6
L24	1,0	0,83	0,8	0,1	6
L25	1,0	0,85	0,9	0,1	6
L26	1,1	0,9	1,0	0,1	6
L27	1,0	0,93	0,8	0,1	6
L28	0,9	0,95	0,8	0,1	6
L29	1,0	1	0,8	0,1	6
L30	1,1	1,05	0,9	0,1	6
L31	1,1	1,1	0,9	0,1	6
L32	1,1	1,15	0,9	0,1	6
L33	1,1	1,2	0,9	0,1	6
L34	0,9	1,25	0,8	0,1	6
L35	1,0	1,3	0,8	0,1	6

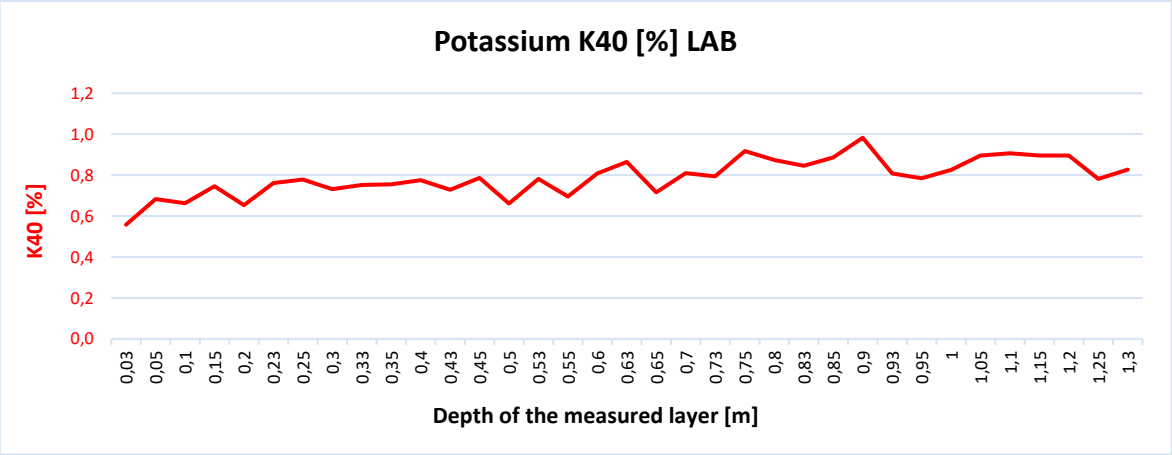

Figure 87. Potassium ^{40}K, laboratory measurement.

Uranium ^{238}U

Table 11. Uranium ^{238}U values after subtracting the measured background.

Layers	U238 [ppm]	Depth of the measured layer [m]	Background subtraction from measured data U238 [ppm]	Standard Deviation SD [+/-]	Weight (kg)
L1	0,9	0,03	0,7	0,1	6
L2	1,2	0,05	0,9	0,1	6
L3	1,2	0,1	1,0	0,1	6
L4	1,4	0,15	1,2	0,1	6
L5	1,1	0,2	0,9	0,1	6
L6	1,3	0,23	1,1	0,1	6
L7	1,4	0,25	1,2	0,1	6
L8	1,4	0,3	1,2	0,1	6
L9	1,3	0,33	1,1	0,1	6
L10	1,1	0,35	0,9	0,1	6
L11	1,1	0,4	0,9	0,1	6
L12	1,1	0,43	0,9	0,1	6
L13	1,1	0,45	0,9	0,1	6
L14	1,0	0,5	0,8	0,1	6
L15	1,2	0,53	1,0	0,1	6
L16	1,0	0,55	0,8	0,1	6
L17	1,1	0,6	0,9	0,1	6
L18	1,1	0,63	0,9	0,1	6
L19	0,9	0,65	0,7	0,1	6
L20	1,1	0,7	0,9	0,1	6
L21	1,0	0,73	0,8	0,1	6
L22	1,1	0,75	0,9	0,1	6
L23	1,2	0,8	1,0	0,1	6

L24	1,1	0,83	0,9	0,1	6
L25	1,1	0,85	0,9	0,1	6
L26	1,3	0,9	1,1	0,1	6
L27	1,0	0,93	0,8	0,1	6
L28	1,1	0,95	0,9	0,1	6
L29	1,1	1	0,9	0,1	6
L30	1,2	1,05	0,9	0,1	6
L31	1,1	1,1	0,9	0,1	6
L32	1,1	1,15	0,9	0,1	6
L33	1,2	1,2	1,0	0,1	6
L34	1,0	1,25	0,8	0,1	6
L35	1,1	1,3	0,9	0,1	6

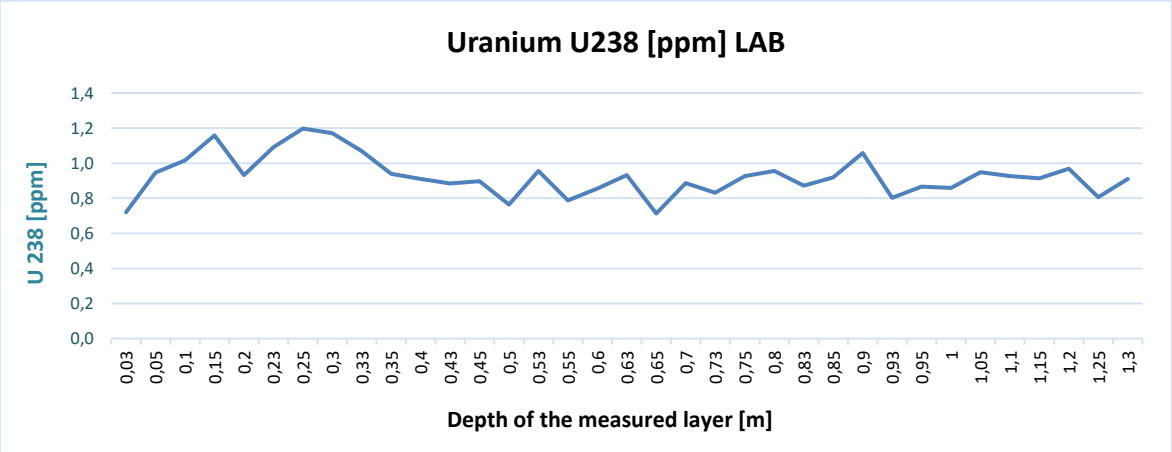

Figure 88. Uranium ^{238}U, laboratory measurements.

Thorium ^{232}Th

Table 12. Thorium ^{232}Th values after subtracting the measured background.

Layers	Th232 [ppm]	Depth of the meas-ured layer [m]	Background subtraction from measured data Th232 [ppm]	Standard Deviation SD [+/-]	Weight (kg)
L1	3,2	0,03	2,6	0,2	6
L2	3,5	0,05	2,9	0,2	6
L3	3,4	0,1	2,7	0,2	6
L4	3,8	0,15	3,2	0,2	6
L5	3,8	0,2	3,1	0,2	6
L6	4,2	0,23	3,5	0,2	6
L7	4,2	0,25	3,5	0,2	6
L8	4,0	0,3	3,4	0,2	6
L9	3,7	0,33	3,0	0,2	6
L10	3,9	0,35	3,2	0,2	6
L11	4,2	0,4	3,5	0,2	6

L12	3,8	0,43	3,1	0,2	6
L13	3,9	0,45	3,2	0,2	6
L14	3,5	0,5	2,8	0,2	6
L15	4,0	0,53	3,3	0,2	6
L16	3,6	0,55	2,9	0,2	6
L17	4,0	0,6	3,3	0,2	6
L18	4,3	0,63	3,6	0,2	6
L19	3,7	0,65	3,0	0,2	6
L20	4,1	0,7	3,4	0,2	6
L21	4,0	0,73	3,3	0,2	6
L22	4,5	0,75	3,8	0,2	6
L23	4,2	0,8	3,5	0,2	6
L24	3,9	0,83	3,2	0,2	6
L25	4,2	0,85	3,5	0,2	6
L26	4,5	0,9	3,8	0,2	6
L27	3,8	0,93	3,1	0,2	6
L28	3,8	0,95	3,1	0,2	6
L29	4,0	1	3,4	0,2	6
L30	4,1	1,05	3,4	0,2	6
L31	4,3	1,1	3,7	0,2	6
L32	4,2	1,15	3,5	0,2	6
L33	3,9	1,2	3,2	0,2	6
L34	3,6	1,25	2,9	0,2	6
L35	3,7	1,3	3,0	0,2	6

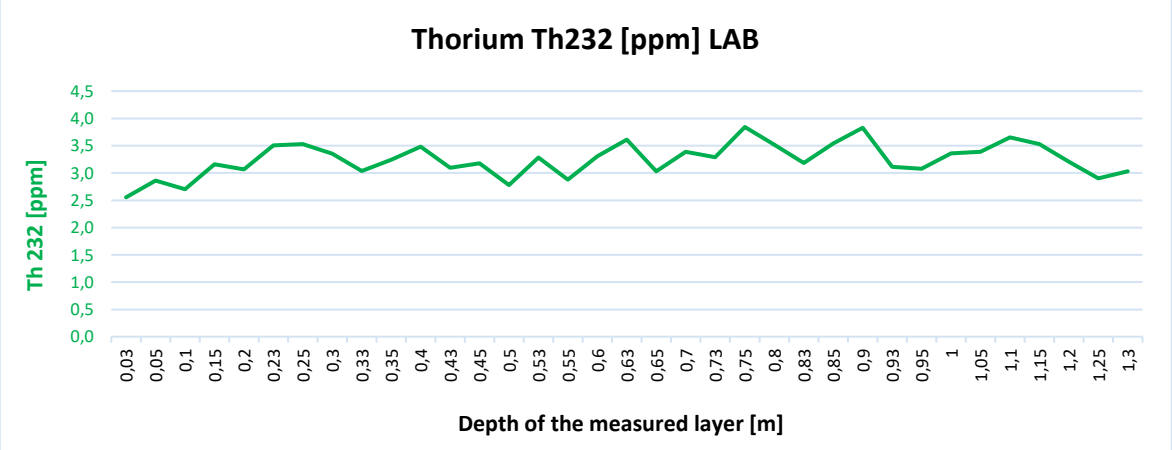

Figure 89. Thorium ^{232}Th, laboratory measurement.

Cesium ^{137}Cs

Highest measured laboratory values of anthropogenic radionuclides from the geological microprobe:

- Cesium ^{137}Cs – (0.4 ± 0.1) kBq/m^2, layer 2, depth 5 cm.

The highest measured cesium value is at a depth of 5 cm and represents 33% of the total. In 1 kg of soil, 0.07 kBq/m^2 or 0.001 m^3 contains 0.07 kBq/m^2.

Table 13. Cesium ^{137}Cs values after subtraction of the measured background.

Layers	Cs137 [kBq/m2]	Cs137 [Bq/m2]	Depth of the measured layer [m]	Background subtraction from measured data [kBq/m2]	Standard Deviation SD [+/-]	Weight (kg)
L1	0,4	381	0,03	0,3	0,1	6
L2	0,5	501	0,05	0,4	0,1	6
L3	0,4	395	0,1	0,3	0,1	6
L4	0,2	243	0,15	0,1	0,1	6
L5	0,2	187	0,2	0,1	0,1	6
L6	0,0	0	0,23	0,0	0,0	6
L7	0,0	0	0,25	0,0	0,0	6
L8	0,0	0	0,3	0,0	0,0	6
L9	0,0	0	0,33	0,0	0,0	6
L10	0,0	0	0,35	0,0	0,0	6
L11	0,0	0	0,4	0,0	0,0	6
L12	0,0	0	0,43	0,0	0,0	6
L13	0,0	0	0,45	0,0	0,0	6
L14	0,0	0	0,5	0,0	0,0	6
L15	0,0	0	0,53	0,0	0,0	6
L16	0,0	0	0,55	0,0	0,0	6
L17	0,0	0	0,6	0,0	0,0	6
L18	0,0	0	0,63	0,0	0,0	6
L19	0,0	0	0,65	0,0	0,0	6
L20	0,0	0	0,7	0,0	0,0	6
L21	0,0	0	0,73	0,0	0,0	6
L22	0,0	0	0,75	0,0	0,0	6
L23	0,0	0	0,8	0,0	0,0	6
L24	0,0	0	0,83	0,0	0,0	6
L25	0,0	0	0,85	0,0	0,0	6
L26	0,0	0	0,9	0,0	0,0	6
L27	0,0	0	0,93	0,0	0,0	6
L28	0,0	0	0,95	0,0	0,0	6
L29	0,0	0	1	0,0	0,0	6
L30	0,0	0	1,05	0,0	0,0	6
L31	0,0	0	1,1	0,0	0,0	6
L32	0,0	0	1,15	0,0	0,0	6
L33	0,0	0	1,2	0,0	0,0	6
L34	0,0	0	1,25	0,0	0,0	6
L35	0,0	0	1,3	0,0	0,0	6

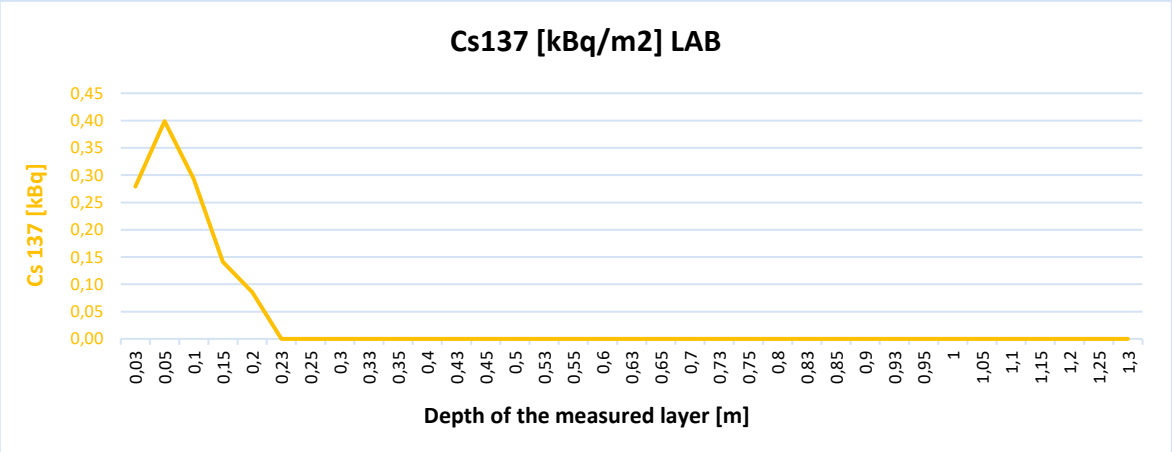

Figure 90. Cesium ^{137}Cs, laboratory measurement.

3.5.3 Laboratory Measurements of Findings from Individual Layers

The grey color in the table indicates the layers where shards, fist wedges, bone fragments and metal objects were found.

Potassium ^{40}K

Table 14. Potassium ^{40}K values after subtracting the measured background.

Layers	K40 [%]	Depth of the measured layer [m]	Background subtraction from measured data K40 [%]	Standard Deviation SD [+/-]	Weight fragments in layers (kg)
L1	0,0	0,03	0,000	0,0	0,00
L2	0,0	0,05	0,000	0,0	0,00
L3	0,0	0,1	0,000	0,0	0,00
L4	0,2	0,15	0,011	0,1	0,07
L5	0,2	0,2	0,017	0,1	0,04
L6	0,0	0,23	0,000	0,0	0,00
L7	0,0	0,25	0,000	0,0	0,00
L8	0,0	0,3	0,000	0,0	0,00
L9	0,2	0,33	0,001	0,1	0,04
L10	0,2	0,35	0,015	0,1	0,03
L11	0,2	0,4	0,002	0,1	0,03
L12	0,2	0,43	0,004	0,1	0,02
L13	0,2	0,45	0,014	0,1	0,05
L14	0,2	0,5	0,010	0,1	0,06
L15	0,2	0,53	0,023	0,1	0,11
L16	0,2	0,55	0,026	0,1	0,07
L17	0,2	0,6	0,003	0,1	0,04
L18	0,2	0,63	0,043	0,1	0,27
L19	0,2	0,65	0,009	0,1	0,06

L20	0,2	0,7	0,018	0,1	0,29
L21	0,2	0,73	0,007	0,1	0,05
L22	0,2	0,75	0,047	0,1	0,18
L23	0,2	0,8	0,018	0,1	0,43
L24	0,2	0,83	0,076	0,1	0,76
L25	0,2	0,85	0,025	0,1	0,30
L26	0,2	0,9	0,005	0,1	0,07
L27	0,2	0,93	0,009	0,1	0,05
L28	0,2	0,95	0,016	0,1	0,51
L29	0,2	1	0,049	0,1	0,21
L30	0,2	1,05	0,018	0,1	0,04
L31	0,2	1,1	0,000	0,1	0,01
L32	0,2	1,15	0,019	0,1	0,04
L33	0,2	1,2	0,011	0,1	0,03
L34	0,2	1,25	0,018	0,1	0,06
L35	0,0	1,3	0,000	0,0	0,00

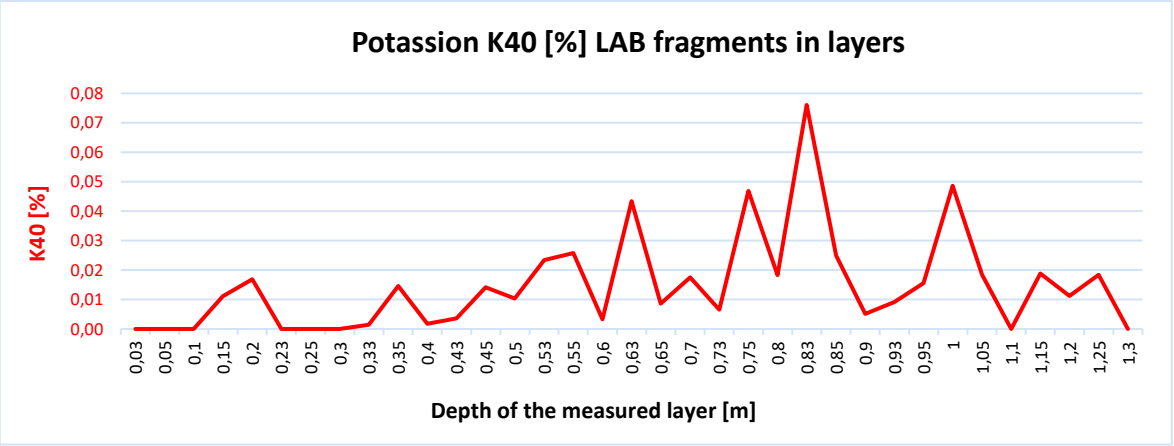

Figure 91. Potassium ^{40}K, laboratory measurement.

Uranium ^{238}U

Table 15. Uranium ^{238}U values after subtracting the measured background.

Layers	U238 [ppm]	Depth of the measured layer [m]	Background subtraction from measured data U238 [ppm]	Standard Deviation SD [+/-]	Weight fragments in layers (kg)
L1	0,0	0,03	0,000	0,0	0,00
L2	0,0	0,05	0,000	0,0	0,00
L3	0,0	0,1	0,000	0,0	0,00
L4	0,2	0,15	0,000	0,1	0,07
L5	0,1	0,2	0,000	0,1	0,04
L6	0,0	0,23	0,000	0,0	0,00
L7	0,0	0,25	0,000	0,0	0,00

L8	0,0	0,3	0,000	0,0	0,00
L9	0,2	0,33	0,004	0,1	0,04
L10	0,2	0,35	0,000	0,1	0,03
L11	0,2	0,4	0,000	0,1	0,03
L12	0,2	0,43	0,000	0,1	0,02
L13	0,2	0,45	0,000	0,1	0,05
L14	0,2	0,5	0,000	0,1	0,06
L15	0,2	0,53	0,000	0,1	0,11
L16	0,2	0,55	0,000	0,1	0,07
L17	0,2	0,6	0,000	0,1	0,04
L18	0,2	0,63	0,000	0,1	0,27
L19	0,2	0,65	0,016	0,1	0,06
L20	0,3	0,7	0,047	0,1	0,29
L21	0,2	0,73	0,000	0,1	0,05
L22	0,3	0,75	0,081	0,1	0,18
L23	0,2	0,8	0,033	0,1	0,43
L24	0,3	0,83	0,047	0,1	0,76
L25	0,2	0,85	0,000	0,1	0,30
L26	0,2	0,9	0,000	0,1	0,07
L27	0,2	0,93	0,000	0,1	0,05
L28	0,2	0,95	0,000	0,1	0,51
L29	0,2	1	0,000	0,1	0,21
L30	0,2	1,05	0,000	0,1	0,04
L31	0,1	1,1	0,000	0,1	0,01
L32	0,2	1,15	0,000	0,1	0,04
L33	0,2	1,2	0,000	0,1	0,03
L34	0,2	1,25	0,000	0,1	0,06
L35	0,0	1,3	0,000	0,0	0,00

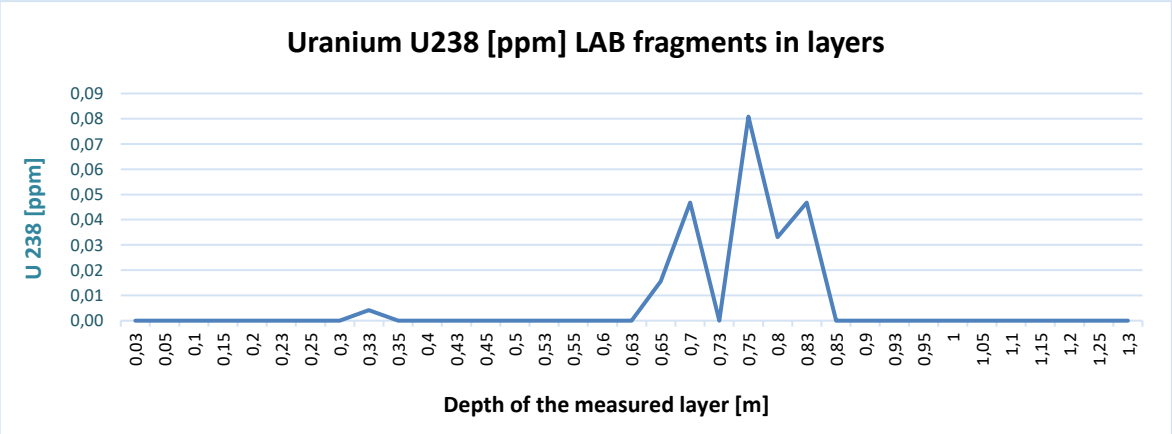

Figure 92. Uranium ^{238}U, laboratory measurements.

Thorium ^{232}Th

Table 16. Thorium ^{232}Th values after subtracting the measured background.

Layers	Th232 [ppm]	Depth of the measured layer [m]	Background subtraction from measured data Th232 [ppm]	Standard Deviation SD [+/-]	Weight fragments in layers (kg)
L1	0,0	0,03	0,000	0,0	0,00
L2	0,0	0,05	0,000	0,0	0,00
L3	0,0	0,1	0,000	0,0	0,00
L4	0,9	0,15	0,167	0,1	0,07
L5	0,8	0,2	0,124	0,1	0,04
L6	0,0	0,23	0,000	0,0	0,00
L7	0,0	0,25	0,000	0,0	0,00
L8	0,0	0,3	0,000	0,0	0,00
L9	0,8	0,33	0,079	0,1	0,04
L10	0,7	0,35	0,000	0,1	0,03
L11	0,8	0,4	0,145	0,1	0,03
L12	0,7	0,43	0,038	0,1	0,02
L13	0,8	0,45	0,086	0,1	0,05
L14	0,9	0,5	0,164	0,1	0,06
L15	0,9	0,53	0,175	0,1	0,11
L16	0,7	0,55	0,038	0,1	0,07
L17	0,8	0,6	0,098	0,1	0,04
L18	0,8	0,63	0,118	0,1	0,27
L19	0,6	0,65	0,000	0,1	0,06
L20	0,8	0,7	0,147	0,1	0,29
L21	0,8	0,73	0,097	0,1	0,05
L22	0,8	0,75	0,154	0,1	0,18
L23	1,1	0,8	0,370	0,1	0,43
L24	0,9	0,83	0,209	0,1	0,76
L25	0,9	0,85	0,194	0,1	0,30
L26	0,8	0,9	0,149	0,1	0,07
L27	0,8	0,93	0,099	0,1	0,05
L28	0,8	0,95	0,127	0,1	0,51
L29	0,9	1	0,234	0,1	0,21
L30	0,8	1,05	0,065	0,1	0,04
L31	0,7	1,1	0,060	0,1	0,01
L32	0,7	1,15	0,045	0,1	0,04
L33	0,7	1,2	0,000	0,1	0,03
L34	0,7	1,25	0,045	0,1	0,06
L35	0,0	1,3	0,000	0,0	0,00

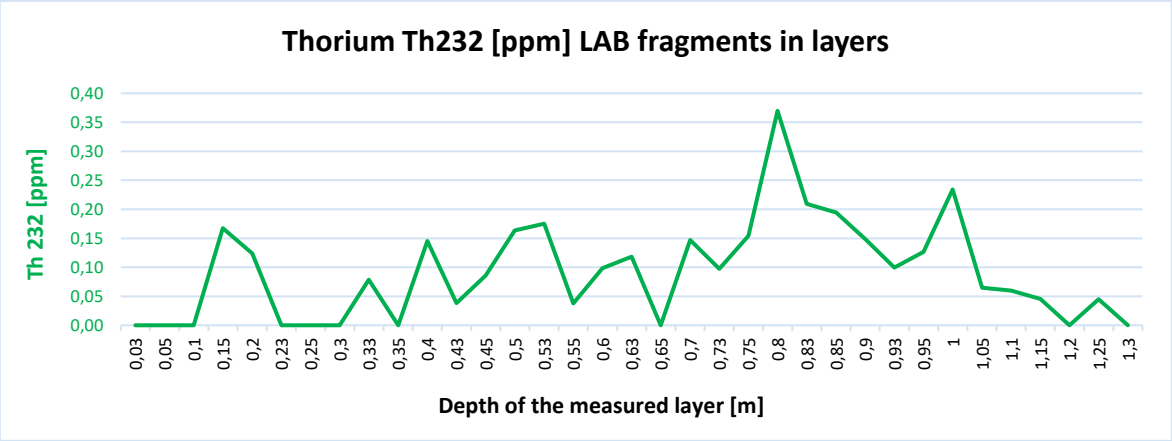

Figure 93. Thorium ^{232}Th, laboratory measurement.

Cesium ^{137}Cs

During the measurement of the finds, I measured a cesium ^{137}Cs value (0.0008 kBq/m^2) in layer 25 (0.85 m depth). The measurement of cesium ^{137}Cs at this depth may be related to the tree root system that grew across the layers of the excavation [90]. Potassium plays a major role in these processes [99].

Table 17. Cesium ^{137}Cs values after subtraction of the measured background.

Layers	Cs137 [kBq/m2]	Depth of the measured layer [m]	Background subtraction from measured data [kBq/m2]	Standard Deviation SD [+/-]
L1	0,000	0,03	0,000	0,0
L2	0,000	0,05	0,000	0,0
L3	0,000	0,1	0,000	0,0
L4	0,053	0,15	0,000	0,0
L5	0,070	0,2	0,000	0,0
L6	0,000	0,23	0,000	0,0
L7	0,000	0,25	0,000	0,0
L8	0,000	0,3	0,000	0,0
L9	0,051	0,33	0,000	0,0
L10	0,000	0,35	0,000	0,0
L11	0,000	0,4	0,000	0,0
L12	0,000	0,43	0,000	0,0
L13	0,033	0,45	0,000	0,0
L14	0,052	0,5	0,000	0,0
L15	0,061	0,53	0,000	0,0
L16	0,067	0,55	0,000	0,0
L17	0,058	0,6	0,000	0,0
L18	0,066	0,63	0,000	0,0
L19	0,043	0,65	0,000	0,0
L20	0,037	0,7	0,000	0,0
L21	0,047	0,73	0,000	0,0

L22	0,064	0,75	0,000	0,0
L23	0,000	0,8	0,000	0,0
L24	0,077	0,83	0,000	0,0
L25	0,103	0,85	0,0008	0,1
L26	0,068	0,9	0,000	0,0
L27	0,069	0,93	0,000	0,0
L28	0,060	0,95	0,000	0,0
L29	0,056	1	0,000	0,0
L30	0,043	1,05	0,000	0,0
L31	0,068	1,1	0,000	0,0
L32	0,106	1,15	0,000	0,0
L33	0,000	1,2	0,000	0,0
L34	0,052	1,25	0,000	0,0
L35	0,000	1,3	0,000	0,0

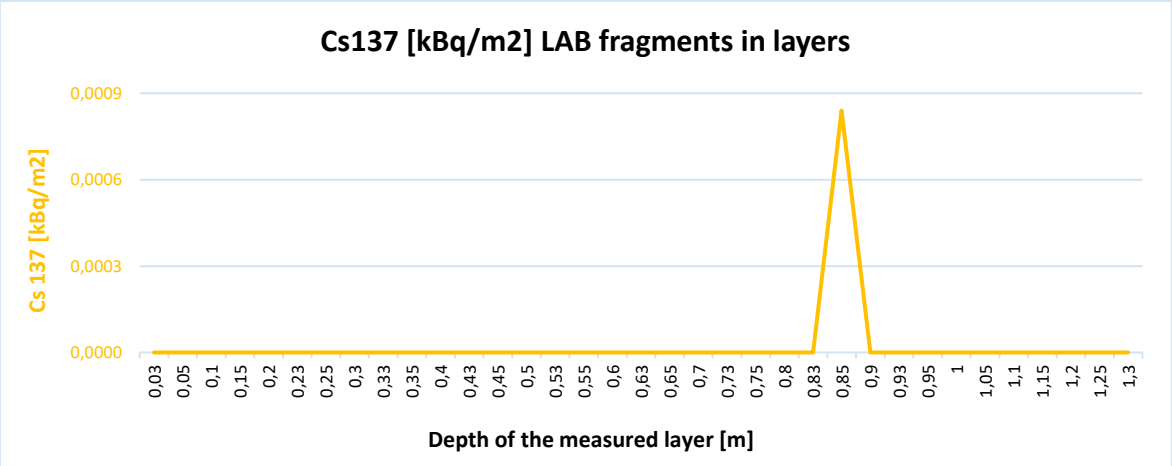

Figure 94. Cesium ^{137}Cs, laboratory measurement.

3.6 Comparison of Outdoor and Laboratory Measurements of Individual layers

When comparing the outdoor and laboratory measurements, a systematic error in the measured values became apparent.

I used the following formula to calculate the measurement error:

Measured value: MV

Actual value: AV

Absolute error: Δ = MV - AV

Percentage error:

$$\delta = \frac{\Delta}{AV} \times 100 \tag{1.6}$$

Percentage error between outdoor and laboratory measurements:

- Potassium ^{40}K – 19 %
- Uranium ^{238}U – 16 %
- Thorium ^{232}Th – 19 %

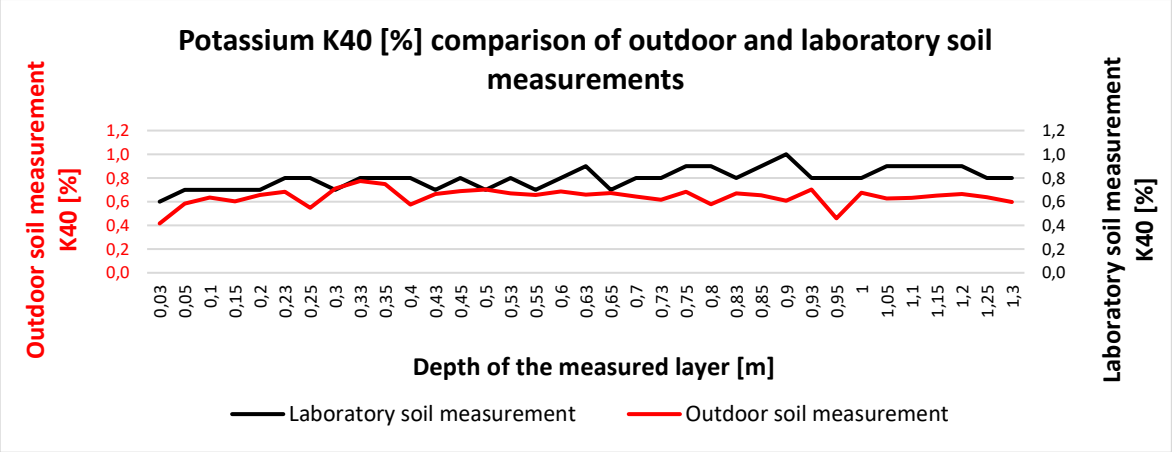

Figure 95. Comparison of measured potassium ^{40}K values for outdoor and laboratory measurements.

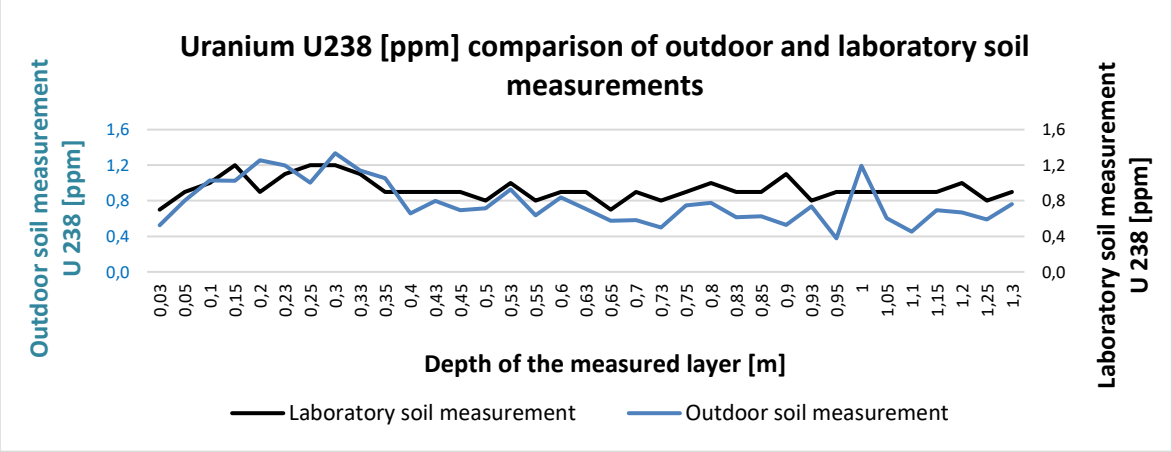

Figure 96. Comparison of measured uranium ^{238}U values for outdoor and laboratory measurements.

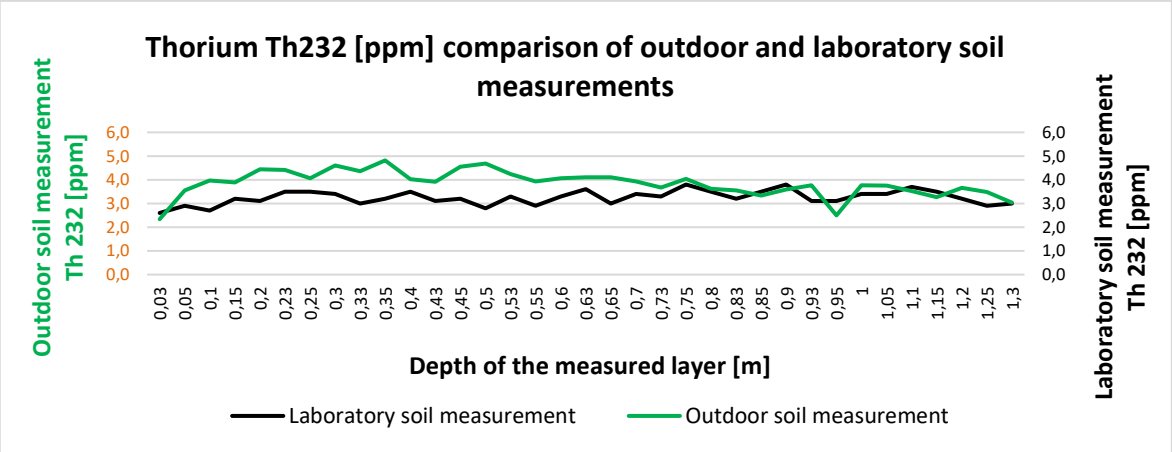

Figure 97. Comparison of measured thorium ^{232}Th values for outdoor and laboratory measurements.

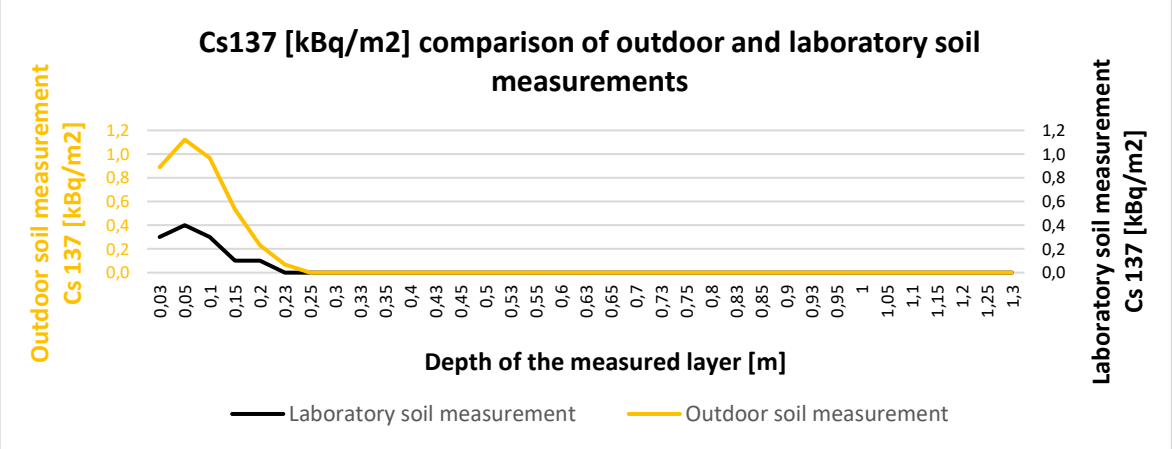

Figure 98. Comparison of measured cesium ^{137}Cs values for outdoor and laboratory measurements.

3.7 Creating a Timeline from Radiocarbon Dating Results

When creating a timeline for the bone finds from each layer, it is necessary to consider the level of uncertainty. This measurement uncertainty applies to the qualitative assessment of bone collagen concentration. The bone samples ranged in quality from 4.5 to 5.5. In this case, the dating result is treated with caution.

To assign the dating of the layers containing cesium ^{137}Cs, the radiocarbon dating of the bone findings was based on the following depths: 0.53 m (1904 ± 16) BP; 0.63 m (1749 ± 16) BP; 0.73 m (1753 ± 18) BP; 0.75 m (1684 ± 16) BP and 0.8 m (1586 ± 16) BP. A linear regression mathematical model was used to determine soil growth. The increase in soil was

determined to be 9×10^{-4}. It follows that 0.8 mm of soil in a given location is formed in approximately 1 year.

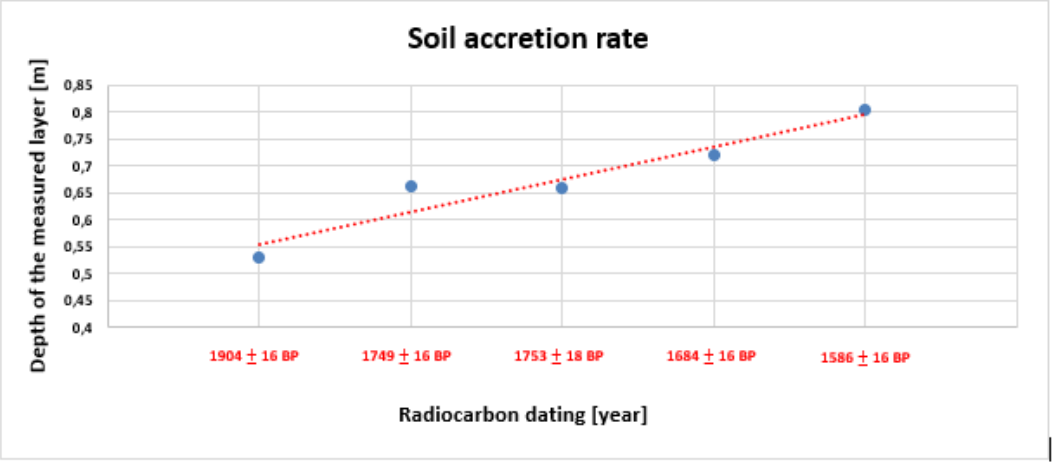

Figure 99. Soil accretion at a given location for a time period, 0.8 mm in 1 year.

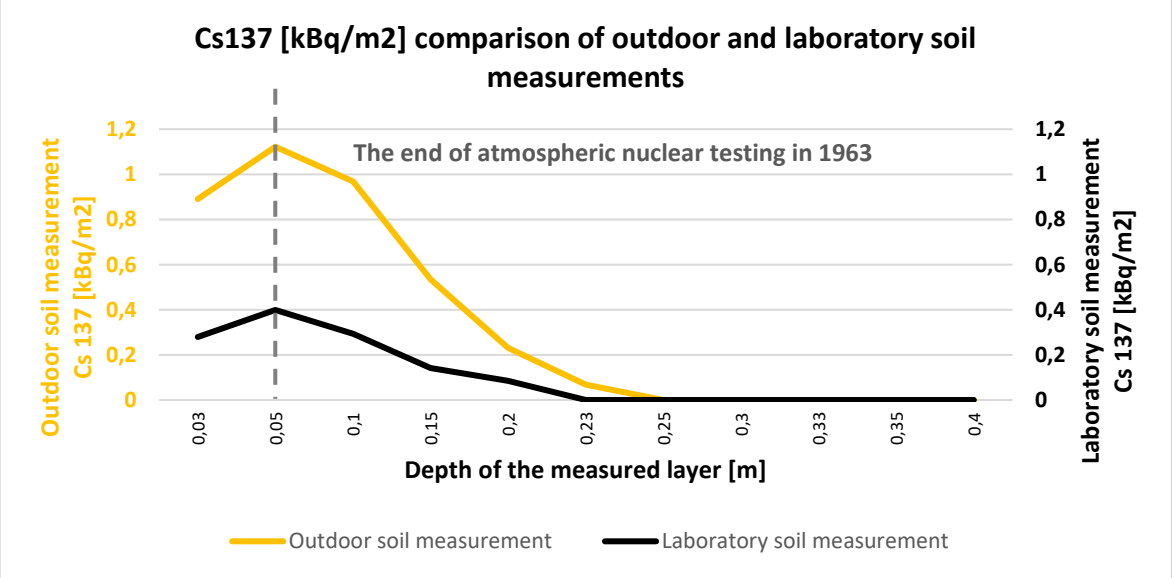

Figure 100. Comparison of measured cesium ^{137}Cs values for outdoor and laboratory measurements. Timeline assignment for dating individual layers with cesium ^{137}Cs occurrence.

Calculation of the decay rate of cesium ^{137}Cs:

T = half-life (cesium ^{137}Cs - half-life 30.17 years)

λ =? conversion constant, unit s^{-1}

$$\lambda = \frac{\ln 2}{T} \tag{1.7}$$

$$\lambda = \frac{\ln 2}{30.17} = 0.023\ s^{-1}$$

Cesium ^{137}Cs decays at a rate of $0.023\ s^{-1}$ per year.

Calculation of the decay time of cesium ^{137}Cs to 0.1% of its value:

T = half-life (cesium ^{137}Cs - half-life 30.17 years)

$N = 0{,}1\%N_0$, $N = 10^{-3}\ N_0$

$2^{10} = 1024 = 10^3$

t =? (decay time)

$$N = N_0(\frac{1}{2})^{\frac{t}{T}} \tag{1.8}$$

$$10^{-3}N_0 = N_0(\frac{1}{2})^{\frac{t}{T}}$$

$$10^{-3} = (\frac{1}{2})^{\frac{t}{T}}$$

$$10^3 = 2^{\frac{t}{T}}$$

$$2^{10} = 2^{\frac{t}{T}} \rightarrow \frac{t}{T} = 10 \rightarrow t = 10 \cdot T$$

$$t = 10 \cdot 30{,}17 = 301 \text{ years}$$

Cesium ^{137}Cs reaches 0.1% in 301 years.

The highest cesium value occurs at a depth of 0.05 cm with a time date of 1963 $\pm$ 16. The calculation of the half-life for the last atmospheric nuclear test relates to this year. **Based on the last atmospheric test in 1963 $\pm$ 16, the cesium contamination at the site would be 0.1% in 2263 $\pm$ 16.**

Another added value of radiocarbon dating was the assignment of an approximate timeline to primordial radionuclides from a historical perspective. This offers a further possible elaboration of the influence of human activities and natural processes on the radiation load of the landscape. Natural influences may include, for example, climate change and volcanic activity in the Northern Hemisphere in the past.

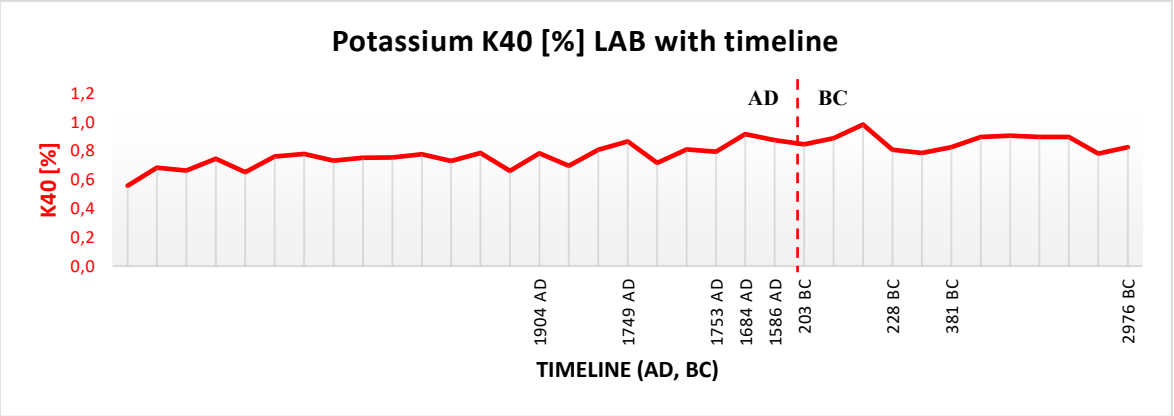

Figure 101. Values of laboratory measurement of potassium ^{40}K and approximate dating of bone findings in individual layers.

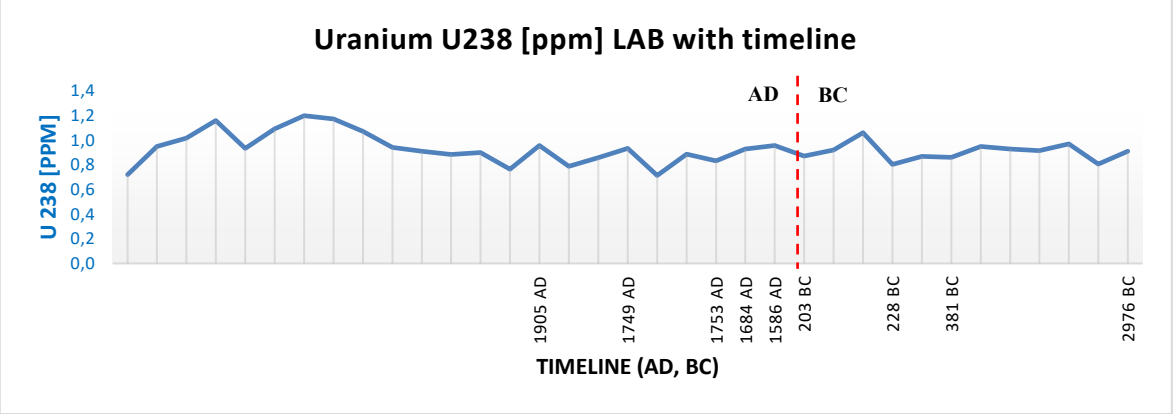

Figure 102. Values of laboratory measurement of uranium ^{238}U and approximate dating of bone finds in individual layers.

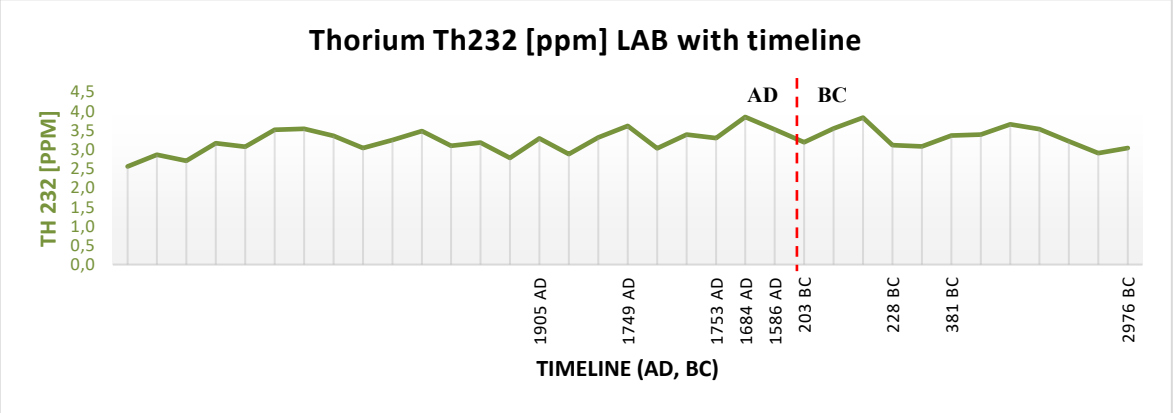

Figure 103. Laboratory measurement values of thorium ^{232}Th and approximate dating of bone finds in individual layers.

3.8 Evaluation of the obtained data

The work focused on the measurement of primordial and anthropogenic radionuclides in the area. During the measurements, special effort was put into recording the values as accurately as possible and following working procedures that were adopted from various scientific disciplines. Consultations with the building authority in Kojetin, archaeologists from the Historical Institute of the Museum of Homeland Science in Olomouc and field archaeologists from the Komenský Museum in Přerov were used in the work. Recommendations of geologists from the Museum of Southeast Moravia in Zlín were also applied. The analysis of the data led to the conclusion that the landscape around Popůvky is radiation-laden due to human activity. First of all, it is caused pollution by primordial radionuclides from coal burning and use of phosphate fertilizers. It is also the result of global impact of atmospheric nuclear weapons tests in the Northern Hemisphere, the consequences of which are still measurable today. In this case, it is the occurrence of cesium ^{137}Cs at the site. These tests are still adversely affecting the environment and human health today.

For a more comprehensive view of the radiation load of a given area and an accurate evaluation of the measured data, a larger surveyed perimeter would be required for surface measurements. A larger number of measurement points is also associated with a larger measurement area. The larger the number of points the more accurate the visualization. In the case of measuring layers in an excavation, it would be necessary to sample thinner layers by scraping, for example, at 5 cm intervals. In the case of cesium ^{137}Cs, an excavation depth of 0.3 m would be sufficient. In the case of studies of cesium ^{137}Cs migration, a greater depth may be required. It would also be of great benefit to carry out geological microprobes in different soil types.

During the work, a large amount of data processing was dealt with. This data was collected over a period of 6 months. For more detailed, accurate and longer lasting measurements, an information system would be required which would include an SQL database. This system should be able to import data from different measuring devices, but also to export data for example for map visualizations. The possibility of interfacing with other systems of different scientific disciplines such as geology, meteorology and pedology would be an advantage. Data processed and evaluated in this way could be used in potential crisis situations. These would include, for example, nuclear accidents, terrorist attacks on soft targets using dirty bombs or the possible use of nuclear weapons.

CONCLUSION

The data analysis concluded that the landscape around Popůvky near Kojetín is under radiation load due to human activities. These activities include coal burning, phosphate fertilization and nuclear experiments in the atmosphere. Laboratory measurements of the soil layers showed the highest contamination of the soil with cesium ^{137}Cs at a depth of 5 cm. Using radiocarbon dating, the rate of increase in the black soil profile at the Popůvky site near Kojetín was calculated to be 0.8 mm per year. Based on these data, a timeline corresponding to the atmospheric nuclear experiments of the 1960s was determined for a depth of 5 cm for the site. In the case of the Chernobyl accident, the measurements fell below the threshold values, indicating negligible impact of the accident on the site. In conclusion, it can be stated that the greatest burden on the landscape is caused by anthropogenic radionuclides. In particular, the contamination with cesium ^{137}Cs from nuclear experiments in the atmosphere, which will burden the landscape for approximately 240 years.

BIBLIOGRAPHY

[1] *Universe*. Online. Universe NASA. Available from: https://universe.nasa.gov/universe/basics/. [Accessed 2024-01-28].

[2] *Dark Matter May Be Older Than the Big Bang*. Online. SciTechDaily. 2019. Available from: https://scitechdaily.com/dark-matter-may-be-older-than-the-big-bang/. [Accessed 2024-01-28].

[3] *Může být temná hmota starší než Velký třesk?* Online. Česká astronomická společnost. 2019. Available from: https://www.astro.cz/clanky/vzdaleny-vesmir/muze-byt-temna-hmota-starsi-nez-velky-tresk.html?tag=kosmick%C3%A1%20inflace. [Accessed 2024-01-28].

[4] HAWKING, Stephen. *Černé díry a budoucnost vesmíru*. Kolumbus. Praha: Mladá fronta, 1995. ISBN 80-204-0515-1.

[5] *What's so special about the Higgs boson?* Online. CERN. 2024. Available from: https://home.cern/science/physics/higgs-boson/what. [Accessed 2024-01-28].

[6] *The birth of a Higgs boson*. Online. CERN. 2024. Available from: https://home.cern/news/news/physics/birth-higgs-boson. [Accessed 2024-01-28].

[7] *What are Hadrons?* Online. Japan Proton Accelerator Research Complex. Available from: https://j-parc.jp/c/en/facilities/nuclear-and-particle-physics/hadron.html. [Accessed 2024-01-27].

[8] HAWKING, Stephen. *Stručná historie času v obrazech*. Praha: Argo, 2002. ISBN 80-720-3422-7.

[9] *Cosmic Background Radiation*. Online. 8TH – GRADE SCIENCE. Available from: http://science8sc.weebly.com/cosmic-background-radiation.html. [Accessed 2024-01-24].

[10] PODZIMEK, František. *Radiologická fyzika*. 2. vydání. V Praze: České vysoké učení technické. ISBN 978-80-01-06900-4.

[11] PODZIMEK, František. *Radiologická fyzika*. V Praze: České vysoké učení technické, 2022. ISBN 978-80-01-06971-4.

[12] *Cosmic rays, explained*. Online. Uchicago. 2023. Available from: https://news.uchicago.edu/explainer/what-are-cosmic-rays. [Accessed 2024-01-27].

[13] *Supernovas & Supernova Remnants*. Online. CHANDRA X – RAY Observatory. Available from: https://chandra.harvard.edu/xray_sources/supernovas.html. [Accessed 2024-01-27].

[14] *Polar plots of the solar wind speed*. Online. ESA. 2024. Available from: https://sci.esa.int/web/ulysses/-/43461-polar-plots-of-the-solar-wind-speed. [Accessed 2024-01-30].

[15] *llustration showing Van Allen radiation belts*. Online. ESA. 2016. Available from: https://www.esa.int/ESA_Multimedia/Images/2016/06/Illustration_showing_Van_Allen_radiation_belts. [Accessed 2024-01-30].

[16] ONORATO, Giada; DI SCHIAVI, Elia a DI CUNTO, Ferdinando. Understanding the Effects of Deep Space Radiation on Nervous System: The Role of Genetically Tractable Experimental Models. Online. *Frontiers in Physics*. 2020, vol. 8. ISSN 2296-424X. Available from: https://doi.org/10.3389/fphy.2020.00362. [Accessed 2024-01-29].

[17] *What are Cosmic Rays?* Online. Let's Talk Science. 2019. Available from: https://letstalkscience.ca/educational-resources/backgrounders/what-are-cosmic-rays. [Accessed 2024-01-30].

[18] *Cosmic Rays*. Online. Antarctic Glaciers. 2023. Available from: https://www.antarcticglaciers.org/glacial-geology/dating-glacial-sediments-2/cosmogenic-nuclide-dating/cosmic-rays/. [Accessed 2024-01-30].

[19] *The Technical Details: Radioactive Decay*. Online. Global Monitoring Laboratory. Available from: https://gml.noaa.gov/ccgg/isotopes/decay.html. [Accessed 2024-02-01].

[20] *Primordial Radionuclides: Origin, Importance, and Health Impact*. Online. Nevada Technical Associates. 2023. Available from: https://www.ntanet.net/primordial-radionuclides-origin-importance-and-health-impact/. [Accessed 2024-02-01].

[21] *A temperate planet*. Online. RADIOACTIVITY. Available from: https://radioactivity.eu.com/in_daily_life/earth_heat. [Accessed 2024-02-05].

[22] *Geothermal Energy*. Online. National Geographic. Available from: https://education.nationalgeographic.org/resource/geothermal-energy/. [Accessed 2024-02-06].

[23] *Pan-European Thermal Atlas 4.3*. Online. Heatroadmap. 2018. Available from: https://heatroadmap.eu/peta4/. [Accessed 2024-02-06].

[24] *Atlas of Natural Radiation*. Online. Joint Research Centre. Available from: https://remap.jrc.ec.europa.eu/Atlas.aspx?layerID=9#. [Accessed 2024-02-05].

[25] CINELLI, G.; De CORT, M.; TOLLEFSEN, T.; ACHATZ, M.; AJTIĆ, J.; BALLABIO eds. Publications Office of the European Union, Luxembourg, 2019, ISBN 978-92-76-08258-3, JRC116795. [Accessed 2024-02-01].

[26] HÜBENER, Siegfried. Actinide Elements. Online. *Encyclopedia of Physical Science and Technology*. 2003, s. 211-236. ISBN 9780122274107. Available from: https://doi.org/10.1016/B0-12-227410-5/00011-9. [Accessed 2024-02-08].

[27] *Uranium Gamma Spectrometry*. Online. PhysicsOpenLab. 2016. Available from: https://physicsopenlab.org/2016/01/29/uranium-gamma-spectrometry/. [Accessed 2024-02-06].

[28] *Decay chain*. Online. Wikipedia. Available from: https://en.wikipedia.org/wiki/Decay_chain. [Accessed 2024-02-06].

[29] *Decay chain*. Online. Wikipedia. Available from: https://en.wikipedia.org/wiki/Decay_chain. [Accessed 2024-02-06].

[30] HU, Qin-Hong; WENG, Jian-Qing a WANG, Jin-Sheng. Sources of anthropogenic radionuclides in the environment: a review. Online. *Journal of Environmental Radioactivity*. 2010, vol. 101, no. 6, pp. 426-437. ISSN 0265931X. Available from: https://doi.org/10.1016/j.jenvrad.2008.08.004. [Accessed 2024-02-09].

[31] *Natural and Man-made radiation sources*. Online. Polimaster. Available from: https://polimaster.com/us/articles/radiation-safety-basics/natural-and-man-made-radiation-sources/. [Accessed 2024-02-10].

[32] *Oppenheimer's legacy: nuclear test sites around the world*. Online. Geographical. 2023. Available from: https://geographical.co.uk/science-environment/oppenheimers-legacy-nuclear-test-sites-around-the-world. [Accessed 2024-02-10].

[33] *Fact check: Is nuclear energy good for the climate?* Online. Deutsche Welle. 2021. Available from: https://www.dw.com/en/fact-check-is-nuclear-energy-good-for-the-climate/a-59853315. [Accessed 2024-02-10].

[34] *FDA Warns of Interference Between CT Scans and Electronic Medical Devices*. Online. Dicardiology. 2016. Available from: https://www.dicardiology.com/content/fda-warns-interference-between-ct-scans-and-electronic-medical-devices. [Accessed 2024-02-10].

[35] *TSA Is Getting New Futuristic Scanners That May Help You Get Through Security Faster*. Online. Travelan + Leisure. 2022. Available from: https://www.travelandleisure.com/airlines-airports/these-futuristic-x-ray-scanners-are-expected-to-be-at-tsa-checkpoints-this-summer. [Accessed 2024-02-10].

[36] *CMS*. Online. CERN. Available from: https://home.cern/science/experiments/cms. [Accessed 2024-02-10].

[37] *Radionuclides*. Online. EPA United States Environmental Protection Agency. 2023. Available from: https://www.epa.gov/radiation/radionuclides. [Accessed 2024-02-11].

[38] *Radionuclide Basics: Americium-241*. Online. EPA United States Environmental Protection Agency. 2023. Available from: https://www.epa.gov/radiation/radionuclide-basics-americium-241. [Accessed 2024-02-11].

[39] *Americium*. Online. Byjus. 2024. Available from: https://byjus.com/chemistry/americium/. [Accessed 2024-02-13].

[40] *Americium-241*. Online. Beyond NERVA. 2020. Available from: https://beyondnerva.com/radioisotope-power-sources/radioisotope-selection-for-rhu-fuels/americium-241/. [Accessed 2024-02-11].

[41] *Public Health Statement for Americium*. Online. Agency for Toxic Substances and Disease Registry. 2012. Available from: https://wwwn.cdc.gov/TSP/PHS/PHS.aspx?phsid=809&toxid=158. [Accessed 2024-02-11].

[42] *Americium in Ionization Smoke Detectors*. Online. EPA United States Environmental Protection Agency. 2023. Available from: https://www.epa.gov/radtown/americium-ionization-smoke-detectors. [Accessed 2024-02-11].

[43] *Developing Next-gen Space Battery with Americium-241*. Online. EE Power. 2023. Available from: https://eepower.com/market-insights/developing-next-gen-space-battery-with-americium-241/. [Accessed 2024-02-11].

[44] *Americium-241 production*. Online. NATIONAL NUCLEAR LABORATORY. Available from: https://www.nnl.co.uk/customer-solutions/space-exploration/americium-241-production/. [Accessed 2024-02-11].

[45] PROCHÁZKA, Václav; SUCHARA, Ivan; THINOVÁ, Lenka; MIZERA, Jiří; SUCHAROVÁ, Julie et al. Stable and Radioactive Cesium in Natural Environment.

Online. *Chemické listy*. 2023, vol. 117, no. 8, pp. 501-507. ISSN 1213-7103. Available from: https://doi.org/10.54779/chl20230501. [Accessed 2024-02-11].

[46] *Hazardous isotopes*. Online. Radioactivity and Radioation. Available from: https://www.geigercounter.org/radioactivity/isotopes.htm. [Accessed 2024-02-12].

[47] *PRODUCTION OF CESIUM-137*. Online. Industrial And Medical Isotopes. Available from: https://industrialandmedicalisotopes.weebly.com/cs-production.html. [Accessed 2024-02-13].

[48] *Radionuclide Basics: Cesium-137*. Online. EPA United States Environmental Protection Agency. 2024. Available from: https://www.epa.gov/radiation/radionuclide-basics-cesium-137. [Accessed 2024-02-11].

[49] *Products in Nuclear Reactors*. Online. Ministry of the Environment Government of Japan. 2016. Available from: https://www.env.go.jp/en/chemi/rhm/basic-info/2018/02-02-03.html. [Accessed 2024-02-11].

[50] *Radiotherapy, what is it and what is it for?* Online. Nuclear Energy. 2023. Available from: https://nuclear-energy.net/applications/nuclear-medicine/radiation-therapy. [Accessed 2024-02-11].

[51] *Radionuclide Basics: Cobalt-60*. Online. EPA United States Environmental Protection Agency. 2023. Available from: https://www.epa.gov/radiation/radionuclide-basics-cobalt-60. [Accessed 2024-02-11].

[52] *Radioisotope Brief: Cobalt-60 (Co-60)*. Online. Center for Disease Control and Prevention. 2018. Available from: https://www.cdc.gov/nceh/radiation/emergencies/isotopes/cobalt.htm. [Accessed 2024-02-11].

[53] *Radioactivity and Nuclear Chemistry*. Online. Western Oregon University. Available from: https://wou.edu/chemistry/courses/online-chemistry-textbooks/ch103-allied-health-chemistry/ch103-chapter-3-radioactivity/. [Accessed 2024-02-11].

[54] *Iodine*. Online. EPA United States Environmental Protection Agency. 2012. Available from: http://www.energybc.ca/cache/nuclear/nuclear2/www.epa.gov/rpdweb00/radionuclides/iodine.html. [Accessed 2024-02-11].

[55] *Radionuclide Basics: Iodine*. Online. EPA United States Environmental Protection Agency. 2023. Available from: https://www.epa.gov/radiation/radionuclide-basics-iodine. [Accessed 2024-02-11].

[56] *Radionuclide Basics: Plutonium*. Online. EPA United States Environmental Protection Agency. 2023. Available from: https://www.epa.gov/radiation/radionuclide-basics-plutonium. [Accessed 2024-02-12].

[57] *Plutonium*. Online. Nuclear power. 2024. Available from: https://www.nuclear-power.com/nuclear-power-plant/nuclear-fuel/plutonium/. [Accessed 2024-02-12].

[58] *Cassini*. Online. NASA. Available from: https://science.nasa.gov/mission/cassini/radioisotope-thermoelectric-generator/. [Accessed 2024-02-12].

[59] *Radionuclide Basics: Strontium-90*. Online. EPA United States Environmental Protection Agency. 2024. Available from: https://www.epa.gov/radiation/radionuclide-basics-strontium-90. [Accessed 2024-02-12].

[60] *Radioisotope Brief: Strontium-90*. Online. Centers for Disease Control and Pervention. 2018. Available from: https://www.cdc.gov/nceh/radiation/emergencies/isotopes/strontium.htm. [Accessed 2024-02-12].

[61] *Radionuclide Basics: Technetium-99*. Online. EPA United States Environmental Protection Agency. 2024. Available from: https://www.epa.gov/radiation/radionuclide-basics-technetium-99. [Accessed 2024-02-13].

[62] *New technology to produce key medical isotope technetium-99m wins U.S. approval*. Online. C&EN Chemical & Engineering News. 2018. Available from: https://cen.acs.org/articles/96/i8/New-technology-produce-key-medical.html. [Accessed 2024-02-13].

[63] *Uran, deuterium nebo thorium?* Online. Aldebaran Bulletin. 2021. Available from: https://www.aldebaran.cz/bulletin/2021_37_tho.php. [Accessed 2024-02-14].

[64] *JADERNÁ A RADIAČNÍ BEZPEČNOST*. Online. CEZ. Available from: https://www.cez.cz/edee/content/microsites/nuklearni/k34.htm. [Accessed 2024-02-14].

[65] *Radioactive ash from coal power plants*. Online. European Parliament. 2022. Available from: https://www.europarl.europa.eu/doceo/document/E-9-2022-003567_EN.html. [Accessed 2024-02-14].

[66] VOGEL, Christian; HOFFMANN, Marie C.; TAUBE, Mareike C.; KRÜGER, Oliver; BARAN, Rafal et al. Uranium and thorium species in phosphate rock and sewage sludge ash-based phosphorus fertilizers. Online. *Journal of Hazardous*

Materials. 2020, vol. 382. ISSN 03043894. Available from: https://doi.org/10.1016/j.jhazmat.2019.121100. [Accessed 2024-02-14].

[67] *Why phosphate fertiliser use on crops may have to change*. Online. FARMERS WEEKLY. Available from: https://www.fwi.co.uk/arable/crop-management/nutrition-and-fertiliser/phosphate-fertiliser-use-may-change. [Accessed 2024-02-14].

[68] *Ending Nuclear Testing*. Online. United Nations. Available from: https://www.un.org/en/observances/end-nuclear-tests-day/history. [Accessed 2024-02-14].

[69] OHTSUKA, Yoshihito; AOYAMA, Michio; TAKAKU, Yuichi; IGARASHI, Yasuhito; HATTORI, Michinari et al. 240Pu/239Pu and 242Pu/239Pu atom ratios of Japanese monthly atmospheric deposition samples during 1963–1966. Online. *Scientific Reports*. 2019, vol. 9, no. 1. ISSN 2045-2322. Available from: https://doi.org/10.1038/s41598-019-44352-7. [Accessed 2024-02-14].

[70] *Nuclear tests in the atmosphere*. Online. STUK Radiation and Nuclear Safety Authority. Available from: https://stuk.fi/en/nuclear-tests-in-the-atmosphere. [Accessed 2024-02-14].

[71] *Global Hibakusha*. Online. The Asia-Pacific Journal – Japan Focus. 2022. Available from: https://apjjf.org/2022/7/Jacobs.html. [Accessed 2024-02-14].

[72] De BORTOLI, M.; GAGLIONE, P.; MALVICINI, A. and VAN DER STRICHT, E. Plutonium-239 and 238, Strontium-90 and Cesium-137 in Surface Air from Mid 1961 Through 1965. Online. *Proceedings of the First International Congress of Radiation Protection*. 1968, pp. 361-367. ISBN 9781483283128. Available from: https://doi.org/10.1016/B978-1-4832-8312-8.50067-9. [Accessed 2024-02-14].

[73] *Number of nuclear weapons tests*. Online. Our World in Data. 2024. Available from: https://ourworldindata.org/grapher/number-of-nuclear-weapons-tests. [Accessed 2024-02-18].

[74] *UNSCEAR 1993 Report, Report to the General Assembly with Scientific Annexes*. Online. United Nations. 1994. Available from: https://www.unscear.org/unscear/en/publications/1993.html. [Accessed 2024-02-19].

[75] BURCHFIELD, L. A. a KURODA, P. K. Recent atmospheric injections of nuclear debris: Fallout from the 16 October 1980 nuclear explosion. Online. *Geochemical*

Journal. 1983, vol. 17, no. 2, pp. 63-70. ISSN 0016-7002. Available from: https://doi.org/10.2343/geochemj.17.63. [Accessed 2024-03-12].

[76] *UNSCEAR 1982 Report, Report to the General Assembly with Scientific Annexes*. Online. United Nations. 1982. Available from: https://www.unscear.org/unscear/en/publications/1982.html. [Accessed 2024-03-13].

[77] BARTUSKOVÁ, M.; ŠKRKAL, J.; SCHLESINGEROVÁ, E.; BEČKOVÁ, V. a MALÁTOVÁ, I. Doses from Cs-137 and Sr-90 to Czech population due to milk consumption. Online. *Radioprotection*. 2017, vol. 52, no. 3, pp. 171-176. ISSN 0033-8451. Available from: https://doi.org/10.1051/radiopro/2017016. [Accessed 2024-02-19].

[78] *UNSCEAR 1982 Report, Report to the General Assembly with Scientific Annexes*. Online. United Nations. 1982. Available from: https://www.unscear.org/unscear/en/publications/1982.html. [Accessed 2024-02-26].

[79] *Energy*. Online. Our World in Data. 2023. Available from: https://ourworldindata.org/energy. [Accessed 2024-03-04].

[80] *Global renewables are growing but have been partly offset by a decline in nuclear production*. Online. Our World in Data. 2022. Available from: https://ourworldindata.org/global-renewables-are-growing-but-are-only-managing-to-offset-a-decline-in-nuclear-production. [Accessed 2024-03-09].

[81] *Renewable Energy*. Online. Teacheng Ineering. 2024. Available from: https://www.teachengineering.org/lessons/view/cub_environ_lesson09. [Accessed 2024-03-09].

[82] *What was the death toll from Chernobyl and Fukushima?* Online. Our World in Data. 2022. Available from: https://ourworldindata.org/what-was-the-death-toll-from-chernobyl-and-fukushima. [Accessed 2024-03-09].

[83] *Černobyl*. Online. Státní úřad pro jadernou bezpečnost. Available from: https://sujb.gov.cz/cernobyl. [Accessed 2024-03-09].

[84] *Atlas of cesium deposition on Europe after the Chernobyl accident*. Online. Europe Union – Publications Office of European Union. Available from: https://op.europa.eu/en/publication-detail/-/publication/110b15f7-4df8-49a0-856f-be8f681ae9fd. [Accessed 2024-03-10].

[85] *Mapa kontaminace půdy České republiky 137Cs po havárii JE Černobyl*. Online. RULÍK, Petr a HELEBRANT, Jan. SÚRO – Státní ústav radiační ochrany. 2011. Available from: https://www.suro.cz/files/2021-03/Zprava%202011%20-%2022%20-%20Kontaminace%20pudy%20Ceske%20republiky%20137Cs%20-%20Mapa-1.pdf. [Accessed 2024-03-10].

[86] *Fukushima Daiichi Accident*. Online. World Nuclear Association. 2023. Available from: https://world-nuclear.org/information-library/safety-and-security/safety-of-plants/fukushima-daiichi-accident.aspx. [Accessed 2024-03-10].

[87] *Fukushima No. 1 cleanup plan only getting tougher*. Online. The Japan Times. 2021. Available from: https://www.japantimes.co.jp/2021/03/11/bosai-special/fukushima-no-1-cleanup-plan-getting-tougher/. [Accessed 2024-03-10].

[88] MATSUDA, Norihiro; MIKAMI, Satoshi; SHIMOURA, Susumu; TAKAHASHI, Junko; NAKANO, Masakazu et al. Depth profiles of radioactive cesium in soil using a scraper plate over a wide area surrounding the Fukushima Dai-ichi Nuclear Power Plant, Japan. Online. *Journal of Environmental Radioactivity*. 2015, vol. 139, no. 427-434. ISSN 0265931X. Available from: https://doi.org/10.1016/j.jenvrad.2014.10.001. [Accessed 2024-03-10].

[89] MISHRA, S.; SAHOO, S.K.; BOSSEW, P.; SORIMACHI, A. a TOKONAMI, S. Vertical migration of radio-cesium derived from the Fukushima Dai-ichi Nuclear Power Plant accident in undisturbed soils of grassland and forest. Online. *Journal of Geochemical Exploration*. 2016, vol. 169, pp. 163-186. ISSN 03756742. Available from: https://doi.org/10.1016/j.gexplo.2016.07.023. [Accessed 2024-03-14].

[90] MATSUOKA, Kaori; MORITSUKA, Naoki; NUKADA, Mitsuhiko a SATO, Mamoru. Continuous nitrogen fertilization retards the vertical migration of Fukushima nuclear accident-derived cesium-137 in apple orchard soil. Online. *Science of The Total Environment*. 2020, vol. 731. ISSN 00489697. Available from: https://doi.org/10.1016/j.scitotenv.2020.138903. [Accessed 2024-03-14].

[91] FUKÁTKO, Tomáš. *Detekce a měření různých druhů záření*. Senzory neelektrických veličin. Praha: BEN – technická literatura, 2007. ISBN 978-80-7300-193-3.

[92] *Přenosný analyzátor záření gama, GT-40, GT-40-S*. Online. Georadis. 2016. v: http://www.georadis.com/cs/produkty/gt-40.html. [Accessed 2024-03-23].

[93] *GT-40R7*. Online. Georadis. 2016. Available from: http://data.georadis.com/data/gt40/manual/GT-40R7.pdf. [Accessed 2024-03-23].

[94] *Laserový nivelační přístroj*. Online. Einhell. 2024. Available from: https://www.einhell.cz/p/2270095-tc-ll-1/. [Accessed 2024-03-22].

[95] *ArcGIS Pro*. Online. Esri. Available from: https://www.esri.com/en-us/arcgis/products/arcgis-pro/overview. [Accessed 2024-03-23].

[96] *Sartorius – ENTRIS 822-1S*. Online. Wolflabs. Available from: https://www.wolflabs.co.uk/laboratory-products/balances-top-pan/10101500. [Accessed 2024-03-23].

[97] *Popůvky – Measurement*. Online. Mapy.cz. 2024. Available from: https://en.mapy.cz/zakladni?mereni-vzdalenosti&rm=97KNqx8hAcgQ03OhT0fItR0fZF&x=17.2586464&y=49.3369917&z=14. [Accessed 2024-03-26].

[98] *ČHMÚ nowcasting webportal*. Online. Český hydrometeorologický ústav. 2022. Available from: https://www.chmi.cz/files/portal/docs/meteo/rad/inca-cz/short.html. [Accessed 2024-03-26].

[99] KITA, Kazuyuki; IGARASHI, Yasuhito; KINASE, Takeshi; HAYASHI, Naho; ISHIZUKA, Masahide et al. Rain-induced bioecological resuspension of radiocesium in a polluted forest in Japan. Online. *Scientific Reports*. 2020, roč. 10, č. 1. ISSN 2045-2322. Available from: https://doi.org/10.1038/s41598-020-72029-z. [Accessed 2024-03-26].

[100] *Radiouhlíková laboratoř*. Online. Ústav jaderné fyziky AV ČR. Available from: https://www.ujf.cas.cz/cs/nase-sluzby/radiouhlikova_laborator/O_nas/. [Accessed 2024-04-03].

LIST OF ABBREVIATIONS

AMS	Accelerator Mass Spectrometry
AV	Actual Value
BG	Background
CERN	Conseil Européen pour la recherche nucléaire
CRA	Conventional Radiocarbon Age
CRL	Czech Radiocarbon Laboratories
CT	Computed Tomography
DR	Batch Power Input
GB	Gigabyte
GIS	Geographic Information System
GM	Geiger–Müller
GT	Gamma Spectrometer
IDW	Inverse Distance Weighted
MV	Measured Value
RTG	Radioisotope Thermoelectric Generators
X-ray	High-energy Electromagnetic Radiation

LIST OF FIGURES

LIST OF TABLES

EQUATION

APPENDICES

A I. CRL Radiocarbon Dating Results

APPENDIX A I: CRL RADIOCARBON DATING RESULTS

Na Truhlářce 39/64
180 86 Praha 8
tel.: +420 266 177 233
e-mail: crl@ujf.cas.cz

Výsledky radiouhlíkového datování CRL

Vzorky a výsledky

K radiouhlíkovému datování byly přijaty vzorky kostí odebrané výkopem v lokalitě Popůvky u Kojetína. Zadavatelem je doc. RNDr. Vojtěch Křesálek, CSc., Fakulta aplikované informatiky, Univerzita Tomáše Bati ve Zlíně, Nad Stráněmi 4511, 760 05 Zlín. Jako možné ovlivnění vzorků v místě nálezu uvádí zadávající pronikání kořínků rostlin, možné poodběrové ovlivnění vzorků není známo. Popisy a vlastnosti vzorků jsou uvedeny v Tabulce 1 a výsledky datování v Tabulce 2.

Tabulka 1: Popis a vlastnosti vzorků

Lab. číslo	Značení vzorků	Materiál/Vlastnosti	Koncentrace kolagenu (mg/g)
CRL24_0022	vrstva 15, 0,53m	kost, pevnější, jakost 5,5	13
CRL24_0023	vrstva 18, 0,63m	kost, křehká, jakost 4,5	36
CRL24_0024	vrstva 21, 0,73m	kost, křehká, spongyózní, jakost 5,5	17
CRL24_0025	vrstva 22, 0,75m	kost, křehká, spongyózní, jakost 5,5 (6)	10
CRL24_0026	vrstva 23, 0,8m	kost, křehká, spongyózní, jakost 5,5	16
CRL24_0027	vrstva 24, 0,83m	kost, křehčí, jakost 5	21
CRL24_0028	vrstva 25, 0,85m	kost, křehčí, jakost 5	18
CRL24_0029	vrstva 27, 0,93m	kost, křehčí, spongyózní, jakost 4,5	41
CRL24_0030	vrstva 28, 0,95m	spálená kost, bez přítomnosti karbonátů	-
CRL24_0031	vrstva 29, 1m	kost, pevnější, jakost 4,5	31

Hodnocení jakosti vzorku kosti/zubu: 1 – nejlepší, 6 – nevyhovující. **U vzorků s hodnocením jakosti 4,5 a horším je doporučováno opatrné nakládání s výsledky datování.** Všeobecně se předpokládá, že analýzy kostí s koncentrací kolagenu pod 1% neposkytují věrohodné výsledky [Brock et al. 2010].

Tabulka 2: Výsledky radiouhlíkového datování (intervaly kalibrovaného stáří)

Lab. číslo	Značení vzorků	Konvenční radiouhlíkové stáří (BP)	Kalibrované stáří (AD, BC)		P (%)
CRL24_0022	vrstva 15, 0,53m	119 ± 16	**1687 – 1924 AD**	*	**97**
CRL24_0023	vrstva 18, 0,63m	275 ± 16	**1524 – 1662 AD**	*	**96**
CRL24_0024	vrstva 21, 0,73m	271 ± 18	**1524 – 1794 AD**	*	**97**
CRL24_0025	vrstva 22, 0,75m	340 ± 16	**1480 – 1635 AD**	*	**96**
CRL24_0026	vrstva 23, 0,8m	438 ± 16	**1432 – 1466 AD**		**95**
CRL24_0027	vrstva 24, 0,83m	2227 ± 17	**376 – 203 BC**	*	**96**
CRL24_0028	vrstva 25, 0,85m	2227 ± 17	**376 – 203 BC**	*	**96**
CRL24_0029	vrstva 27, 0,93m	2252 ± 17	**390 – 208 BC**	*	**96**
CRL24_0031	vrstva 29, 1m	2405 ± 18	**541 – 403 BC**		**95**

* *spojený interval, podrobněji v příloze*

Datovanou epizodou je vždy doba nárůstu/vzniku datovaného materiálu (například dřevní hmoty, která byla později karbonizována).
U vzorků kořenů lidských zubů datovaná epizoda odpovídá přibližně době jejich prořezání. U vzorků kostí je to střední charakteristická doba utvoření kostního kolagenu, která může u starších lidských jedinců předcházet době smrti až o desítky let [Handlos et al. 2018, Bárta a Štolc 2007]. V případě tkání krátkodobě žijících živočichů se datovaná epizoda přibližuje době smrti.

Na Truhlářce 39/64
180 86 Praha 8
tel.: +420 266 177 233
e-mail: crl@ujf.cas.cz

Postupy zpracování vzorků

Příchozí vzorky[1] byly v laboratoři kontrolovány a mechanicky očištěny.
Uhlíky, dřevo a rostlinné makrozbytky: Vzorky byly louženy v roztocích 0,5 M HCl, 0,1 M NaOH a 0,01 M HCl a mezi jednotlivými kroky promývány destilovanou vodou. V literatuře je tato předúprava nazývána postupem Acid/Alkali/Acid (AAA neboli ABA) [Gupta a Polach 1985, Jull et al. 2006, Brock et al. 2010]. Vzorky byly poté sušeny do konstantní hmotnosti při teplotě 60 °C. V průběhu loužení může dojít k úplné ztrátě vzorku následkem jeho kvantitativního rozpuštění.
Kosti a zuby: Očištěné vzorky byly drceny a frakce o průměrech zrn 0,5 – 1 mm byla opakovaně loužena v roztocích zředěné HCl, vody, zředěného NaOH, vody a silně zředěné HCl, dle postupů odvozeného z publikací [Gupta a Polach 1985, Longin 1971, Law a Hedges 1989, Jull et al. 2006, Brock et al. 2010]. Ze vzorků izolovaný kolagen byl želatinizován při teplotě 75 °C a filtrován na filtru ze skleněných vláken. Rozpuštěný podíl byl zpracován ultrafiltrací a retentát (bílkovinná frakce o hmotnostech více než 30 kDa) vysušen do konstantní hmotnosti při teplotě 60 °C.
Karbonáty a spálené kosti: Vzorky byly mechanicky očištěny, povrchové vrstvy byly odstraněny pomocí zředěné HCl. Poté byly vzorky proplachovány demineralizovanou vodou, po vysušení byly rozloženy působením koncentrované H_3PO_4 v evakuovaných ampulích a uvolněný oxid uhličitý byl jímán do ampule chlazené kapalným dusíkem.
Vzorek spálené kosti **24_0030** neobsahoval karbonátovou formu uhlíku a byl proto z datování vyloučen.

Grafitizace: Vysušené vzorky byly s přídavkem CuO zataveny pod dynamickým vakuem do ampulí z křemenného skla a spáleny při teplotě 900 °C. Připravený oxid uhličitý byl přečištěn a dávkován do grafitizačního reaktoru. Vsádková metoda grafitizace byla odvozena z obdobných postupů používaných v zahraničí [Rinyu et al. 2015, Orsovszki a Rinyu 2015].

Měření vzorků

Měření grafitizovaných vzorků bylo provedeno na kompaktním tandemovém urychlovači se spektrometrickou trasou MILEA v radiouhlíkové laboratoři CRL ÚJF AV ČR, v.v.i. s mezinárodním kódem CRL [Kučera et al. 2022]. Spolu se vzorky bylo měřeno minimálně pět párů grafitů připravených ze sekundární kyseliny šťavelové NIST (NBS) HOX II SRM 4990-C [Schneider et al. 1995] a z fosilního anhydridu kyseliny ftalové. AMS data byla zpracována pomocí softwaru BATS [Wacker et al. 2010], včetně opravy na pozadí, korekce na vliv frakcionace pomocí hodnoty $\delta^{13}C$ měřené AMS a normalizaci na standardy HOX II. Naměřené aktivity ^{14}C a jejich kombinované nejistoty byly vyjádřeny v letech BP (Before Present) jako konvenční radiouhlíkové stáří (Conventional Radiocarbon Age – CRA)[2] dle Stuiver-Polachovy konvence [Stuvier a Polach 1977]. Kombinované nejistoty uváděné u hodnot konvenčního radiouhlíkového stáří odpovídají pravděpodobnosti přibližně 68% [Curie 1999].

Interpretace naměřených aktivit

Pro určení stáří vzorku 24_0022 byl použit kalibrační program CALIBomb s kombinací kalibračních křivek IntCal20 (pro klasické datování suchozemských vzorků severní polokoule) a LEVIN, která je určena pro datování pomocí bombového píku suchozemských vzorků původem z Evropy [CALIBomb; Reimer et al. 2004; Levin a Kromer 2004; Hammer a Levin 2017; Reimer et al. 2020].
Pro určení stáří ostatních vzorků byl použit kalibrační program OxCal 4.4 spolu s kalibrační křivkou IntCal20 [Bronk Ramsey 2009, Reimer et al. 2020].

[1] Pro účely datování se předpokládá, že stáří datovatelné formy uhlíku je v celém zpracovaném vzorku stejné. Laboratoř výsledky analýz vztahuje pouze na dodané vzorky a nikoliv na předměty, ze kterých byly (mohly být) vzorky odebrány.
[2] Jde o zvláštní formou vyjadřování aktivity ^{14}C, která je bez kalibrace pouze v přibližné relaci se stářím reálným.

Na Truhlářce 39/64
180 86 Praha 8
tel.: +420 266 177 233
e-mail: crl@ujf.cas.cz

Po přiřazení nejistot daných radiouhlíkovou kalibrační křivkou bylo konvenční radiouhlíkové stáří a jeho kombinovaná nejistota přepočteno na výsledný interval (intervaly) kalibrovaného stáří (pro interval nejistoty dvě sigma stanovení aktivity ^{14}C, který odpovídá pravděpodobnosti přibližně 95%).
Celková míra absolutní pravděpodobnosti P výsledného intervalu kalibrovaného stáří vycházela z rozšířené kombinované nejistoty stanovení ^{14}C (dvě sigma) a byla vypočtena kalibračním programem. Pro výsledky analýz jsou v kalibračním souboru uvedeny kalibrační diagramy (křivka průběhu hustot pravděpodobnosti je přidružena k vodorovné ose diagramu) spolu s podrobným výpisem intervalů kalibrovaného stáří pro hladiny pravděpodobnosti 95% a 68% a skupinový diagram porovnávající křivky hustoty pravděpodobnosti doby původu vzorků.

V Praze dne 26. 3. 2024

Ing. Ivo Světlík, Ph.D.

Literatura

Bárta P a Štolc S Jr (2007) HBCO Correction: Its impact on archaeological absolute dating. *Radiocarbon,* 49(2), 465–472. doi:10.1017/S0033822200042399

Brock F et al. (2010) Current pretreatment methods for AMS radiocarbon dating at the Oxford Radiocarbon Accelerator Unit (ORAU). *Radiocarbon,* 52(1), 103–112. doi:10.1017/S0033822200045069

Bronk Ramsey C (2009) Bayesian analysis of radiocarbon dates. *Radiocarbon*, 51(1), 337-360. doi:10.1017/S0033822200033865

CALIBomb: http://calib.org

Curie LA (1999) Nomenclature in Evaluation of Analytical Methods Including Detection and Quantification Capabilities. (IUPAC Recommendation 1995). *Analytica Chimica Acta,* 391(2), 105–126. doi:10.1016/S0003-2670(99)00104-X

Gupta SK and Polach HA (1985) Radiocarbon dating practises at ANU. *ANU,* Canberra.

Hammer S a Levin I. (2017) Monthly mean atmospheric $D^{14}CO_2$ at Jungfraujoch and Schauinsland from 1986 to 2016. heiDATA: Heidelberg Research Data Repository [Distributor] V2 [Version] doi:10.11588/data/10100

Handlos P et al. (2018) Bomb peak: radiocarbon dating of skeletal remains in routine forensic medical practice. *Radiocarbon,* 60(4), 1017–1028. doi:10.1017/RDC.2018.72

Hua Q et al. (2021) Atmospheric radiocarbon for the period 1950 – 2019. *Radiocarbon,* 64(4), 723–745. doi:10.1017/RDC.2021.95

Jull AJT et al. (2006) Application of accelerator mass spectrometry to environmental and paleoclimate studies at the University of Arizona. *Radioactivity in the Environment,* 8, 3–23. doi:10.1016/S1569-4860(05)08001-0

Kučera J et al. (2022) A new AMS facility MILEA at the Nuclear Physics Institute in Řež, Czech Republic. *Nuclear Instruments and Methods in Physics Research B,* 527, 29–33. doi:10.1016/j.nimb.2022.07.012

Law IA a Hedges REM (1989) A semi-automated bone pretreatment system and the pretreatment of older and contaminated samples. *Radiocarbon,* 31(3), 247–253. doi:10.1017/S0033822200011759

Levin I a Kromer B. (2004) A concatenation of Levin's Vermunt and Schauinsland data sets. Representative of the European atmosphere (except for highly industrial areas). Published by Levin and

Na Truhlářce 39/64
180 86 Praha 8
tel.: +420 266 177 233
e-mail: crl@ujf.cas.cz

Kromer in The Tropospheric $^{14}CO_2$ Level in Mid-Latitudes of the Northern Hemisphere (1959-2003). *Radiocarbon*, 46(3), 1261-1272. doi:10.1017/S0033822200033130

Longin R (1971) New method of collagen extraction for radiocarbon dating. *Nature,* 230, 241–242. doi:10.1038/230241a0

Molnár M et al. (2013a). EnvironMICADAS: a mini ^{14}C-AMS with enhanced gas ion source interface in the Hertelendi Laboratory of Environmental Studies (HEKAL), Hungary. *Radiocarbon,* 55(2–3), 338–344. doi:10.1017/S0033822200057453

Molnár M et al. (2013b). Status report of the new AMS ^{14}C sample preparation lab of the Hertelendi Laboratory of Environmental Studies (Debrecen, Hungary). *Radiocarbon*, 55(2–3), 665–676. doi:10.1017/S0033822200057829

Orsovszki G a Rinyu L (2015) Flame-sealed tube graphitization using zinc as the sole reduction agent: precision improvement of Environ MICADAS ^{14}C measurements on graphite targets. *Radiocarbon,* 57(5), 979–990. doi:10.2458/azu_rc.57.18193

Reimer PJ et al. (2020) The IntCal20 Northern Hemisphere Radiocarbon Age Calibration Curve (0–55 cal kBP). *Radiocarbon*, 62(4), 725–757. doi:10.1017/RDC.2020.41

Reimer PJ et al. (2004) Discussion: Reporting and Calibration of Post-Bomb ^{14}C Data. *Radiocarbon,* 46(3), 1299–1304. doi:10.1017/S0033822200033154

Rinyu L et al. (2013) Application of zinc sealed tube graphitization on sub-milligram samples using Environ MICADAS. *Nuclear Instruments and Methods in Physics Research B,* 361, 406–413. doi:10.1016/j.nimb.2015.03.083

Schneider et al. (1995) Measurements of the Oxalic Acid II/Oxalic Acid I Ratio as a Quality Control Parameter at NOSAMS. *Radiocarbon,* 37(2), 693–696. doi:10.1017/S0033822200031210

Stuiver M a Polach HA. (1977) Reporting of ^{14}C data. *Radiocarbon*, 19(3), 355-363. doi:10.1017/S0033822200003672

Wacker L et al. (2010) Bats: A new tool for AMS data reduction. *Nuclear Instruments and Methods in Physics Research Section B,* 268, 976–979. doi:10.1016/j.nimb.2009.10.078